MODAL ANALYSIS OF MEMS GYROSCOPIC SENSORS

by

Marc Burnie

A thesis submitted to the Department of Mechanical & Materials Engineering

In conformity with the requirements for

the degree of Master of Applied Science

Queen's University

Kingston, Ontario, Canada

(May, 2010)

Abstract

Microgyroscopes find popular applications in modern life, such as, vehicle navigation, inertial positioning, human body motion monitoring, etc. In this study, three unique MEMS gyroscopic sensors were investigated using experimental methods and finite element analysis (FEA) modelling, particularly their modal behaviour. The analytical, simulated and experimental results were compared and the discrepancy between resonant frequencies of the significant mode shapes was discussed.

Three microfabricated gyroscopes were investigated: a thermally-actuated in-plane gyroscope, an electrostatically-actuated in-plane gyroscope and an electrostatically-actuated out-of-plane gyroscope. Numerical finite element modal analysis for these three gyroscopes was conducted using COMSOL Multiphysics^{TM}. The experimental testing was conducted using a microsystem analyzer (MSA-400 PolyTec) with an integrated laser vibrometer.

The simulation models predicted that the frequencies for driving and sensing modes were 4.948kHz and 5.459kHz for a thermally-actuated gyroscope, which agreed well with experimentally determined results of 5.98kHz and 6.0kHz respectively. The power requirements of a thermally-actuated gyroscope were 363.39mW to elicit a maximum peak-to-peak displacement of 4.2μm during dynamic operation. Similarly, the simulated frequencies for the driving and sensing modes were 1.170kHz and 1.644kHz for an electrostatically-actuated in-plane gyroscope, which corresponded to experimentally determined resonant frequencies 1.6kHz and 1.9kHz.

Simulation for the electrostatically-actuated out-of-plane gyroscope was conducted and the frequencies for the driving and sensing modes were found to be 2.159kHz and 3.298kHz. Due to

some fabrication defects, the experimental testing for this microgyroscope was not successful. Some recommendations to improve the design were provided for the future work.

Dedication

I would like to dedicate this thesis to my father, Martin Burnie, who taught me the value of education and the meaning of hard work.

Acknowledgements

I would to sincerely thank my supervisor, Dr. Yongjun Lai, for his guidance, understanding and patience. I would not have been able to complete this thesis if it wasn't for his valuable advice and support.

I would also like to thank Jacky Chow, Xin Guo and Kongying Xie, my lab mates, for their assistance with lab equipment and being great people to work with in general.

Finally, I would like to thank my parents and the rest of my family for their ceaseless support.

Table of Contents

List of Figures

List of Tables

Symbols and Nomenclature

Abbreviation	Phrase
AC	Alternating Current
CMOS	Complementary Metal-Oxide-Semiconductor
COMSOL	Multiphysics Modelling Software
CVD	Chemical Vapour Deposition
DC	Direct Current
DOF	Degrees-of-Freedom
DRIE	Deep Reactive Ion Etching
FEA	Finite Element Analysis
FEM	Finite Element Modelling
FFT	Fast Fourier Transform
ICs	Integrated Circuits
LIGA	Lithografie, Galvanoformung, Abformung
MEMS	Micro-Electro-Mechanical Systems
MUMPS	Multi-User MEMS Process
PMA	Polytec Motion Analyzer
PSV	Polytec Scanning Vibrometer
PVD	Physical Vapour Deposition
RMS	Root-Mean Square
SCSi	Single-Crystal Silicon
SEM	Scanning Electron Microscope
SOI	Silicon-on-Insulator
ZRO	Zero Rate Output

Chapter 1 Introduction

1.1 Introduction to Micro-Electro-Mechanical Systems

Micro-Electro-Mechanical Systems (MEMS) is the integration of mechanical elements, sensors, actuators, and electronics on a silicon substrate through microfabrication technology, which studies micro-scale physics and microfabrication processes for the creation miniature devices. MEMS devices typically range in size between sub-microns to sub-millimeter.

Richard Feynman (1962) realized the potential benefits of creating devices in the micro-scale when he conceptualized the MEMS field in his famous lecture "There's Plenty of Room at the Bottom".[1] In the lecture he identified a few features of this technology:

- Lower Cost – The relatively small volume of the devices reduces the cost of materials. The expense of exotic materials such as gold are negligible compared to cost of the microfabrication process. However, the price of fabrication is highly susceptible to economies of scale since the initial capital cost is higher than the material cost. The price of the equipment is reduced through the reapplication of outdated CMOS equipment and lithography masks can be used multiple times. Most microfabrication processes are parallel by nature so many devices can be made for approximately the same cost as making one. Economically, it is then reasonable to include many devices on a single wafer, even identical devices that can be used as redundancy. The intrinsic material value of each device is relatively low so they can be disposed of with little environmental impact.

- Low power – Less work is done to MEMS devices because smaller displacements and momentum forces are required. The heat capacity of micro-components is also relatively

small in comparison to human scale objects, which allows for the use of joule heating as a method of actuation. The integration of MEMS devices with IC technology decreases the required length of the electrical interconnects that ultimately reduces the power due to heat loss in the wires.

- Fast response – The reduction in mass reduces the time and energy required to change state. Thermal and electrical components have less capacitance and mechanical components have higher resonant frequencies and rapidly accelerate. MEMS devices have the ability to detect and react to disturbances much faster making them ideal for sensing applications.

- Insignificance of inertial forces - This was derived from the underlying forces that dominate in the micro scale. Scaling laws verify that the influence of volumetric forces, such as gravity and momentum, have on the devices at that scale would be reduced; while surface area effects, such as surface tension and Van der Waals attraction, would dominate.

1.2 Micro-gyroscopes

1.2.1 Applications

Gyroscopic sensors are already an integral component of the automotive and aerospace industries with specific applications in roll-over detection in vehicles, orientation diction in global positioning systems (GPS), as well as diction of yaw, pitch and roll orientation in missiles and aircraft. With the advent of MEMS micro-gyroscope technology the range of cost-efficient applications of gyroscopic sensors has expanded. The driving forces behind this trend are smaller

form-factors, higher accuracy, greater power efficiency and lower cost. Some of the growing applications of MEMS gyroscopic sensors are:

- Image stabilization for handheld video, DSLR and point-and-shoot cameras

- Computer and video game input devices

- Biomechanical research and monitoring, such as, human motion tracking

- Personal electronics, toys and hobbyist applications

The application for micro gyroscopic sensors is large and will continue to grow with further research into making them a more enabling technology.

1.2.2 Operating Principles

The majority of MEMS vibratory gyroscopes use the Coriolis force to detect the angular velocity of a rotating body, which the gyroscope is attached to, by oscillating a proof mass that is suspended with elastic springs that restrict the mass to move in two degrees of freedom (DOF).

The Coriolis force is a fictitious force that cannot be observed in the inertial frame, the non-accelerating of reference. The Coriolis acceleration is given by the formula:

$$\overrightarrow{a_c} = 2\vec{v} \times \overrightarrow{w}, \tag{1.1}$$

Where $\overrightarrow{a_c}$ is the Coriolis acceleration, $\vec{v}$ is the velocity of the proof mass in the accelerating frame of reference and $\overrightarrow{w}$ is the angular velocity of the rotating body. The cross product of the velocity and angular velocity gives a resultant acceleration in the orthogonal direction. If the velocity and angular velocity of the body act in the same direction then there is no resultant Coriolis acceleration.

The angular velocity $\overrightarrow{w}$ is the characteristic of the rotating body that we intend to indirectly measure; as such an artificial velocity must be imposed on the microgyrscope's proof mass in order to create a resultant Coriolis force that can be directly measured. It is unreasonable to

impose a constant velocity on the proof mass since it would soon leave the confines of the system; an oscillating velocity can be used instead. The Coriolis force will also be oscillatory in nature as a result, and thus the forcing frequency of the gyroscope will ideally coincide with the sensing resonant frequency. In other words, ideally the frequency of the imposed proof mass velocity must match the natural frequency in which the proof mass will readily oscillate in the sensing direction. If the proof mass is not excited at the correct frequency then the displacement in the sensing direction will be significantly reduced. The process for designing a mechanical system that has the same or similar driving and sensing resonant frequencies is called mode matching and is an important constraint for micro-gyroscopes.
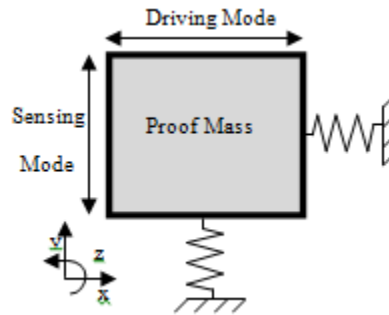
Figure 1-1-1 - Hypothetical vibratory gyroscope.

Another important constraint in the design of vibratory gyroscopes is the decoupling frame. Given a hypothetical gyroscope such as in figure 1-1, any displacement in the driving direction will change the length of the springs in the sensing direction and vice-versa, which will affect the underlying forces. A decoupling frame will ideally mechanically isolate the driving and sensing modes.

1.2.3 Gyroscope Kinematics

The MEMS gyroscope, M, is mounted on some hypothetical rigid body with unknown dimensions and a centre of mass, *G*, with an angular velocity of *w* as shown in figure 1-2 below.

An inertial frame of reference is used in this investigation and thus the coordinate system rotates with the rigid body. The position vector $\vec{P}_{M/G}$ locates the centre of the gyroscopes proof mass to the centre of mass of the rigid body. The direction vectors, $\hat{\imath}$, $\hat{\jmath}$, $\hat{k}$, rotate with the center of mass of the object. In the below case, the driving direction corresponds to the $\hat{\imath}$ direction, the sensing direction is in the $\hat{\jmath}$ direction and the input rotation is about the $\hat{k}$ direction.
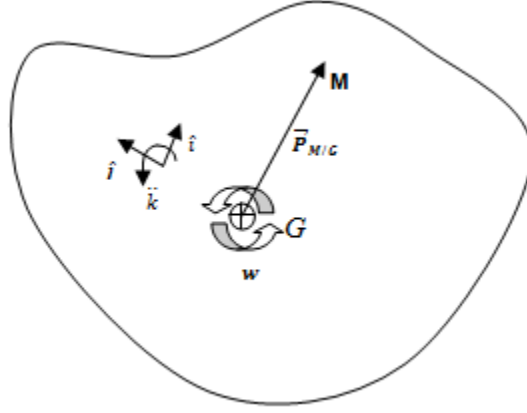
Figure 1-1-2 - Kinematics of a gyroscopic sensor system

The kinematic formulas arising from this system are given below:

$$\vec{P}_{M/G} = x\hat{\imath} \tag{1.2}$$

$$\vec{v}_{M/G} = \dot{x}\hat{\imath} + wx\hat{\jmath} \tag{1.3}$$

$$\vec{a}_{M/G} = (\ddot{x} - w^2 x)\hat{\imath} + (2w\dot{x} + \dot{w}x)\hat{\jmath} \tag{1.4}$$

The $\ddot{x}$ term in the right side of equation (1.4) is an acceleration imposed on the system by the forced vibration on the proof mass; the $-w^2 x$ term is the centrifugal force. Both these accelerations act in the driving direction. The $2w\dot{x}$ and $\dot{w}x$ terms are the Coriolis and Euler accelerations respectively; these accelerations act in the sensing direction. The Euler acceleration disappears when the angular velocity of the body does not change. By mounting the gyroscope close to the centre of mass of the rigid body then the Euler acceleration becomes negligible and the acceleration acting on the proof mass in the sensing direction becomes:

$$\vec{a}_c = 2w\dot{x}\hat{\jmath} \tag{1.5}$$

The resultant force is proportional to the angular velocity of the rigid body when the velocity of the proof mass in the driving direction is constant, which is a desirable characteristic for a sensor. However the velocity of the proof mass in the driving direction is not constant and is in the form:

$$\dot{x} = A(2\pi f)\cos(2\pi ft + \varphi) \tag{1.6}$$

where A is the amplitude, f is the frequency, t is the time and φ is the phase angle. This will, in turn, produce an oscillating force and oscillating output signal. The velocity of the proof mass in the driving direction is controlled thus the angular velocity can be deduced from measuring the force in the sensing direction.

A potential source of error is an outside acceleration acting on the rigid body in the sensing direction causing a resultant force on the proof mass. This can be corrected by measuring the acceleration separately and adjusting the output signal accordingly.

1.2.4 Performance Characterization

The quality of all gyroscopic sensors can be measured by their performance of each of the below factors:

- Scale Factor – The proportional constant of the change of output to a change in input. The output signal is measured in Volts so the unit of the constant is V/(°/s). The scale factor can be found by fitting a straight line to the input and output data using the method of least squares.

- Resolution – The minimum change in input that will result in a change in output. The white noise of the device is what limits the resolution; therefore the resolution can be determined by measuring the standard deviation of the white noise. The unit used is (°/s)/√Hz.

- Drift Rate – The output of a gyroscope is subject to a slowly changing random function that is independent of the input angular rate. The drift rate is the peak-to-peak value of this function and is measured in °/s.

- Sensitivity – As with other sensors, the output signal can be affected by environmental conditions or other undesirable inputs. Some common secondary inputs include temperature, pressure and humidity. The sensitivity of the output to a secondary input is the ratio of change in the proportional scale factor to a change in the secondary input. The units of sensitivity are different depending on which undesirable input is considered. All sensitivities must be compared to the operating standard by which the original scale factor was determined.

- Zero Rate Output – Any inherent dissymmetry or disparity in a micro-gyroscope may result in an offset to the output. The zero rate output (ZRO) can be found by determining the mean of the output signal in the absence of an input rotation and is measured in Volts.

- Quality Factor – Mechanical, damped mass-spring systems respond to all forcing frequencies but can have varying amplitudes depending on the natural frequencies of the system. A damped mass-spring system that is being vibrated at its natural frequency will experience greater amplitude compared to a similar system that is not. Increasing the damping in the system will subsequently reduce the amplitude but extend the frequency range of the mode. The quality factor describes the relationship between the mass-spring and damping coefficients. A high quality factor represents a large amplitude at the natural frequency with a sharp drop in amplitude as the forcing frequency changes from the resonant value, while a low quality factor represents a small amplitude with a shallow drop in amplitude. The quality factor can be determined theoretically using formula 1.7,

$$Q = \frac{1}{2\zeta}^2 \tag{1.7}$$

where Q is the quality factor and ζ is the damping coefficient. This formula may only be used with a $\zeta < 0.05$.

- Bandwidth – The bandwidth of the gyroscope is the range of frequencies where the displacement of the proof mass is equal to at least half of the resonant peak value. The following formula can be used to determine the bandwidth of the gyroscope,

$$\Delta f = f_0/Q, \tag{1.8}$$

where Δf is the range of frequencies and f_0 is the natural frequency. Similarly to the quality factor calculation, the damping coefficient must be less than 0.05.

1.3 MEMS Actuators

MEMS actuators are required for a variety of applications including ink-jet printers, RF, micro-pumps, micro-manipulators and inertial sensors. The most common micro-actuators are thermal and electrostatic but other types include magnetic and piezoelectric actuators.

1.3.1 Electrostatic Actuation

Previously, the actuation method used to drive the proof mass in vibratory micro-gyroscopes has been electrostatic actuation. In most macro scale applications electrostatic forces are not used as a method of actuation since the electrostatic force arising from the Coulomb charging of parallel plates decreases with the square of distance, assuming that the effect of the electrical field on the edges of the plates is negligible.

$$F_e = \frac{\varepsilon A V^2}{2d^2} \qquad (1.9)$$

where F_e is the force from the electric field, ε is the permittivity of air, A is the area of the parallel electrode plates, V is the charge of the parallel plates and d is the distance between the plates. In macro scale systems, the voltage required is too great to produce a significant force due to the large distance between the two electrode plates. However, in the micro scale, the distance between the two electrode plates is relatively small.

There are two popular MEMS electrostatic actuators; the parallel plate actuator, shown in figure 1.3, and comb drive actuator shown figure 1.4. Both actuators operate by the same electrostatic forces, but act in different directions due to different configurations of the plates. In parallel plate actuators, there are two sets of fingers or plates; one is anchored to the substrate and faces the other, which is connected to flexures and is free to move. Parallel plates provide a large facing area which enable large force but only for small motions due to rapid change of force when the gap between the two plates varies. The dramatic force change causes instability in the actuator.

Therefore, it is only suitable for applications requiring small motion with large force. Comb drive actuators operate perpendicular to the working plane and use symmetrical fingers with repulsive electrostatic forces. They are capable of larger displacements compared to parallel plate actuators.
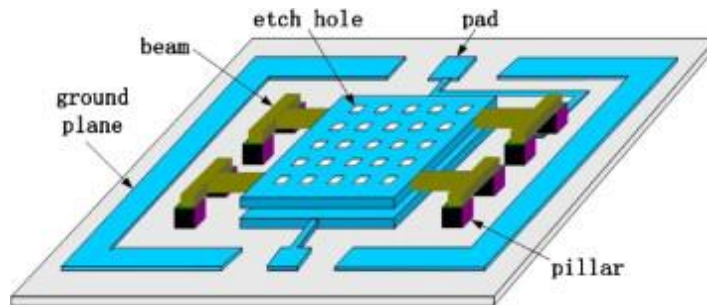
a) Schematic illustration of the general structure of parallel plate actuator
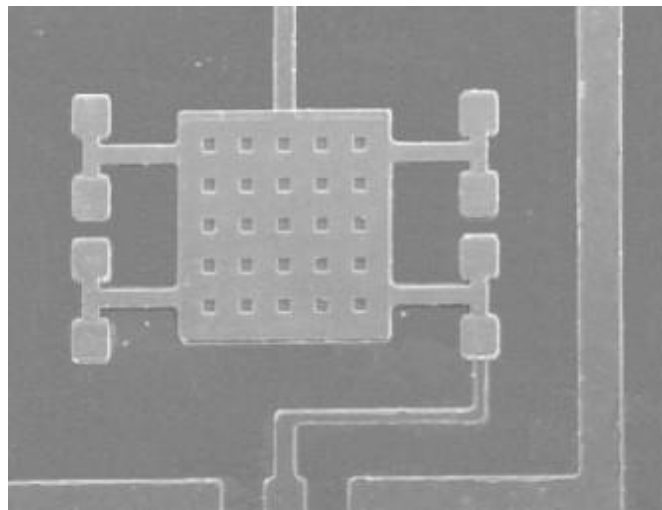
b) Micrograph of the prototype

Figure 1-1-3 - Parallel plate actuator.[3]
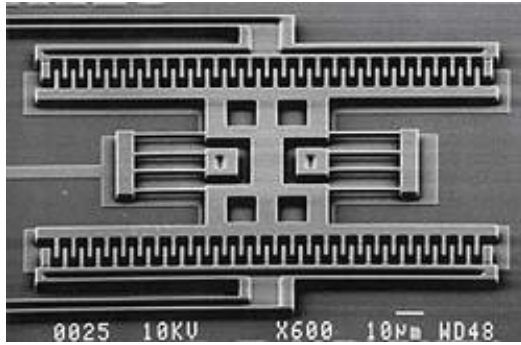
a) Image of an in-plane comb drive actuator,   **b) Close-up of the fingers**
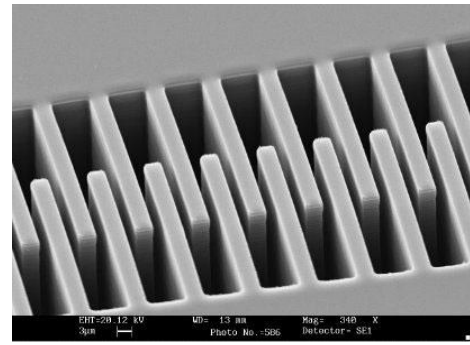
Figure 1-1-4 - Micrograph of an in-plane Comb Drive Actuator.[4]

The advantage of using electrostatic actuation methods is that they require very little power because very little current is required to charge the plates due to their low specific electrical capacity. However, the voltages are relatively high for most applications including vibratory gyroscopes, typically 30V to 200V range[56] and hence are difficult to integrate with other CMOS (Complimentary-Metal-Oxide-Silicon) circuits.

1.3.2 Thermal Actuation

Thermal actuators use thermal expansion to generate forces and displacement, which is facilitated by asymmetrical geometry or the use of materials with different thermal expansion properties. The volume of a material expands as the temperature increases and a force is created as a result if a mechanical constrain is applied to the structure. Thermal expansion is often considered in the longitude direction since most of MEMS devices are thin and narrow; their thickness and width are far smaller compared to their length.

Thermal actuators can be heated by either direct or indirect heating. Direct heating increases the temperature of the actuator by inducing a current through the volume of the expanding elements where heat is generated through the materials resistance to the current. This physical process is called Joule heating and is more efficient in comparison to indirect heating. Indirect heating does

not generate heat within the structure but instead uses a proxy source to heat it using conduction, radiation or convection. This allows for greater flexibility in the device design and allows for greater control but is less efficient and has a slower response.

Using direct heating methods, Joule heating is given by the formula:

$$Q_{GEN} = I^2 \cdot R \cdot t \tag{1.10}$$

Where Q_{GEN} is the energy is joules, I is the current flowing through the structure in amps, t is the amount of time in seconds and R is the resistance of the structure in ohms that is characterized by the formula below:

$$R = \frac{\rho l}{A} \tag{1.11}$$

Where ρ is the material resistivity, l is the length and A is the cross-sectional area of the structure. The material resistivity is dependent on the temperature and changes during operation of the actuator.

Some of the energy generated from Joule heating is dissipated into the surroundings through radiation, convection and conduction so the temperature of the device can be found by accounting for these terms:

$$Q_{GEN} - Q_{RAD} - Q_{CONV} - Q_{COND} = m \cdot c \cdot \Delta T \tag{1.12}$$

Where m is the mass of the structure in kilograms, c is the specific heat capacity of the material in joules per kilogram-kelvin and T is the temperature in kelvin. The Q terms represent the energy generated and the energy lost from radiation, convection and conduction in joules. Radiation is not very significant at the temperatures that thermal actuators operate in and convection is negligible in the micro-scale, thus they are typically ignored. Conduction is the dominant heat transfer mode where most energy is transferred to the substrate which acts as a large heat sink.

Strain, ε, and therefore the displacement of the actuator can be found from the temperature according to the thermal expansion strain formula:

$$\varepsilon = \beta \Delta T = \Delta L / L \qquad (1.13)$$

Where β is the material specific, linear thermal expansion coefficient defined as:

$$\beta = \frac{(\Delta L / L)}{\Delta T} \qquad (1.14)$$

The force can be found from the stress, σ, the Young's modulus of the material, E, the strain and the cross-sectional area:

$$\sigma = E\varepsilon \qquad (1.15)$$

$$F = A\sigma \qquad (1.16)$$

Thermal actuators are compact, reliable, require low voltages and generate large displacements in comparison to electrostatic actuators. The three most common thermal actuators are bimorph, hot/cold arm and chevron.

Bimorph actuators are typically in the form of a cantilevered beam made from two separate material layers. As the beam heats up, the beam bends toward the direction of the lower thermal expansion coefficient layer. MEMS bimorph actuators have fast response times and can vibrate at relatively high frequencies due to its low specific thermal capacity and light weight.

Hot/cold arm actuators use geometrical asymmetry, usually containing a thin and wide arm to create displacement. The resistance in the thin arm is greater than the thick arm due to its smaller cross-section causing it to generate more heat and expand more than the thick arm. The actuator bends towards the thick arm due to the difference in arm lengths.

Chevron actuators also use device asymmetry to generate displacements. Several "V" shaped beams are placed in parallel and fixed at both ends. The point of the chevron actuator moves

adjacent to the beams when the beams expand due to Joule heating. Chevron actuators generate large forces but are limited in the displacement they can produce.

Thermal actuators are also typically restricted to MEMS applications. The energy required to heat a macro-scale actuator is uneconomical and the heating and cooling response would be slow due to the low surface to volume ratio compared to MEMS sized devices. To produce significant travel the actuator must be relatively long, which would also increase the material cost. MEMS thermal actuators suffer from the same drawbacks but scaling laws dictate that they are negligible in comparison.

Depending on the material and design of a thermal actuator it can use less voltage compared to electrostatic actuators. Using a material with a high conductivity will greatly reduce the resistance and the electric potential across the actuator; however the current will also increase and will ultimately require more power compared to electrostatic actuators. The lower voltage requirement of thermal actuators allows them to be easily used with IC`s and need less supporting actuation signal circuitry, which also require power to operate. The thermal actuation forcing frequency is also similar to the natural frequencies of MEMS gyroscopes, which also helps reduce the operational power. Thus, it is within reason to expect that a thermal actuator can operate under a lower power requirement compared to a similar electrostatic actuator.

1.4 Fabrication Fundamentals

Traditional machining methods are commonplace and well understood in macro-scale manufacturing settings. The same techniques are difficult to apply to the micro-scale. Material property discontinuities become significant at sub-millimeter levels as grain boundaries span larger proportions of the width of the tool this are more prone to failure. Alternative methods are required for smaller features and greater resolution. Lithography and molding methods are well-

understood technologies that can be used for microfabrication applications. The parallel characteristic of the majority of lithography techniques make them suited for high-volume production. Lithography methods are typically restricted to lower dimensionality structures and the use of specific materials that are sometimes a design constraint. Traditional machining technologies can be used on a wider variety of materials and allow for more control and higher dimensionality structures. Research in this field has led to several promising fabrication technologies such as laser micromachining and micro-electro-discharge machining that are serial processes that allow for better dimensionality.

1.5 Thesis Outline

The objective of the work outlined in this thesis is to theoretically and experimentally determine the modal behavior of three different gyroscopic sensor models and compare the performance of each model. A Finite Element Analysis (FEA) is performed on each model to determine the mode shapes of the gyroscopic sensors experimentally. The information gained by performing these simulations will assist in interpreting the experimental results. The mode shapes are determined experimentally by separate in-plane and out-of-plane tests that produce frequency response data. The insights gained from these tests will help predict the performance of the sensors. Comparing the simulation and experimental results will improve the theoretical model, which can be used to assist in the design of future MEMS vibratory gyroscopic sensor designs.

Chapter 2

Literature Review

2.1 Lithography Modes

Lithography is a general term that encompasses various geometrical structuring microfabrication techniques. The two lithography modes that are involved in the Metal MUMPS and Micragem processes, which were used to fabricate the micro-gyroscopes, are pattern etching and deposition. Optical lithography is typically used in both processes for patterning. They are inherently parallel, which is useful to increase throughput but are also highly material critical.

In optical lithography, a mask is used to transfer a pattern to a deposited photosensitive material, commonly called a resist, by exposing it to radiation. Radiation changes the material properties of the resist, which makes it either susceptible or resistant to the developer solution. In a positive resist the radiation increases the susceptibility of the resist to the developer, which is shown in figure 2-1 below. In a negative resist the radiation hardens the resist to the developer.
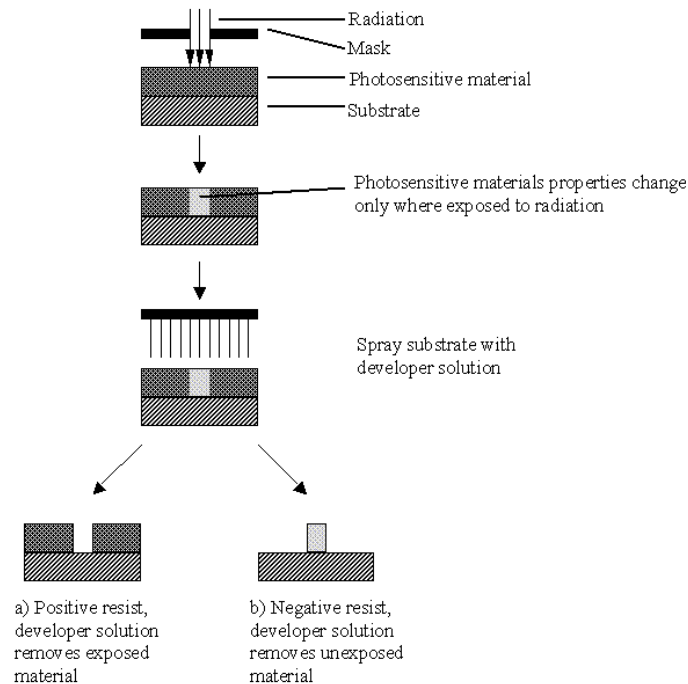
Figure 2-1 - Photolithography process steps[7].

The resist can then be used as part of the geometrical structure or as a sacrificial material that will eventually be completely removed by the end of the process. When used sacrificially, an additive layer can be deposited to fill in the gaps in the resist and then the resist can be removed to transfer the pattern or an etchant can be used to remove material from a layer beneath the resist.

2.1.1 Etching

Etching can be separated into two classes; wet and dry etching. The anisotropy, etch rate, and material selectivity are all important considerations when choosing which process to use. Anisotropic etching, shown in figure 2-2 on the left, has etching rates that are faster in the vertical direction compared to the horizontal. Anisotropic pyramid shaped structures can be created by etching material between crystallographic planes. Isotropic etching, shown below on the right, has an etching rate that is equal in both horizontal and vertical directions, which produces structures that have a more rounded shape. Undercutting of the mask occurs in both cases and has to be accounted for in the mask design.

17
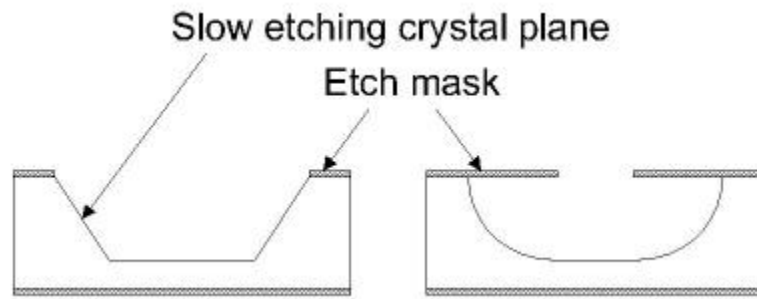
Figure 2-2 - Anisotropic (left) and isotropic (right) wet etching.

Wet chemical etching is typically isotropic but anisotropic structures can be created by taking advantage of crystallographic plane orientations. Alternatively, most dry etching is anisotropic regardless of the presence of crystallographic planes. The feature side walls are almost completely vertical and hence there is no undercutting of the mask.

There are three types of dry etching; sputter, plasma and reactive ion etching (RIE). Sputter etching involves physically bombarding the workpiece with ions to remove the unmasked material. Plasma assisted etching uses heat, high pressure and reactive gas ions to induce chemical reactions on the surface. In contrast to the other types of dry etching, plasma etching is isotropic. Preventative measures must be taken when using plasma etching to ensure that chemical by-products do not build up and interfere with the etching process. Reactive ion etching combines sputter and plasma etching by bombarding the exposed material with reactive ions. The anisotropy of side walls can be controlled by adjusting the pressure and energy of the beam. In deep reactive ion etching (DRIE) a polymer is deposited on the substrate first and is subsequently removed by the physical bombardment of ions. The polymer dissolves slowly in the reactive gas leaving it to coat the side-walls of the structure and preventing the reactive ions from etching in the horizontal direction. The structures produced by DRIE are highly anisotropic; 50:1 aspect ratios are possible, and can be up to 100μm deep.

Dry etching is expensive compared to wet etching and is subject to worse material selectivities. However dry etching allows for greater dimensional control and does not suffer from contamination issues from the etchant such as with wet etching. The etch rate for both types is highly dependent on the operational conditions. The desired geometrical structure of MEMS devices will typically determine which etching process must be used.

2.1.2 Deposition

While there are many deposition techniques available, chemical vapour deposition (CVD), physical vapour deposition (PVD), thermal oxidation, epitaxy, spin coating and electroplating are the most common in thin films.

Using the CVD process, the wafer is placed inside a reactor chamber where a chemical reaction occurs between gas molecules. The product of the reaction gets deposited on the wafer as a thin film. There are several types of CVD that can be used for a variety of materials, which makes CVD an enabling technology for MEMS devices.

Similarly, PVD involves the deposition of a thin film from a vapour to a wafer; however PVD does not require a chemical reaction for the material deposit to take place. The film can be either evaporated or sputtered onto the wafer. Low pressure and high temperatures are used to vaporize the thin film material, which is then deposited on the wafer during evaporative PVD. Sputtering uses lower operating temperatures than evaporation but still requires low pressures. The atoms from the source material are transferred to the wafer by bombarding the source with ions. The energy from the collision is enough to eject atoms from the source in the form of vapour, which is then deposited on the wafer. PVD is cheaper and less dangerous to the wafer compared to CVD but the quality of the thin film is usually worse.

Thermal oxidation is a relatively simple and cheap deposition technique, which is limited to materials that can be oxidized. The most common application is silicon dioxide, also referred to as an oxide layer. The wafer is placed in a high temperature, oxygen-rich environment to speed up the diffusion of the oxygen atoms in the oxidized material. Oxidation time increases with the thickness of the material so there is a constraint on the thickness of the oxide layer.

Epitaxy is similar to CVD but gas or liquid can be used. The substrate acts as a seed layer that defines the epitaxial growth of the layer being deposited on it. For example, an amorphous silicon wafer will cause an amorphous silicon layer to grow; however the seed layer and epitaxial layer do not necessarily need to be the same material. Thick films greater than 100μm with high growth rates are possible using epitaxy.

Spin coating is a useful method for depositing thin polymer films. The material is dissolved in a solvent and then either sprayed or spun onto the wafer. The solvent is evaporated and a thin film remains.

2.1.3 Electroplating

Electroplating is a relatively mature fabrication technology in both the micro and macro scales. IBM first used electroplating as a microfabrication process in the 1960s and the fundamental operating principles have not changed since then. The process involves using lithography to define a mould and electrodeposition to form the structure. The diagram, in figure 2-3 below, shows some of the steps involved in using electroplating to fabricate a comb-drive resonator.
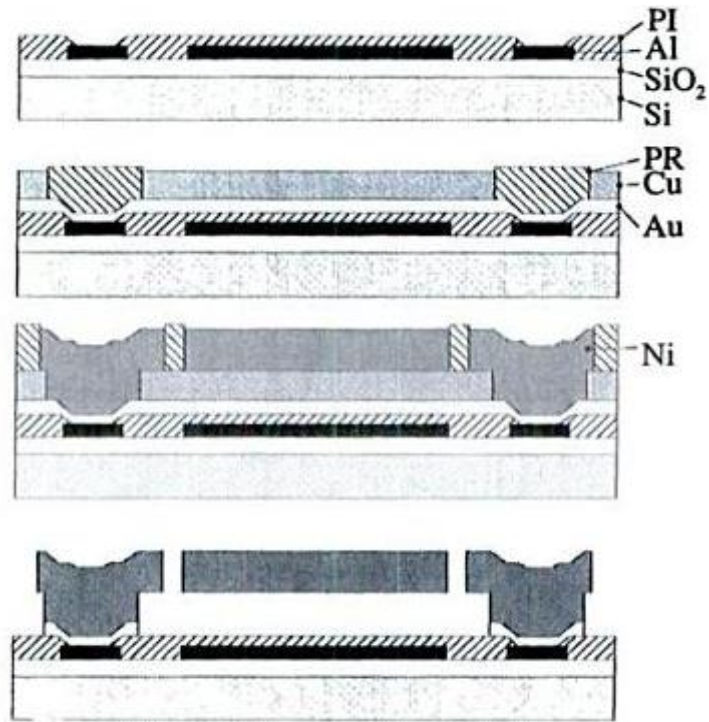
Figure 2-3 - Cross-sectional diagram of an electroplated nickel comb-drive resonator[8].

The first cross-section shows an oxidized silicon wafer with aluminum electrical interconnects used for ICs and electrodes. The polyimide layer is used to protect the aluminum from the environment. A gold plating base is added that will be used to grow the subsequent nickel layer from a nickel sulphamate bath. The positive photoresist mould, labeled PR in the diagram, is defined using optical lithography and a sacrificial copper layer is grown in a copper pyrophosphate bath. The photoresist is stripped and the nickel layer is grown. The resonators are released by selectively etching the copper and gold base. An SEM image of a released comb-drive finger is shown in figure 2-4 below.
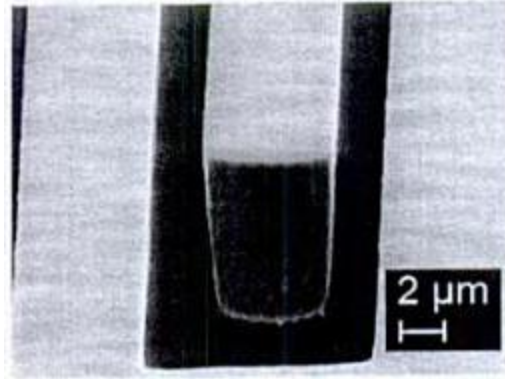
Figure 2-4 - SEM image of a comb-drive finger fabricated with the electroplating process.

The finished product has a high aspect ratio, low surface roughness and low residual stress, which makes electroplating an attractive geometrical structuring technique for MEMS devices. Electroplating requires few process-steps and allows for tall structures with high aspect ratios that are not possible with other microfabrication processes. However, the process involves harmful chemical solutions that can damage preceding layers, which restricts the materials that can be used.

Electroplating is commonly used in a process called LIGA that combines X-ray lithography, electroplating and moulding. Recent reports state that LIGA is capable of a lateral resolution better than 0.5 microns, 1.3mm structural depth, steep walls up to 100nm per 100 microns and a side-wall surface roughness of 20nm root-mean square depending on the X-ray wavelength used[9]. However, the dimensional control of LIGA requires highly-focused X-ray beams that are generated by synchrotron radiation, which are relatively expensive. By taking advantage of economies-of-scale the cost per device can be lowered by using moulding.

2.1.4 Anodic Bonding

Anodic bonding is a geometrical structuring technique that involves the assembly of a silicon substrate to a borosilicate glass wafer by means of an electric field and thermal bonding. The process involves a vacuum chamber, two electrodes that apply an electric field of 200-1000V across the wafers and heating plates that are used to assist the migration of sodium and oxygen atoms. The temperature range is typically controlled to be between 200-450°C. Once a field is applied, with the glass being the cathode and the silicon wafer being the anode, the sodium and oxygen ions migrate towards the electrodes as shown in the diagram below, which causes the two wafers to be electrically attracted to one another. Oxidation at the borosilicate glass-silicon interface bonds the two wafers preventing them from falling apart once the electric field is removed. Very little bulk modification in the silicon wafer is caused by this process.

cathode

$4Na^+ + 4e^- \rightarrow 4Na^0$

anode

$Si + 2O^{2-} \rightarrow SiO_2 + 4e^-$

750V

Si
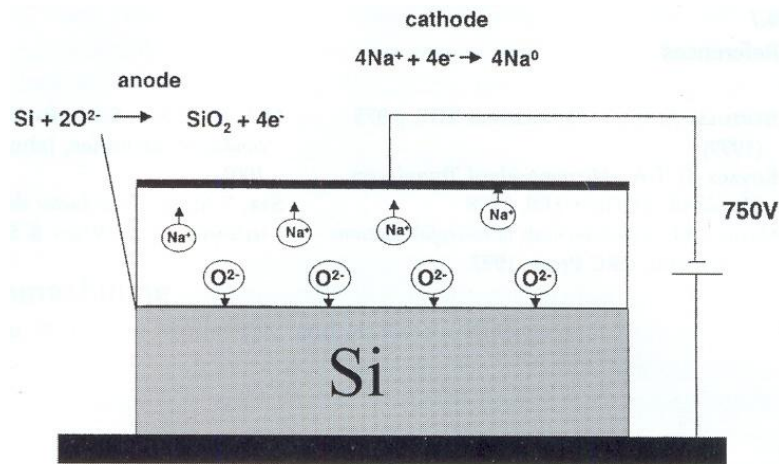
Figure 2-5 – Diagram of anodic bonding between a borosilicate glass and silicon wafer[10].

2.2 Microfabrication Processes

2.2.1 Metal Multi-User MEMS Process (MUMPS)

The metal MUMPS process was designed for general purpose micromachining for MEMS devices. An electroplated nickel layer is used as the primary structural material and also for electrical interconnects.

The process begins with an n-type (100) silicon wafer. A 2μm oxide layer is then grown on the wafer followed by a 0.5μm sacrificial phosphosilicate glass (PSG) layer, which is then patterned using wet chemical etching. A 0.35μm silicon nitride layer, used for electrical isolation, is deposited as well as a 0.7μm polysilicon layer used for resistors and additional mechanical structures. The polysilicon layer is lithographically patterned using RIE and a second 0.35μm silicon nitride layer is deposited. Both nitride layers are then patterned by RIE as well. Another 1.1μm PSG layer is added and then annealed at 1050°C for 1 hour. The oxide is etched away and a metal layer, used for anchoring, is deposited and patterned using lift-off. 500nm of Copper and 50nm of Titanium is deposited as a plating base layer and nickel is electroplated to a thickness of 20μm with a 0.5μm gold layer electroplated on top. A photoresist stencil was used to pattern the nickel and give it an anisotropic structure. Once the stencil is removed a 1.3μm gold sidewall is electroplated. The structure is released using a 49% HF solution to remove the sacrificial PSG and the oxide layer[11].

This process was used to fabricate both an electro-thermally driven and electrostatically driven gyroscope. The cross-sectional diagrams below outline the Metal MUMPS steps as it applies to the microgyrscope designs. The thickness of each layer is exaggerated so that it can be seen.
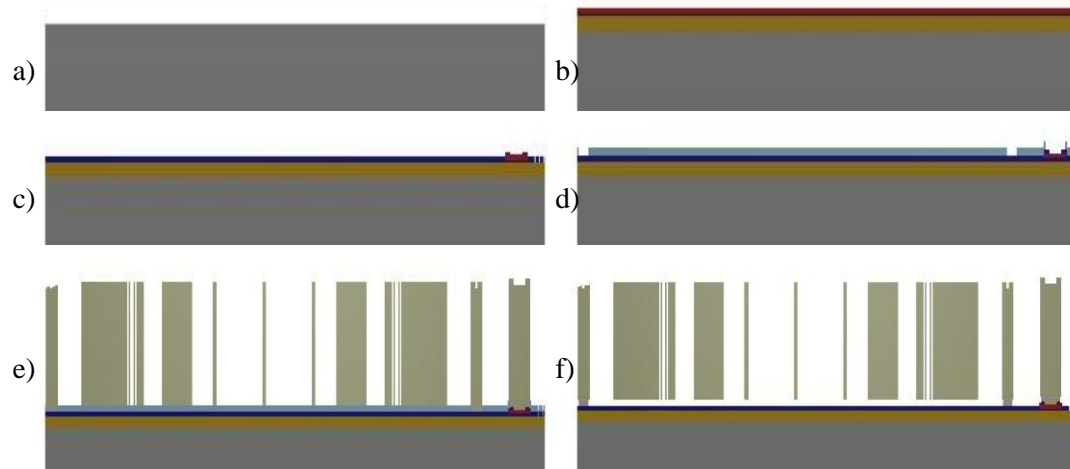
Figure 2-6 - Cross-sectional view of an electrostatic gyroscope fabricated with the Metal MUMPS process.

Figure 2-6 a) shows the plain silicon wafer. The oxide, PSG, silicon nitride and polysilicon layers are then added in b). However, the oxide layer cannot be seen because it was not utilized in this case. In c) the polysilicon is patterned, followed by an additional nitride layer, which is then patterned as well. The cross-section d) in figure 2-6 shows the second, patterned PSG layer after the annealing process. The gaps in the PSG layer are used to affix the subsequent nickel layer to the substrate. In e), the plating base layer is added and the nickel is grown by electroplating in the gaps between the photoresist. Step f) shows the released structure after the sacrificial base layers have been etched away. A 3 dimensional view of the final product can be seen in the figure below.
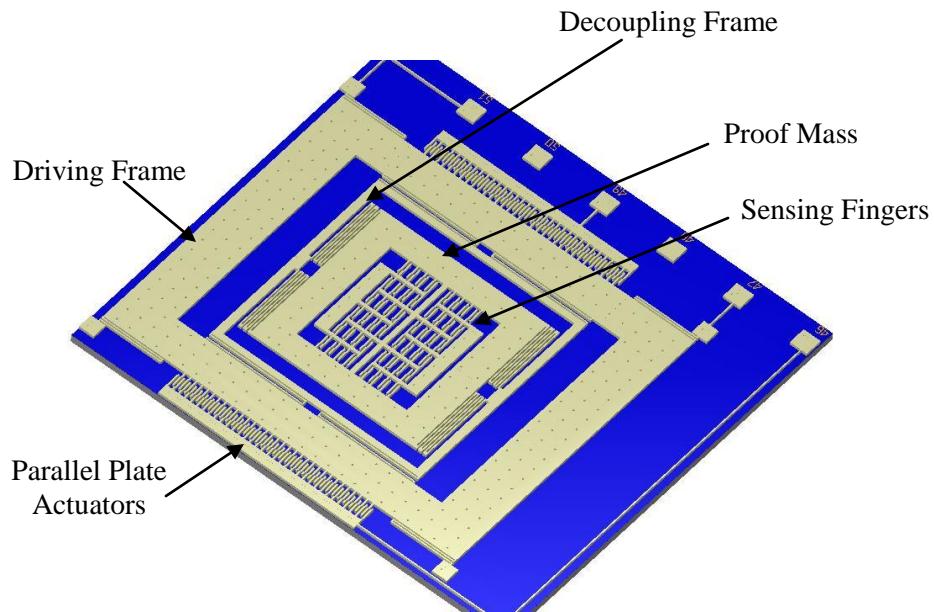
Figure 2-7 - 3D view of an electrostatic gyroscope using the Metal MUMPS fabrication process.

2.2.2 Micragem Silicon-On-Insulator (SOI)

Micragem is a microfabrication process developed by Micralyne Inc. and CMC Microsystems for MEMS applications. The technology allows for fully suspended metal electrodes and three different gap depths, which makes the process comparatively versatile and increases the design possibilities for micro-gyroscopes.

The process begins with a 500μm glass wafer that is then selectively etched using to add gaps or cavities to the structure. Metal electrodes and bonding pads consisting of 500Å Titanium-Tungsten and 2000Å gold are added using surface patterning. An additional SOI layer is then anodically bonded to the glass and the silicon handle and buried oxide is etched away to leave the 10μm single crystal silicon layer (SCSi) behind. An additional metal layer can be deposited on top of the SCSi layer at this point and patterned using lithography. The final step is to etch the SCSi layer using DRIE[12].

These steps are shown visually below where the Micragem process was used to fabricate an electrostatically driven micro-gyroscope. The thicknesses have been scaled to show off the significant features of each layer.
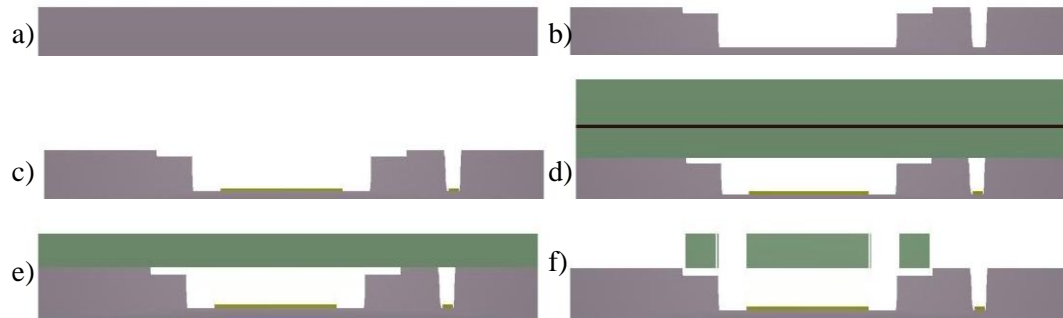
Figure 2-8 - Cross-sectional views of an electrostatic gyroscope using the Micragem process.

The cross-sectional diagram in figure 2-8 a) shows the bare glass substrate. The surface is etched to add gaps and cavities in the structure in b). The bonding pads are added in the c), which will be used to electrostatically actuate the subsequent SCSi layer. The next diagram, d), shows the SOI layer being joined to the original substrate using anodic bonding. The oxide and silicon handle are removed by etching in e) and then the SCSi layer is patterned in the last phase. The end result can be seen in the figure below.
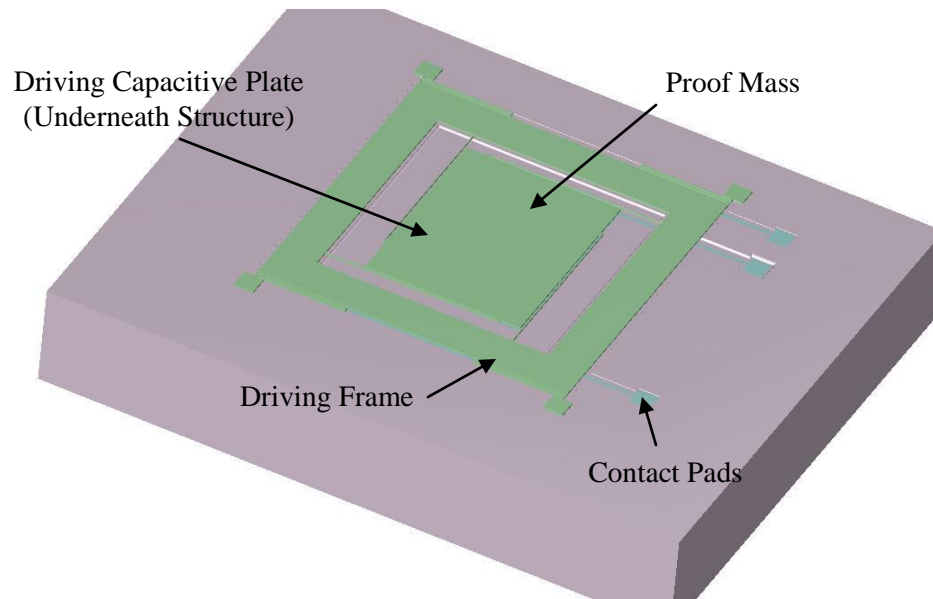
Figure 2-9 - 3D view of an electrostatic gyroscope using the Micragem process.

2.3 Previous Micro-gyroscope Research

The first MEMS inertial sensor was an SOI accelerometer developed by Roylance et al. in 1979 for applications that required small transducers[13]. This development pioneered MEMS inertial sensors, which influenced the invention of the first micro-gyroscope created in 1988 by Draper Labs and was presented at the Navigation and Control Conference[14]. The device was assembled by hand and contained a silicon member and a separate glass slide containing the electrodes. Their research was instrumental in verifying the micro-gyroscope concept and establishing a model for which proceeding gyroscopes would be compared.

In 1991, Draper Labs published a paper on another double-gimbal micro-gyroscope supported by torsional flexures with an on-board buffer circuit to reduce noise and made from single-crystal silicon. The operational characteristics of the device are graphically shown in figure 2-10 below. The footprint of the outer gimbal was $350 \times 500 \mu m^2$; it was hypothesized by Boxenhorn et al. that a larger gyroscope would elicit greater performance. The gyroscope was designed to detect the

angular velocity of the out-of-plane, z-axis, component of the rotating system that it was mounted to. To detect this angular rate, an oscillating torque was applied in the drive axis electrostatically by silicon p-type electrodes on the ends of the device. The Coriolis force caused the inner frame to oscillate in the output axis direction at the same frequency as the driving frequency and at an amplitude that was proportional to the magnitude of the angular rate of the input. Ideally, the device would be driven at the resonant frequencies of the sensing gimbal to maximize the resultant amplitude. Capacitive sensors were used to detect the resultant motion of the inner frame. When operated within a vacuum at 3kHz a 4°/s/$\sqrt{\text{Hz}}$ resolution was demonstrated.
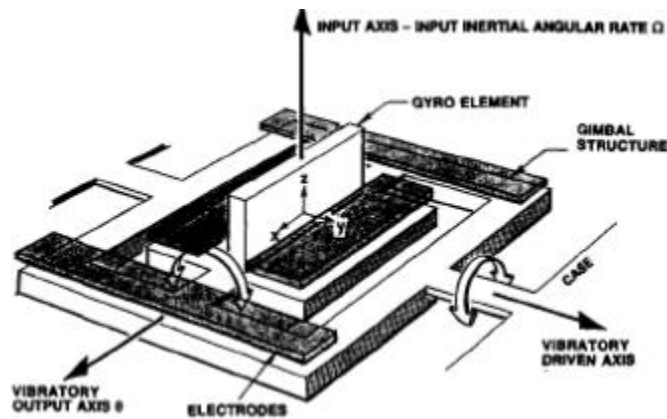
Figure 2-10 - A novel double-gimbal micro-gyroscope by Draper Labs

The first lateral-axis gyroscope was developed Tanaka et al. in 1995[15]. The substrate was a p-type silicon wafer that was selectively doped to make electrodes. Oxide and nitride layers were added for insulation. A 1µm sacrificial PSG layer was deposited to separate the subsequent 5µm polysilicon layer from the substrate. The device was slightly larger, compared to Draper Labs double-gimbal gyroscope, at a footprint of 400x800µm^2.
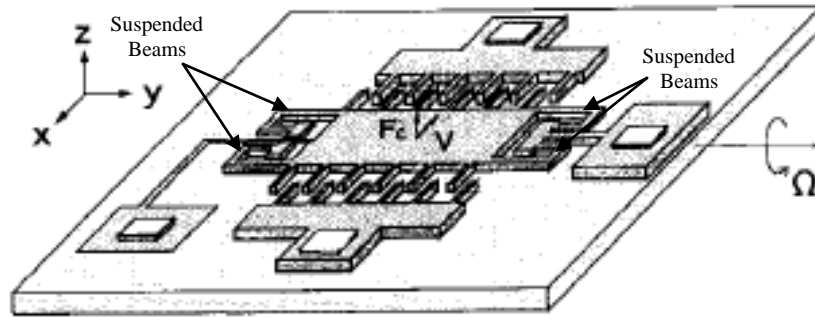
Figure 2-11 - A planar, coupled micromachined vibratory gyroscope.

Electrostatic comb actuators and sensors were used to drive and detect the motion of the proof mass respectively. In figure 2-11 above, the proof mass was suspended by 4 beams and was driven in the x-direction by an AC voltage. An angular velocity applied in the y-direction causes the proof mass to vibrate out-of-plane in the z-direction due to the Coriolis force. Electrodes beneath the mass detected the displacement in the z-direction, which was proportional to the angular velocity. Using a 5V DC bias and 10V peak-to-peak AC driving voltage operating at the driving mode resonant frequency of the device, 12.475kHz, and at an atmospheric pressure below 0.1Pa a resolution of $7^{o}/s/\sqrt{Hz}$ was found. A piezoelectric actuator was mounted to the gyroscope to detect mechanical Q factors at various pressures. At 1Pa Q factors of 2,800 and 16,000 were found for the driving and sensing modes respectively, which are relatively sharp peaks.

Tanaka et al. also conceived of a technique to adjust the driving and sensing mode frequencies so that they are close to each other in 1995. The technique involves modifying the stiffness in the supporting springs. Ion milling was used to decrease the height of the spring, therefore reducing the sensing mode resonant frequency, and RIE was used to modify the width of the spring reducing the driving mode resonant frequency.

Until Juneau et al.'s paper in 1997 only single input axis gyroscopes had been researched[16]. Their dual input axis device was manufactured using Analog Devices Inc. proprietary surface micromachining process. The functional concept requires symmetry in two planes normal to the substrate, which is depicted in the figure below. The proof mass of the gyroscope is a 2µm thick circular disk with 150µm radius. Four 180µm long symmetrically placed beams were used to suspend the mass 1.6µm above the substrate and to oscillate the inertial element orthogonally to the substrate.

a)   b)
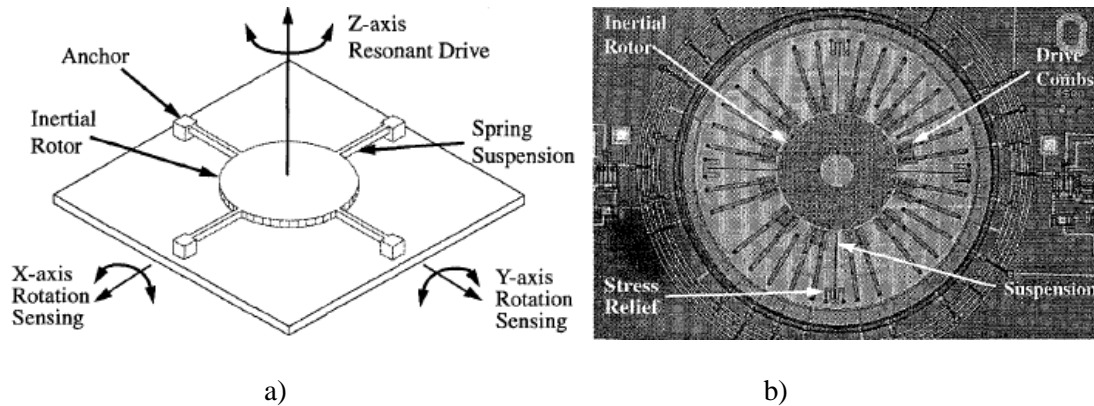
Figure 2-12 - a) Conceptial diagram of a dual input axis gyroscope. b) A micrograph of the proposed gyroscope.

The proof mass of the gyroscope was a 2µm thick circular disk with 150µm radius. Four 180µm long symmetrically placed beams were used to suspend the mass 1.6µm above the substrate. Drive combs, shown in figure 2-12 b) above, oscillate the inertial element orthogonally to the substrate. Sensing was performed by four electrodes beneath the proof mass.

During operation, the inertial mass was oscillated about the z-axis. Any rotation about the x-axis would induce an oscillating torque, at the frequency of the drive oscillation, on the proof mass about the y-axis and vice versa due to the induced Coriolis force. The torque tilts the proof mass, which was then detected electrostatically using the electrodes underneath. Using an open-loop driving signal the team was able to demonstrate resolutions of 0.24 °/s/√Hz by matching the

driving and sensing modes but with high cross axis sensitivity. Sensing axis coupling was reduced when the driving frequency was unmatched with respect to the sensing natural frequency but increases the noise floor. Juneau et al. predicted that using closed-loop force feedback control would reduce the cross axis dependency and increase device performance.

Mochida et al. were able to reduce mode coupling mechanically by using separate beams for the driving and sensing modes in 1999[17]. In their study they fabricated a similar device to Tanaka et al. and investigated the cross axis sensitivity and noise floor of both to determine the effect of coupling. The device was fabricated from an SOI substrate. The mechanical structure was defined by etching the top silicon layer using RIE. A glass substrate was then wet etched and gold and chromium layers were patterned as electrodes. The glass and SOI layers were then anodically bonded together and the silicon handle was etched. The process is similar to the standardized Micragem fabrication process. The resultant structure is shown pictorially in figure 2-13 below. The size of the resonator was $800x1200x50\mu m^3$.
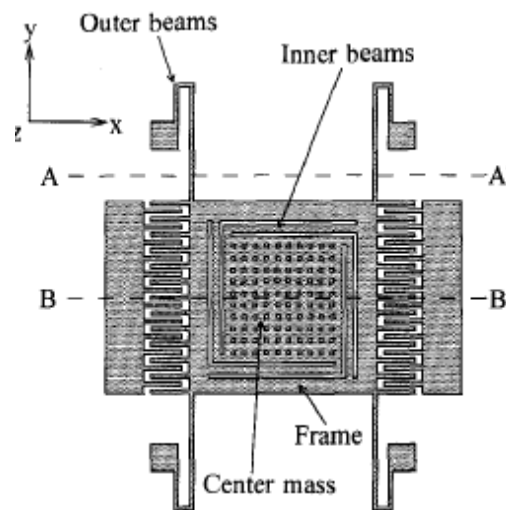
Figure 2-13 - MEMS gyroscope utilizing independent drive and sense beams for mode decoupling.

The decoupling frame contains four springs allowing the proof mass to move in the z-direction. The frame was supported by four beams similarly to Tanaka et al.'s design. Ideally, the deflection of the inner frame does not change with a deflection in the outer beams and vice versa; however some coupling was observed in the FEM model but very weak in comparison. Figure 2-14 below shows the intended deflection of the beams in their respective modes of operation.
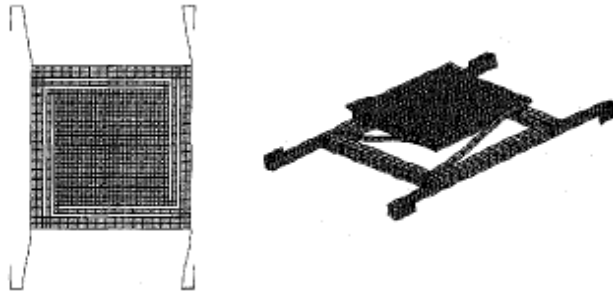
Figure 2-14 - Drive mode beam deflection (left) and sensing mode deflection (right).

Using laser interferometry the cross axis coupling was experimentally measured and compared. The path of the proof mass in the x-z plane when driven electrostatically was elliptical in shape for both gyroscopes. However Mochida et al.'s device had half of the x-z amplitude ratio compared to Tanaka et al.'s device for all tested frequencies. The noise was greater for Mochida's design, which is likely due to less mechanical stability due to the increased DOF of the system. Overall, the reduced coupling improved the resolution by 100 times that of Tanaka's device with a resolution of 0.07 °/s/√Hz at 10Hz bandwidth while operating at an environmental pressure of 100Pa.

One of the biggest challenges in the previous micro-gyroscope designs were the variability in output due to residual manufacturing stresses and environmental temperature and pressure fluctuations. Previously, this has been compensated by post-processing of on-chip electronics. Acar et al. were able to develop a micro-gyroscope that compensated for fluctuations in the

environment and residual stresses mechanically, which helped reduce the complexity and increase the robustness of the system[18].

The gyroscope uses two DOF for the sensing mode and one DOF for driving and incorporates a decoupling frame. The footprint of the device is 4x4mm^2. An SEM image of the device is shown in figure 2-15 below.
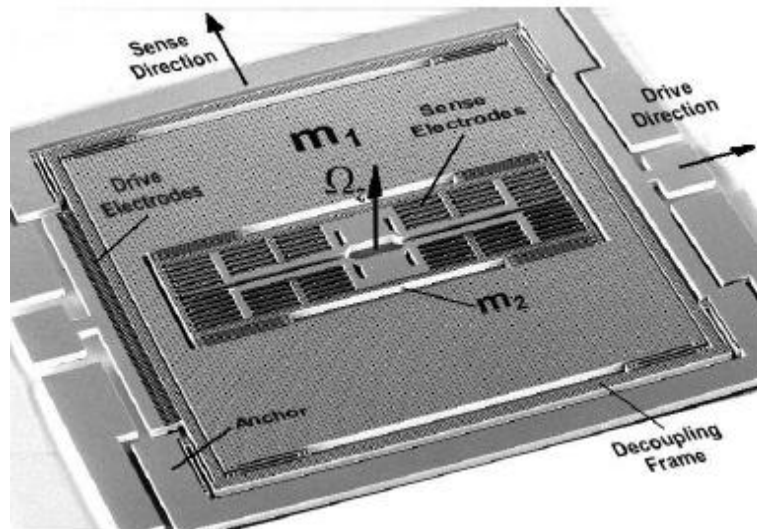
Figure 2-15 - SEM image of a robust 3 DOF mechanically decoupled gyroscope.

The mass m_1 is free to move in the driving and sensing direction while mass m_2 is constrained in the driving direction with respect to mass m_1. The two masses oscillate together in the drive direction using comb-drive actuators and their response in the sensing direction is the sum of the response of both masses in the sensing direction. This displacement was detected using parallel plate capacitive sensors. This produces two separate response peaks since the two masses have separate resonant frequencies as shown in figure 2-16 below.
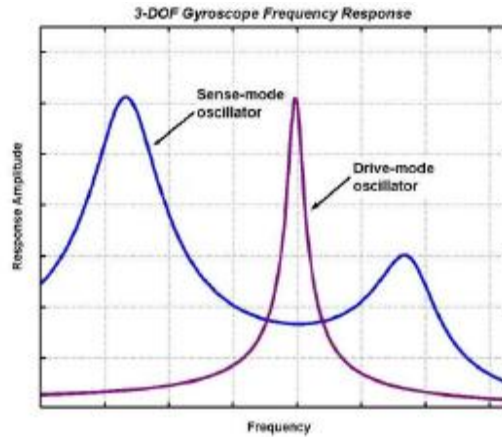
Figure 2-16 – Frequency response curves of a 3 DOF gyroscope.

The masses were driven between the two sensing peaks where the response amplitude is flat. In the given frequency range the gain is less sensitive to changes in the natural frequencies of the system making it more resilient to fabrication imperfections and environmental changes.

The device was tested under a variety of environmental conditions. It was found that the flat region between the peaks remained relatively constant despite the variations in temperature and pressure while the amplitude of the peaks decreased with variations in pressure and shifted with changes in temperature. The device was installed onto a rate-table and excited using a 25V DC bias with a 3V AC drive signal and operating at atmospheric pressure. The resolution of the device was then determined to be 0.64°/s/√Hz at 50Hz bandwidth. Temperature insensitivity was also proven to be 12.2 times less compared to a conventional one DOF micro-gyroscope.

Chapter 3

MEMS Gyroscope Theoretical Modal Analysis

In this section the simulated models of three comparable MEMS gyroscopes are developed using COMSOL Multiphysics finite element analysis software. A 3D modal analysis of each gyroscope was performed to predict the experimental modal frequencies. A simplified analytical model of the thermally-actuated gyroscopic sensor is also presented.

3.1 Thermally-Actuated Gyroscopic Sensor Analytical Model

A visual representation of the fixed anchors and suspended, free-floating mechanical structure is shown in the figure below.
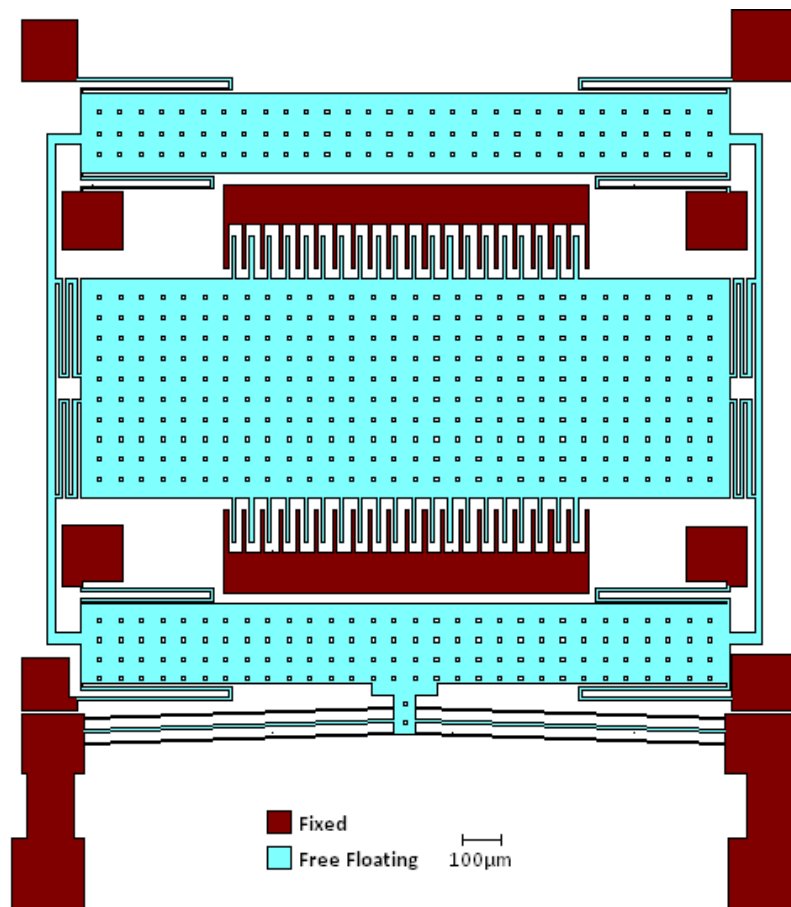
Figure 3-1 - Thermally-actuated gyroscope FEA boundary condition definition diagram.

The device itself has an overall footprint of 6mm^2 and is 20µm thick. The thermal actuator is used to drive the decoupling frame that is suspended above the substrate using eight double-folded flexures that are anchored to the substrate. The proof mass is attached to the decoupling frame using four triple-folded flexures, which ideally act as linear springs in the sensing direction, the x-direction in this case, and act as rigid beams in the other directions. The chevron and double-folded flexures are modelled similarly.

3.1.1 Analytical Model Assumptions and Constraints

An analytical model of the thermally-actuated gyroscopic sensor was developed to support the simulated and experimental results. The picture of the gyroscopic sensor in figure 3-1 can be simplified into the following diagram.
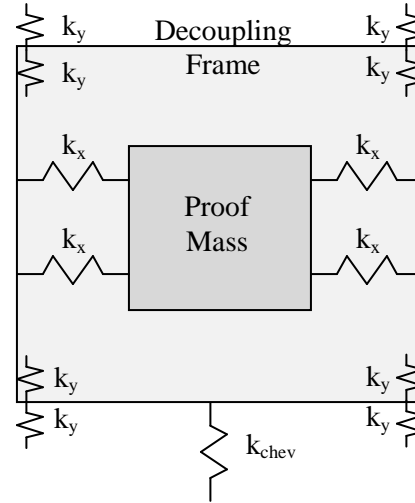
Figure 3-2 - Thermally-actuated gyroscopic sensor in-plane simplified model.

The decoupling frame, with mass *M*, is used to mechanically decouple the proof mass, of mass *m*, from the motion of the driving frame. To eliminate any coupling of the proof mass and decoupling frame in the model it must be assumed that $k_y \ll k_x$ and $k_y \ll k_z$ for the double-folded flexures attached to the decoupling frame and $k_x \ll k_y$ for the triple-folded flexures attached to the proof mass. This restricts the system such that there are only 5 DoF present; *x, y, z, θ, φ*. The DoF are shown in a diagram of the proof mass below.
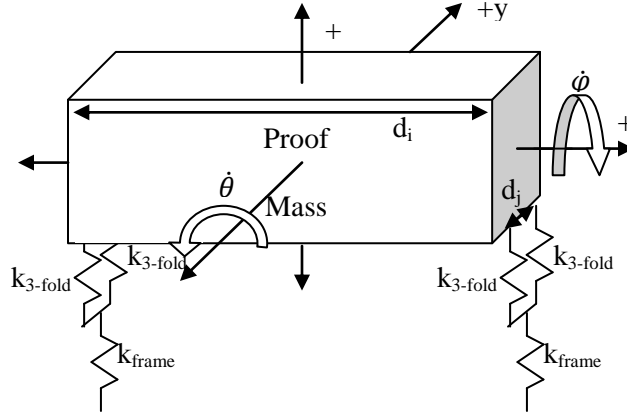
Figure 3-3 - Out-of-plane thermally-actuated gyroscopic sensor model.

Where d_i and d_j are the distances between the triple-folded flexures. Several other assumptions were made to develop the analytical model. It is assumed that the frame is rigid except for the thin section of the decoupling frame in the z-direction, which is treated as a spring, k_{frame}.

3.1.2 Spring Modelling

The displacement caused by the flexures can be modelled by simplifying each fold in the flexure to be an independent cantilevered beam. The displacement of each fold, ζ, can then be summed to receive the total displacement of the flexure. The diagram below shows a force, F, applied to the flexure fold section of length, L.
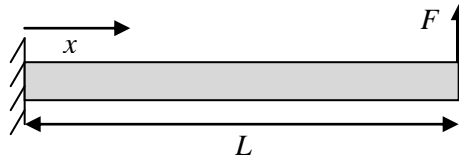
Figure 3-4 - Folded flexure simplified model.

The Euler-Bernoulli relation can be used to find the displacement of the cantilevered section, where E is the Young's modulus of the material, I is the moment of inertia of a beam and M is the moment as a function of the displacement from the wall, x.

$$EI \frac{d^2}{dx^2} \zeta(x) = -M(x) \tag{3.1}$$

Where:

$$M(x) = -F(L - x) , I = \frac{wt^3}{12}$$

The boundary conditions that were used were:

$$\frac{d}{dx}\zeta(0) = 0 , \zeta(0) = 0$$

Solving for this provides the following equation for the displacement at the end of the cantilevered beam:

$$\zeta(L) = \frac{FL^3}{3EI} \tag{3.2}$$

The displacements of each fold can then be summed to receive a total displacement of the flexure. For a triple-folded flexure, there are three long sections of flexure length L_x that are orthogonal to the intended spring direction and four short sections of length L_t that are parallel to the spring direction. The lengths of each flexure are identified in the figure below.
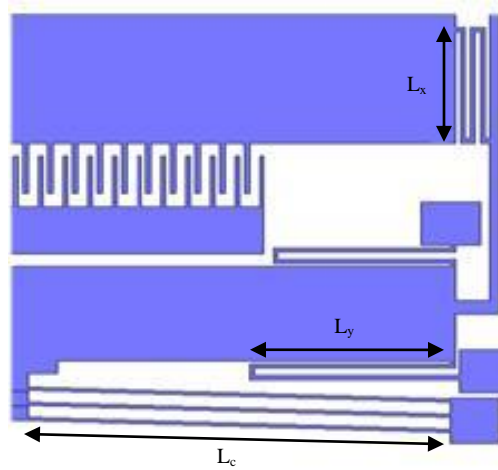
Figure 3-5 - Analytical modelling of the flexures.[19]

Thus, the total deflection of the flexure in the x-direction will be:

$$\zeta_x = \frac{3FL_x^3}{3EI} = \frac{12FL_x^3}{Etw^3}$$

39

Where w is the width of the flexure and t is the thickness. Therefore, the spring constant of the triple-folded flexure is:

$$k_x = \frac{Etw^3}{12L_x^3} \tag{3.3}$$

Similarly, the double folded flexure spring constants in the y-direction are:

$$k_{y1} = \frac{Etw^3}{8L_{y1}^3} \, , k_{y2} = \frac{Etw^3}{8L_{y1}^3} \tag{3.4}$$

Where L_{y1} and L_{y2} are the length of the double folded flexures. The chevron actuator also acts as a spring and is calculated using the following formula[19]:

$$k_{chev} = M \left[\frac{16Etw^3}{L_c^3} \right] \tag{3.5}$$

The three folded flexures also act as springs in the out-of-plane direction. However, the folded sections also act as independent cantilevers, therefore the spring constants can be calculated similarly below.

$$\zeta_{3-fold} = \frac{3FL_x^3}{3E(\frac{wt^3}{12})} + \frac{4FL_t^3}{3E(\frac{wt^3}{12})} = F\left(\frac{12L_x^3 + 16L_t^3}{Ewt^3} \right)$$

$$k_{3-fold} = \frac{Ewt^3}{12L_x^3 + 16L_t^3} \tag{3.6}$$

The stiffness of the decoupling frame is predicted to be significant as well. The deflection caused by the decoupling frame can be evaluated by assuming that the combined stiffness of the double-folded flexures and chevron actuator that are attached to the decoupling frame are negligible in comparison. The thin section of the decoupling frame that is connected to the triple-folded flexures that support the proof mass can then be assumed to have fixed ends. A force, F, caused by the proof mass acts on the decoupling frame of length L through the triple-folded flexures, which acts a distance, d, from the fixed ends as shown in the figure below.
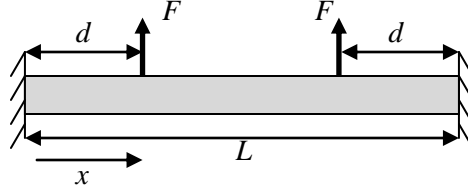
Figure 3-6 - Decoupling frame simplified model.

Equation 3.1 can be used again to model the above diagram with the following boundary conditions:

$$\frac{d}{dx}\zeta\left(\frac{L}{2}\right) = 0 \,, z(0) = 0$$

The formula of the moment is:

$$M = -F\langle x \rangle + F\langle x - d \rangle + F\langle x - (L - d) \rangle$$

Solving for the displacement at distance d from the fixed ends yields:

$$\zeta(d)_{frame} = F\left(\frac{-d^3 - \frac{dL^2}{8} + \frac{(L-d)^3}{6}}{EI}\right) = F\left(\frac{-12d^3 - \frac{3dL^2}{2} + 2(L-d)^3}{Ewt^3}\right)$$

This results in a spring constant for the decoupling frame of:

$$k_{frame} = \frac{Ewt^3}{-12d^3 - \frac{3dL^2}{2} + 2(L-d)^3} \tag{3.7}$$

The forces acting on the decoupling frame for the φ mode shape are similar to figure 3-6 except the forces are acting in opposing directions as shown below:
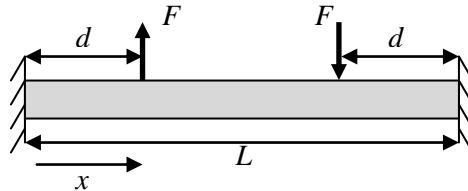
Figure 3-7 - Decoupling frame forces in φ mode shape.

41

Which then gives the spring constant for the decoupling frame about the i-axis:

$$k_{\varphi-frame} = \frac{Ewt^3}{\dfrac{-2d^3L - 4d^4 - 12d^2L^2 + 18dL^3 + 4L^4}{L}} \tag{3.8}$$

The independent springs are then summed in parallel to give the equivalent stiffness in the x, y, and z directions defined as k_i, k_j and k_k respectively. Numerical solutions are given below:

$$k_i = 4k_x = 4\left(\frac{Etw^3}{12L_x^3}\right) = 4\left(\frac{(219GPa)(20\mu m)(13\mu m)^3}{12(260\mu m)^3}\right) = 182.50 N/m$$

$$k_j = 4k_{y1} + 4k_{y2} + 6k_{chev} = 4\left(\frac{Etw^3}{8L_{y1}^3}\right) + 4\left(\frac{Etw^3}{8L_{y2}^3}\right) + 6\left(\frac{16Etw^3}{L_c^3}\right)$$

$$= \left(\frac{(219GPa)(20\mu m)(8\mu m)^3}{2(362\mu m)^3}\right) + \left(\frac{(219GPa)(20\mu m)(8\mu m)^3}{2(420\mu m)^3}\right)$$

$$+ 6\left(\frac{16(219GPa)(20\mu m)(8\mu m)^3}{(860\mu m)^3}\right) = 377.24 N/m$$

$$k_k = \left[\frac{1}{4k_{3-fold}} + \frac{1}{2k_{frame}}\right]^{-1} = \left[\frac{1}{4\left(\dfrac{Ewt^3}{12L_x^3 + 16L_t^3}\right)} + \frac{1}{2\left(\dfrac{Ewt^3}{-12d^3 - \dfrac{3dL^2}{2} + 2(L-d)^3}\right)}\right]^{-1}$$

$$= \left[\frac{1}{4\left(\dfrac{(219GPa)(13\mu m)(20\mu m)^3}{12(260\mu m)^3 + 16(20\mu m)^3}\right)}\right.$$

$$\left. + \frac{1}{2\left(\dfrac{(219GPa)(20\mu m)(20\mu m)^3}{-12(400\mu m)^3 - \dfrac{3(400\mu m)(1400\mu m)^2}{2} + 2(1400\mu m - 400\mu m)^3}\right)}\right]^{-1}$$

$$= 107.64 N/m$$

The spring constant for the φ mode, $k_k{'}$, is:

$$k_k' = \cfrac{1}{\cfrac{1}{4k_{3-fold}} + \cfrac{1}{2k_{\varphi-frame}}} = 233.46N/m$$

3.1.3 Analytical Resonant Frequencies Calculation

The Lagrangian equations of motion were developed for the system given the degrees of freedom: x, y, z, θ, φ. The equations for the potential and kinetic energy of the system are shown below.

$$U = \frac{1}{2}k_i x^2 + \frac{1}{2}k_j y^2 + \frac{1}{2}k_k(z^2 + d_i^2 \sin^2\theta + d_j^2 \sin^2\varphi) - mgz \qquad (3.8)$$

$$T = \frac{1}{2}m(\dot{x}^2 + \dot{y}^2 + \dot{z}^2) + \frac{1}{2}M\dot{y}^2 + \frac{1}{2}I_j\dot{\theta}^2 + \frac{1}{2}I_i\dot{\varphi}^2 \qquad (3.9)$$

Where x, y and z are the displacements of the proof mass and decoupling frame, g is the gravitational acceleration and I_j and I_i are the mass moments of inertia of the proof mass. The mass and mass moments of inertia are given below.

$$m = 1.9224 \times 10^{-7} kg$$

$$M = 1.8012 \times 10^{-7} kg$$

$$I = \frac{1}{12}m(b^2 + h^2)$$

$$I_i = \frac{1}{12}(1.9224 \times 10^{-7} kg)(600\mu m^2 + 20\mu m^2) = 5.77 \times 10^{-15} kg \cdot m^2$$

$$I_j = \frac{1}{12}(1.9224 \times 10^{-7} kg)(1800\mu m^2 + 20\mu m^2) = 5.19 \times 10^{-14} kg \cdot m^2$$

Assuming small deflections about its neutral position, the above equations are simplified to:

$$x: m\ddot{x} + k_i x = 0$$

$$y: m\ddot{y} + k_j y = 0$$

$$z: m\ddot{z} + k_k z = 0$$

$$\theta: I_j\ddot{\theta} + d_i^2 k_k \theta = 0$$

$$\varphi: I_i\ddot{\varphi} + d_j^2 k_k'\varphi = 0$$

The below solution is assumed for the system:

43

$$\{x(t)\} = \{X\}e^{\lambda t}$$

The natural frequencies of the system, λ, can be solved in the following matrix.

$$x: m\lambda^2 + k_i = 0$$

$$y: m\lambda^2 + k_j = 0$$

$$z: m\lambda^2 + k_k = 0$$

$$\theta: I_j\lambda^2 + d_i^2 k_k = 0$$

$$\varphi: I_i\lambda^2 + d_j^2 k_k{}' = 0$$

Therefore the natural frequencies of the system are 4.904kHz, 5.066kHz, 3.766kHz, 6.523kHz and 8.644kHz for the *x, y, z, θ, φ* DoF respectively.

3.2 Finite Element Analysis

The COMSOL solid, stress-strain module with the Lagrange-quadratic eigenfrequency solver was used to numerically determine several eigenfrequencies. It was assumed that viscous and frictional damping is negligible and that small vibrations and displacements take place. The pre-packaged MEMS material constants for nickel and SCSi were used, which can be found in the table 1 in the appendix.

All three gyroscopes were designed in MEMS Pro (L-Edit) and then imported into COMSOL. A 3D tetrahedral element, 10 node, size-varying mesh was used in each case.

Each simulation result is depicted as a deformed structure to show the mode shape. Colouring was also used as an indicator for the out-of-plane, z-direction, displacement so that the results can readily be compared to experimental fast Fourier transform (FFT) data, where dark red and dark blue indicate large displacements from the neutral axis and teal indicates negligible displacement.

3.3 Thermally-Actuated Gyroscope Simulation Results

The thermally-actuated gyroscope design was manufactured using the MetalMUMPS process outlined in section 2.2.1. The mechanical structure is made from electrodeposited nickel, which is suspended above the substrate. Nickel electrical pads are also used to anchor the suspended structure to the substrate.

The structure was imported into COMSOL and geometrically simplified to reduce computation time. The holes in the structure, necessary in the MetalMUMPS process to facilitate device release from the substrate, were removed as well as the sensing parallel plate sensors, which caused an acceptable bias error of -1.64% to the mass of the device. A mesh of 62747 elements with 391287 degrees-of-freedom (DoF) was used to define the structure of the device within COMSOL. The first five simulated mode shapes are shown in the figures below.

Figure 3-8 - Thermally-actuated gyroscope simulated 1st mode at 3.669kHz.
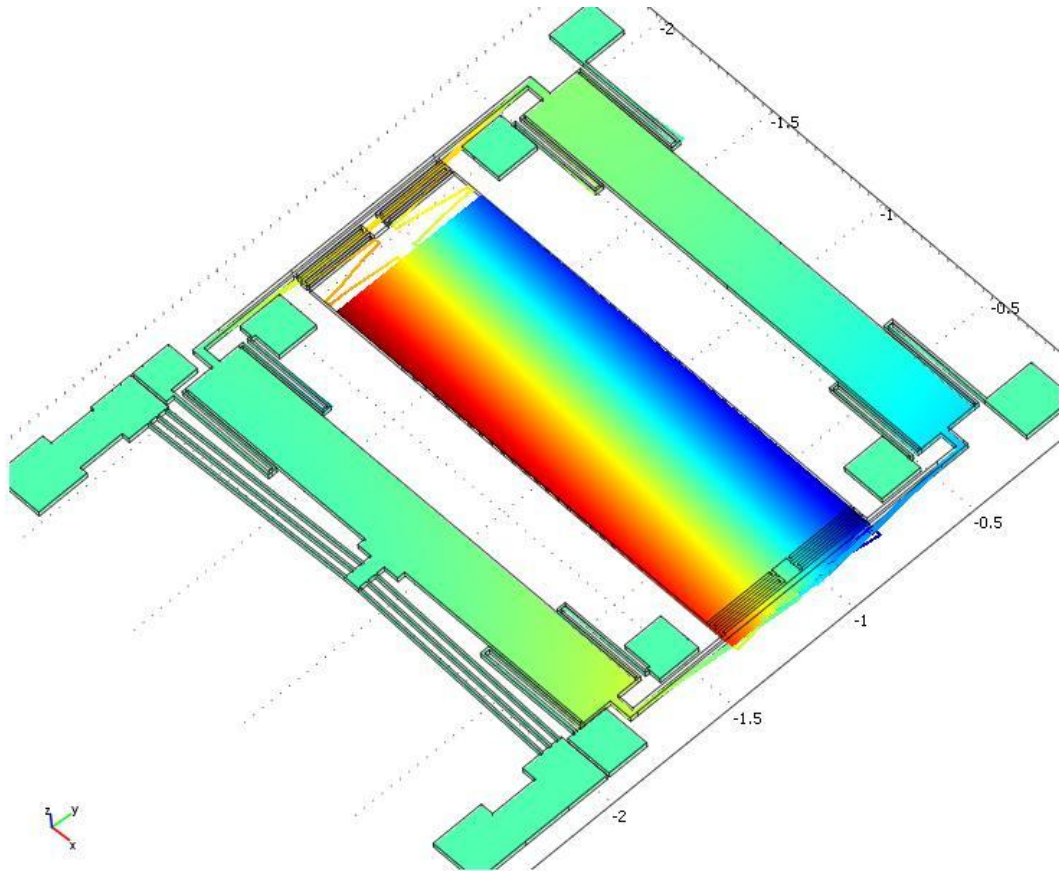
Figure 3-9 - Thermally-actuated gyroscope simulated 2nd mode at 4.948kHz.
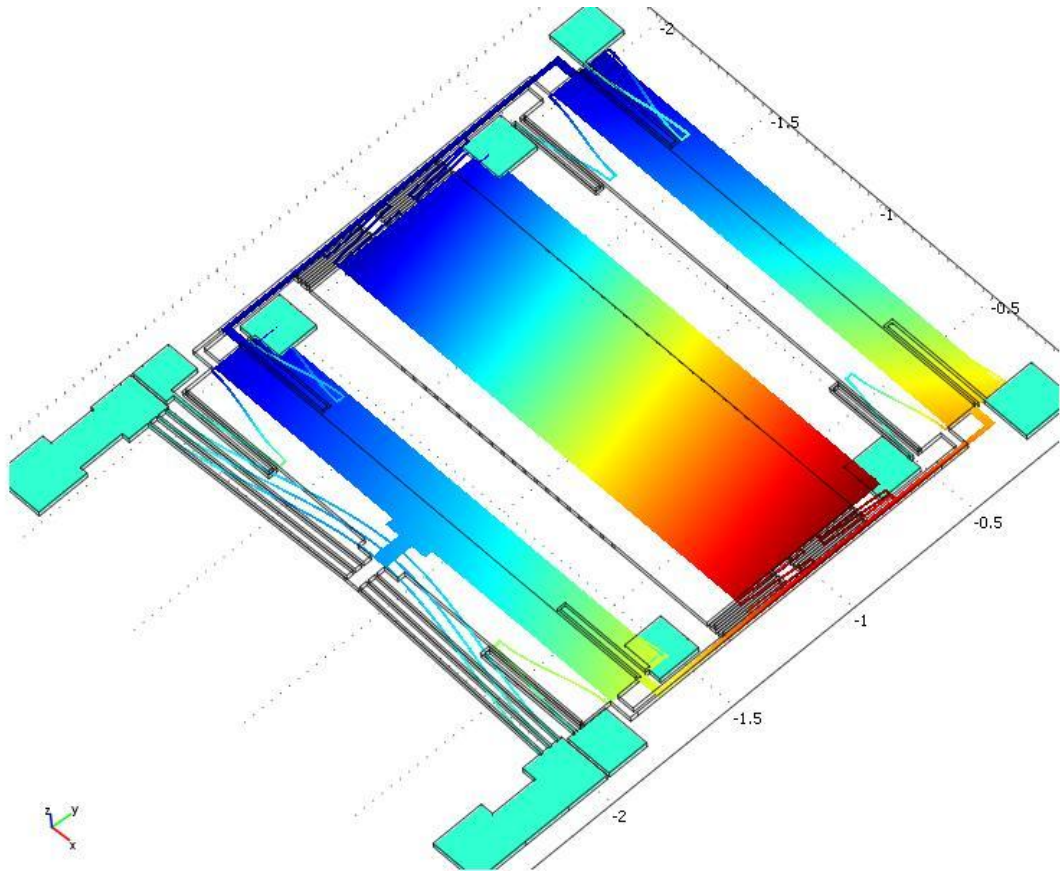
Figure 3-10 - Thermally-actuated gyroscope simulated 3rd mode at 5.459kHz.
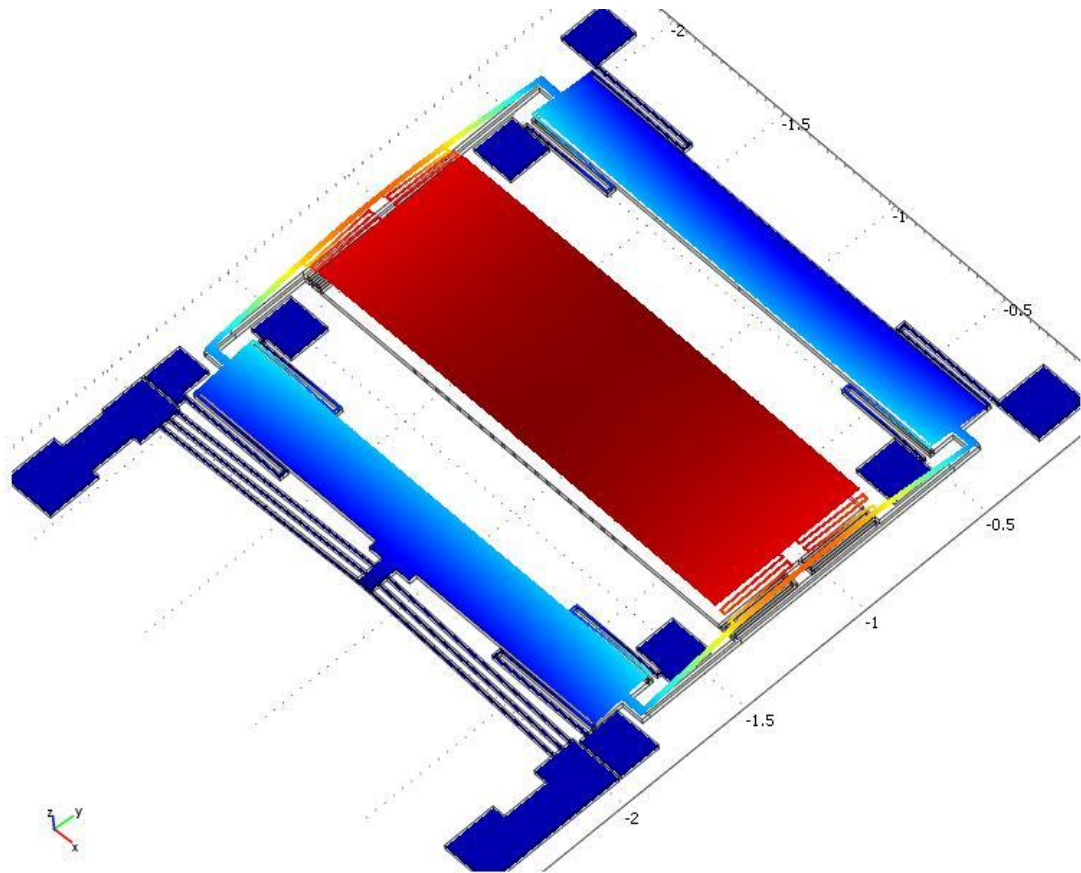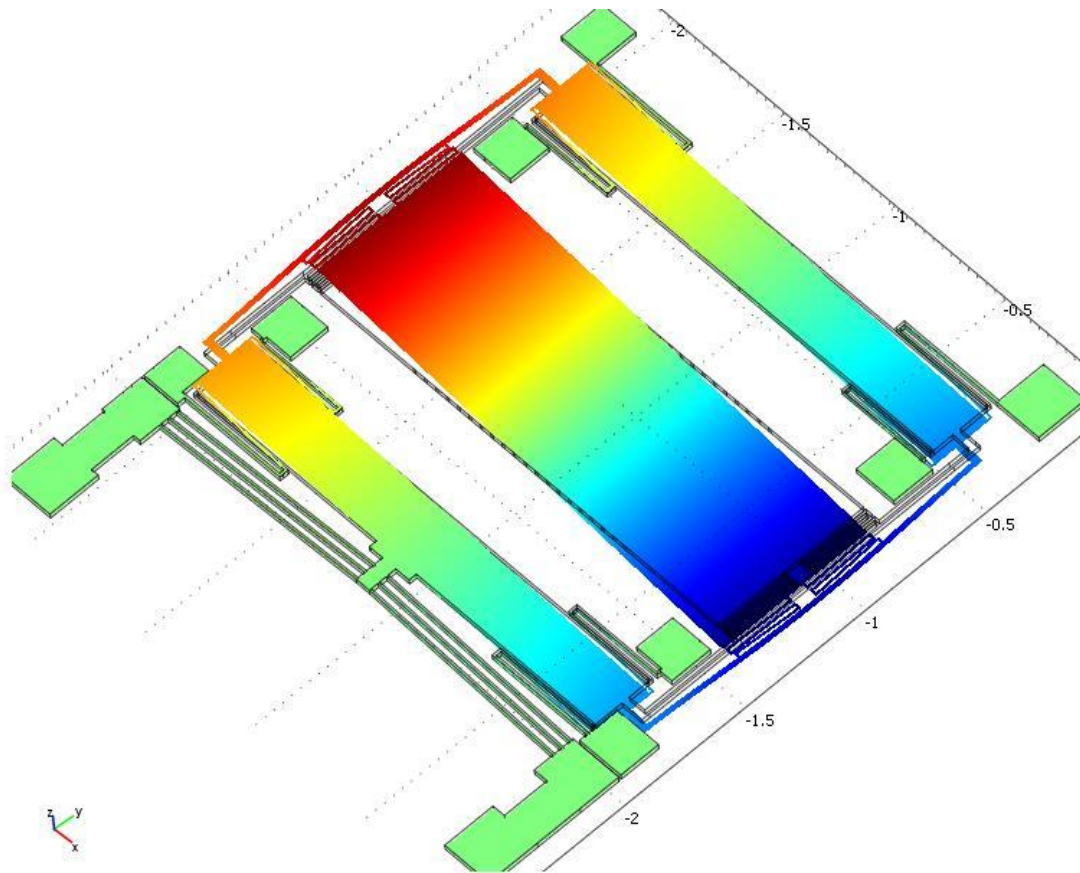
Figure 3-11 - Thermally-actuated gyroscope simulated 4th mode at 6.923kHz.
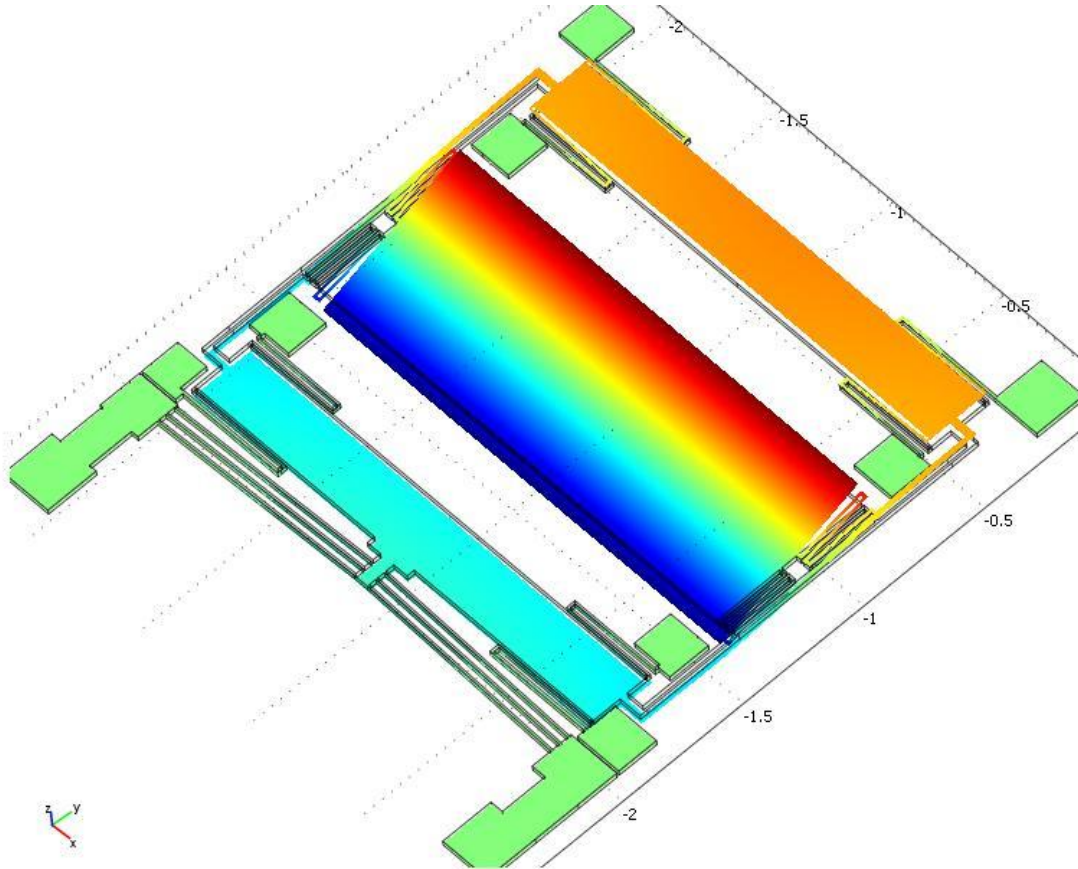
Figure 3-12 - Thermally-actuated gyroscope simulated 5th mode at 8.500kHz.

The scale of the z-displacement in each simulation is arbitrary but useful in comparing the relative magnitudes associated with each eigenfrequency. However, the frequency of the mode shape is important in predicting the resonant frequencies of the device prototype.

The simulated results above show five distinct mode shapes of the thermally-actuated gyroscope. The first mode shape, which occurs at 3.669kHz, shows the centre proof mass vibrating straight up-and-down in the z-direction. The second mode shape causes the proof mass to move in the x-direction, where there is also a slight torsion mode about the x-axis. This response occurs at 4.948kHz and is defined as the sensing mode of the device. The third mode occurs at 5.459kHz where the proof mass moves along the y-direction, also defined as the driving mode. There is a torsional mode at 6.293kHz where the proof mass vibrates about the y-axis and likewise, at

Figure 3-12 - Thermally-actuated gyroscope simulated 5th mode at 8.500kHz.

8.500kHz the proof mass vibrates about the x-axis. These mode shapes correspond to the analytically determined mode shapes where the first, second, third, fourth and fifth modes are the z, x, y, θ and φ modes in the analytical model. This information is summarized in the table below:

Table 3-1 - Thermally driven microgyroscopic sensor analytical and simulated summary of results.

Mode Shape	DoF	Analytical Eigenfrequency (kHz)	Simulated Result (kHz)	% Error
1st	z	3.766	3.669	2.6%
2nd	x	4.904	4.948	-0.9%
3rd	y	5.066	5.459	-7.2%
4th	ϑ	6.523	6.923	-5.8%
5th	φ	8.644	8.500	1.7%

The difference between the simulated and analytical values can be explained by the initial rigidity and fixed end assumptions made for the analytical model.

3.4 Electrostatically-Actuated MetalMUMPS Gyroscope Simulation Results

The electrostatically-actuated MetalMUMPS gyroscope was modelled similarly to the thermally-actuated gyroscope. The CAD model was not simplified in this case; therefore a finer mesh of 273378 elements with 1547550 DoF was required to define the increased complexity of the gyroscopes geometry while sacrificing computation time. The structure itself is more complex in comparison to the thermal gyroscope since it contains an additional frame, which increases the degrees-of-freedom. Several of the significant mode shapes are shown below.

Figure 3-13 - Electrostatically-actuated MetalMUMPS gyroscope simulated 1st mode at 1.170kHz.

Figure 3-14 - Electrostatically-actuated MetalMUMPS gyroscope simulated 2nd mode at 1.644kHz.

Figure 3-15 - Electrostatically-actuated MetalMUMPS gyroscope simulated 3rd mode at 1.941kHz.
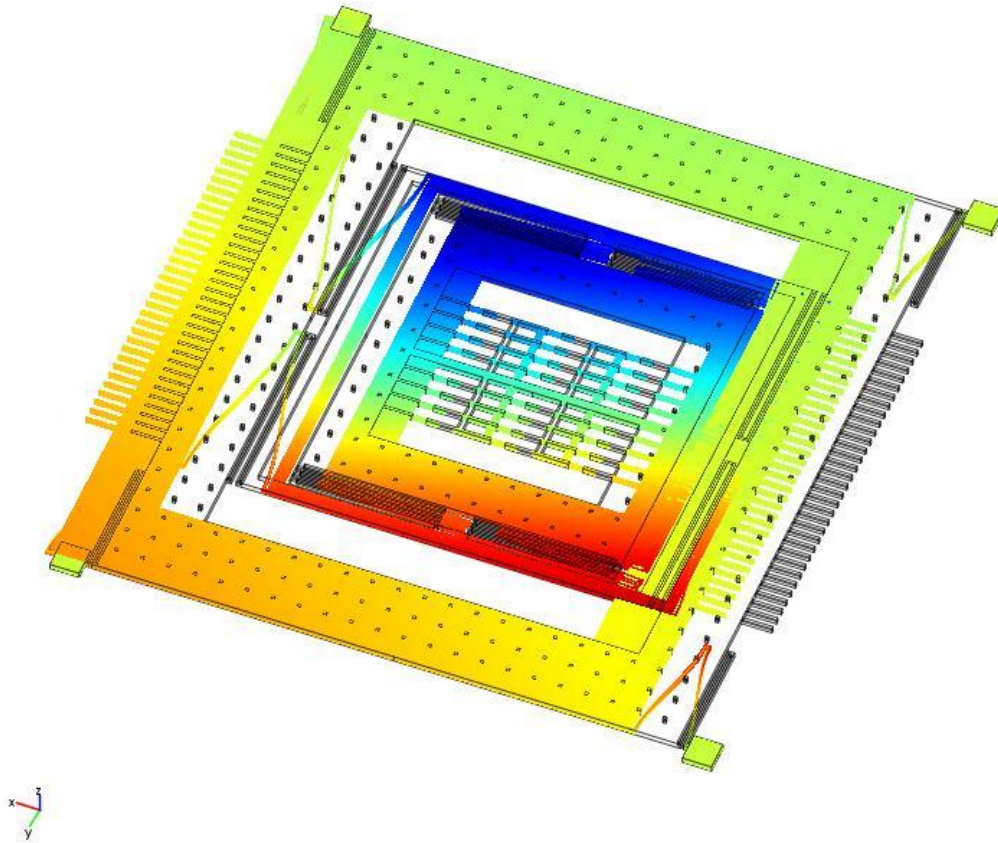
Figure 3-16 - Electrostatically-actuated MetalMUMPS gyroscope simulated 4th mode at 2.316kHz.
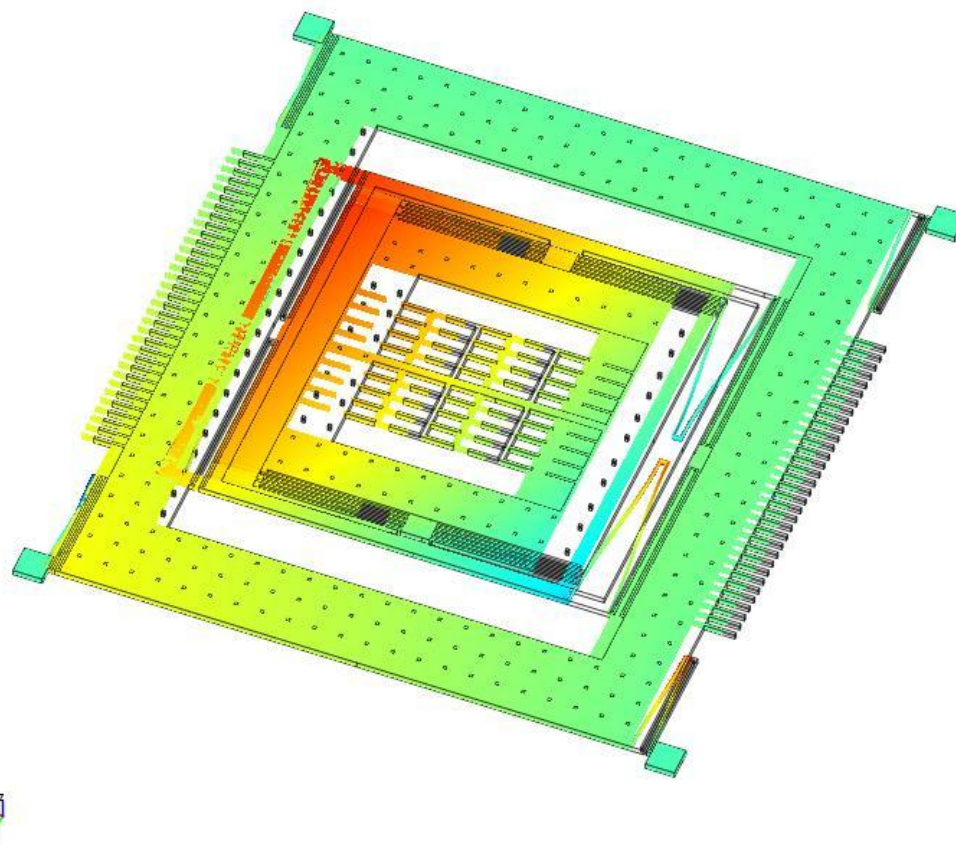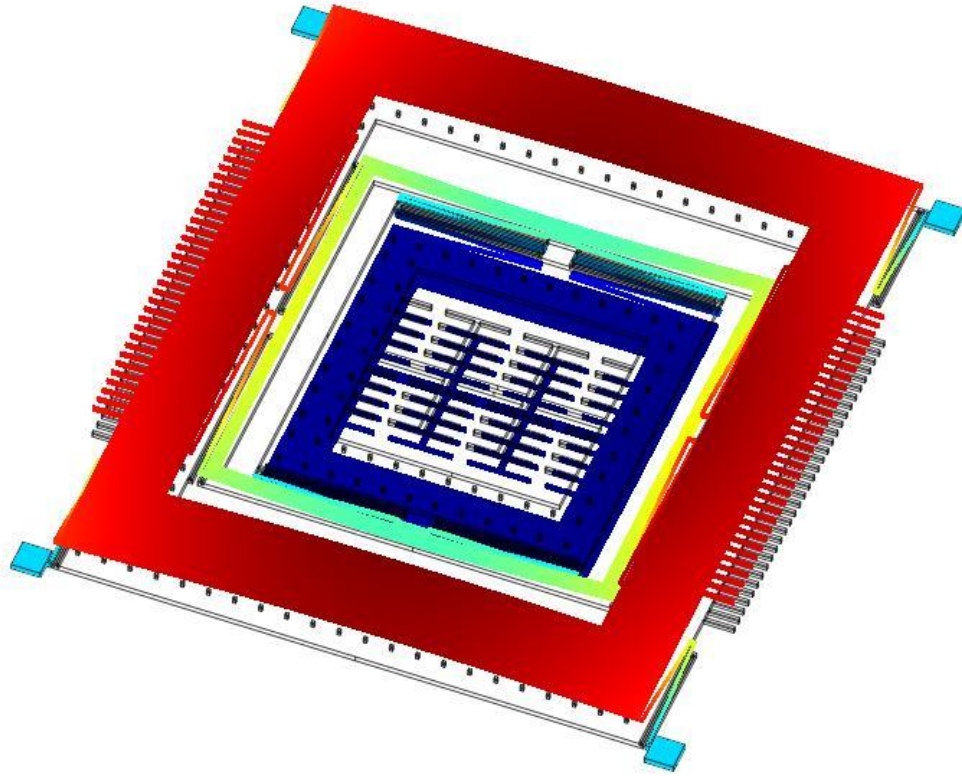
Figure 3-17 - Electrostatically-actuated MetalMUMPS gyroscope simulated 7th mode at 4.246kHz.
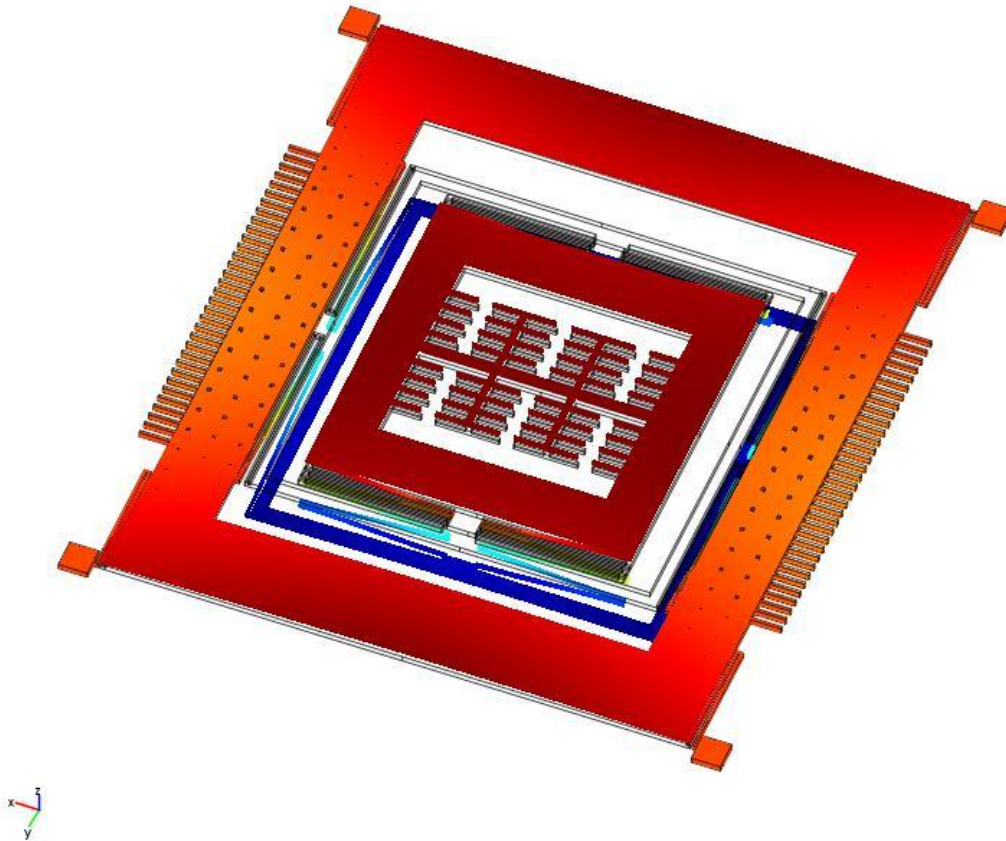
Figure 3-18 - Electrostatically-actuated MetalMUMPS gyroscope simulated 11th mode at 8.510kHz.

The first, second and fourth mode shapes are in-plane modes, which occur at 1.170kHz, 1.644kHz and 2.316kHz. The first mode is in the driving, x-direction, which only affects the middle frame. The second mode is in the sensing, y-direction, which exclusively affects the proof mass since it is the only mass that has a DOF in that direction. The fourth mode also vibrates in the driving direction but the middle and outside frames vibrate out of phase with each other.

The out-of-plane mode shapes that are shown are the third, seventh and eleventh modes, which occur at 1.941kHz, 4.246kHz and 8.510kHz. These were selected because they were observed in the experimental data. The third mode shows the proof mass and middle frame moving in-phase with each other while the outside frame remains stationary. Both the outside frame and proof

mass move out-of-phase with each other in the seventh mode shape. The middle frame bends in response to the outside frame's displacement but is motionless otherwise. The eleventh mode shape involves the proof mass and outside frame moving out-of-phase with the middle frame.

3.5 Electrostatically-Actuated SOI Gyroscope Simulation Results

The structure of the electrostatically-actuated SOI gyroscope is made of single-crystal silicon as opposed to nickel like the MetalMUMPS devices. The thin-film silicon layer is half the thickness of the MetalMUMPS layer as well at 10μm, which affects the spring and mass constants of the mechanical components of the system. The device itself is relatively simple in comparison with only an outside frame and a proof mass with supporting flexures to suspend the structure. A mesh of 101061 elements with 585126 DoF was used in the simulated model. The first seven mode shapes that were derived from the simulated model are shown in the figures below.

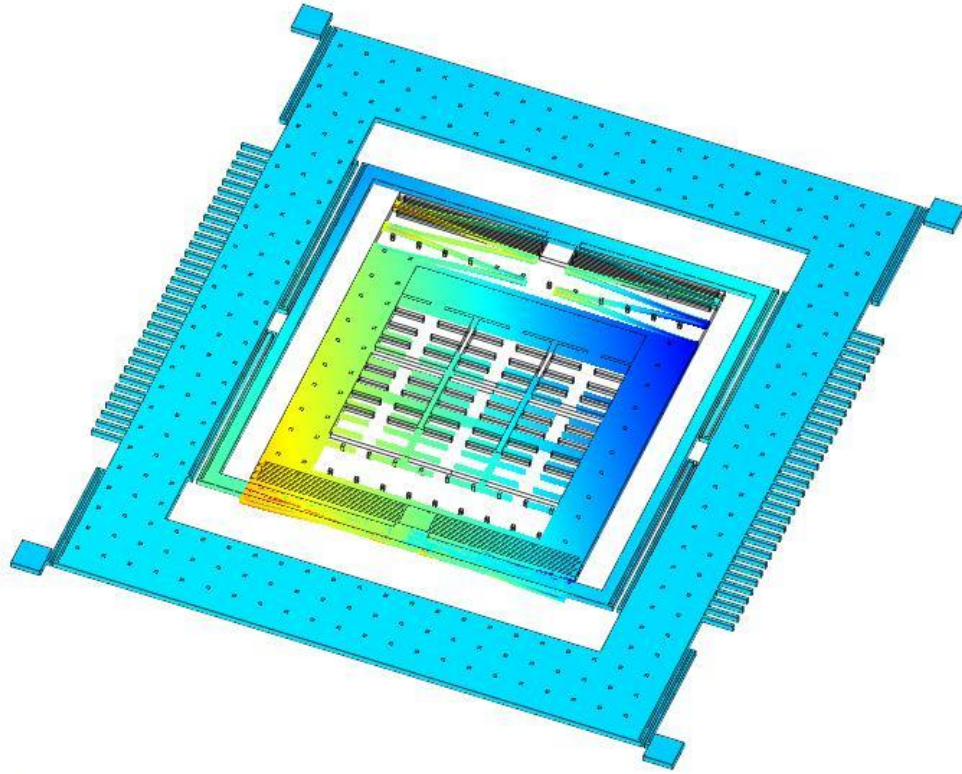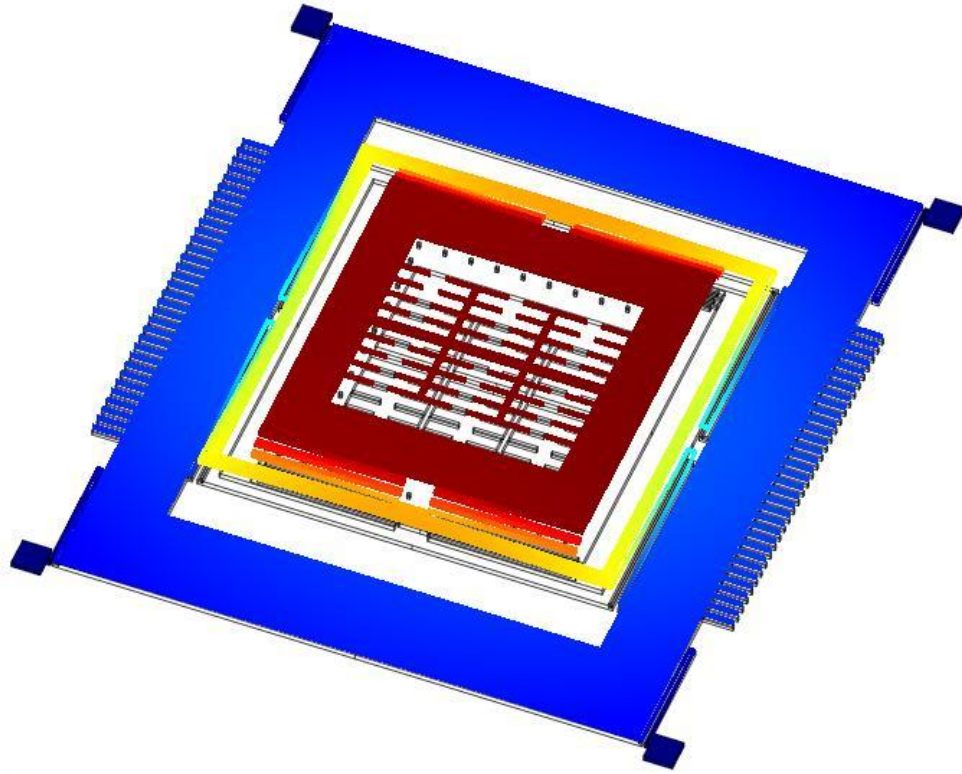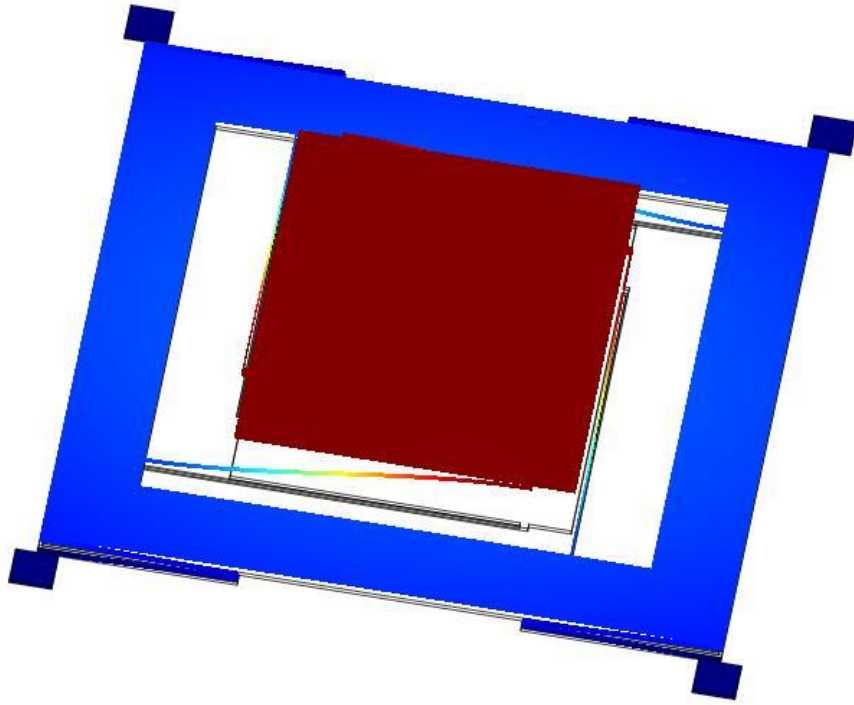**Figure 3-19 - Electrostatically-actuated SOI gyroscope simulated 1st mode at 2.159kHz.**
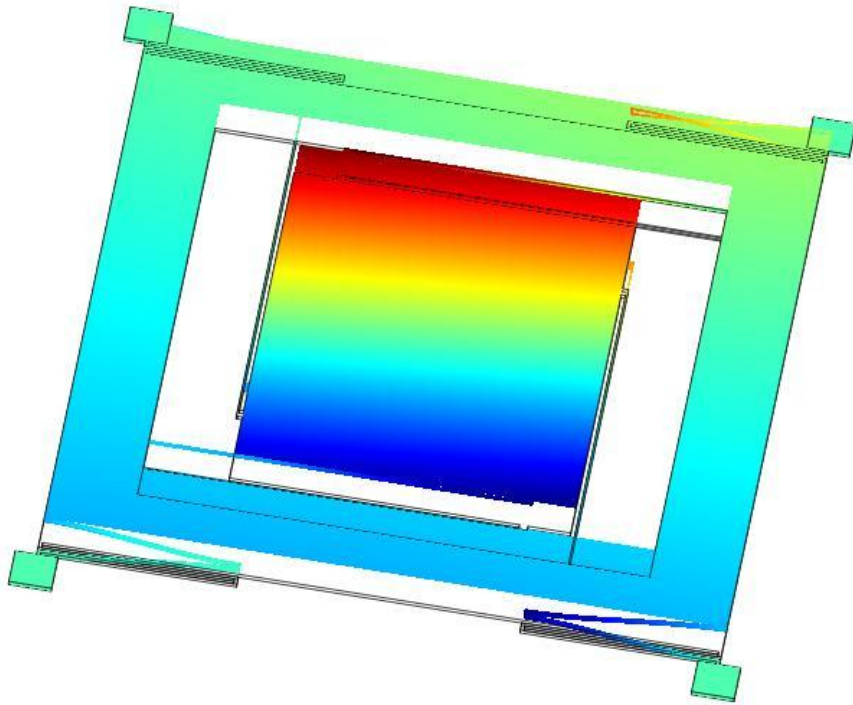
Figure 3-20 - Electrostatically-actuated SOI gyroscope simulated 2nd mode at 3.298kHz.
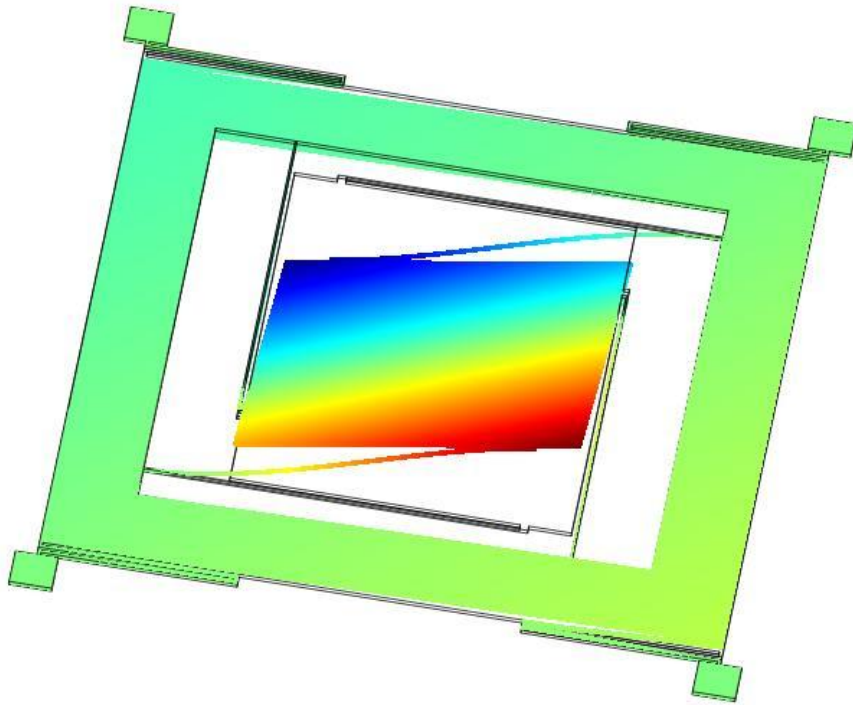
Figure 3-21 - Electrostatically-actuated SOI gyroscope simulated 3rd mode at 3.454kHz.
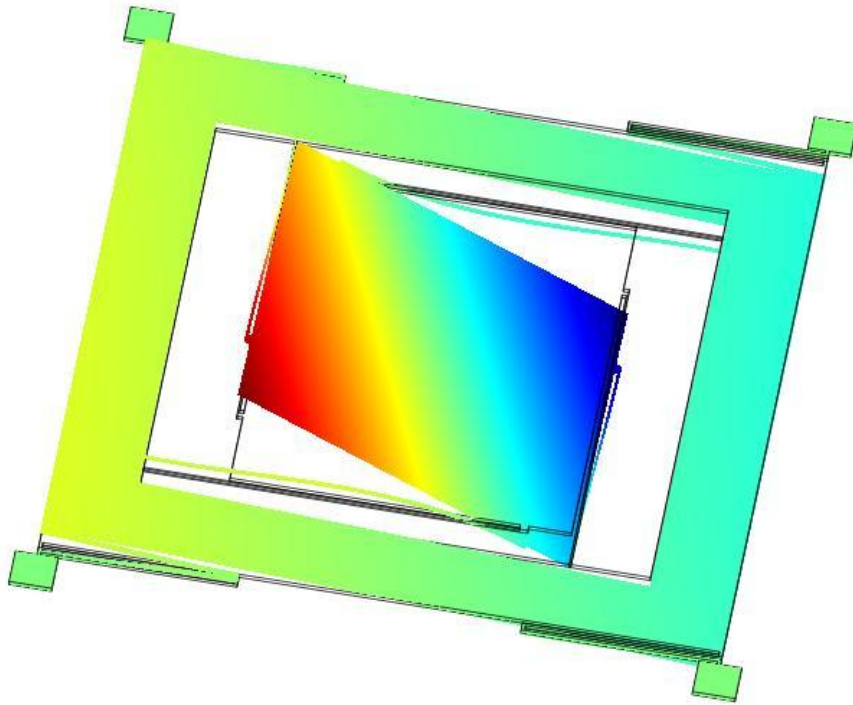
Figure 3-22 - Electrostatically-actuated SOI gyroscope simulated 4th mode at 3.679kHz.
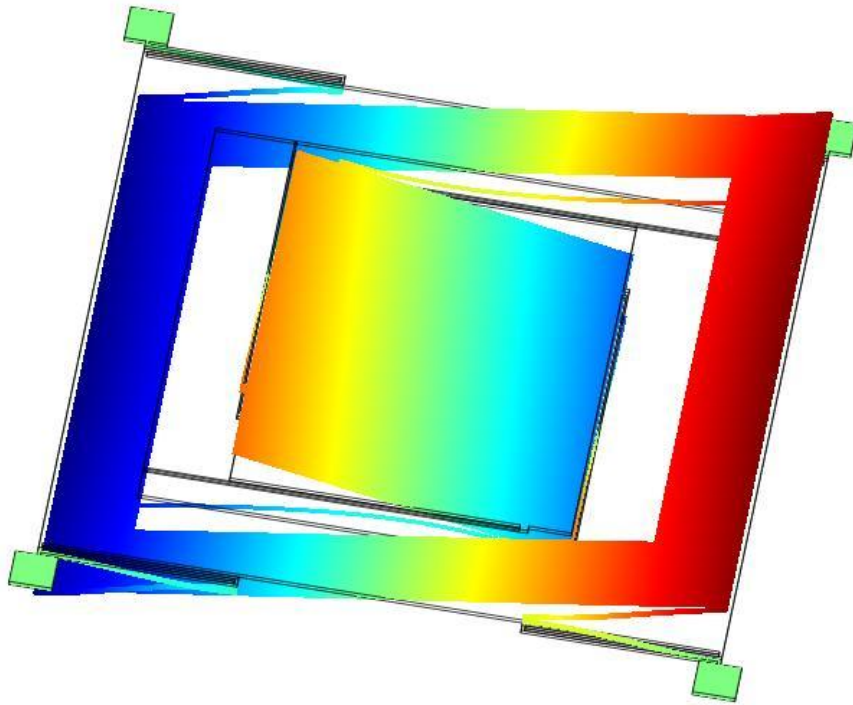
Figure 3-23 - Electrostatically-actuated SOI gyroscope simulated 5th mode at 5.494kHz.
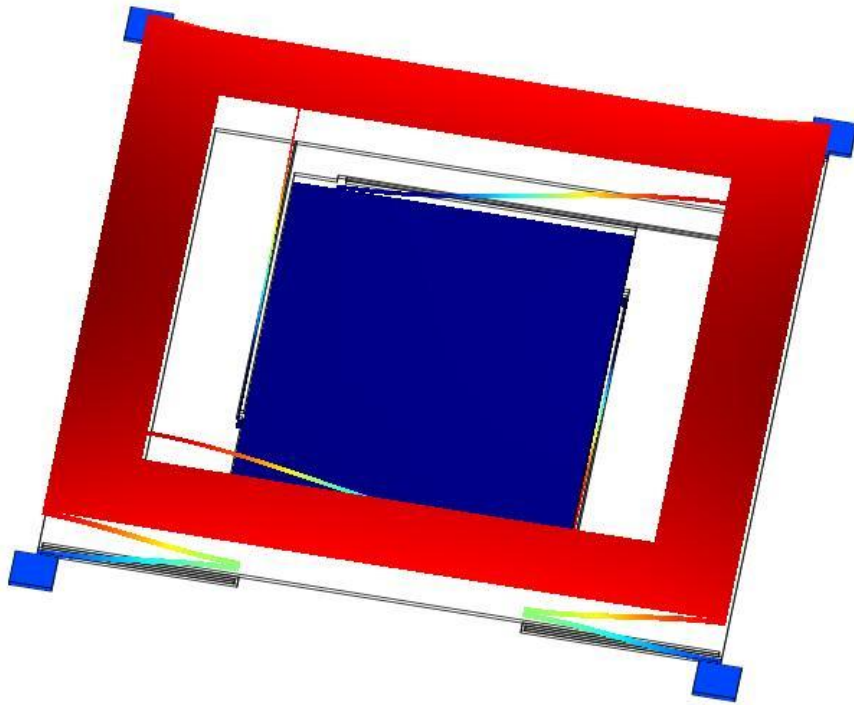
Figure 3-24 - Electrostatically-actuated SOI gyroscope simulated 6th mode at 5.500kHz.
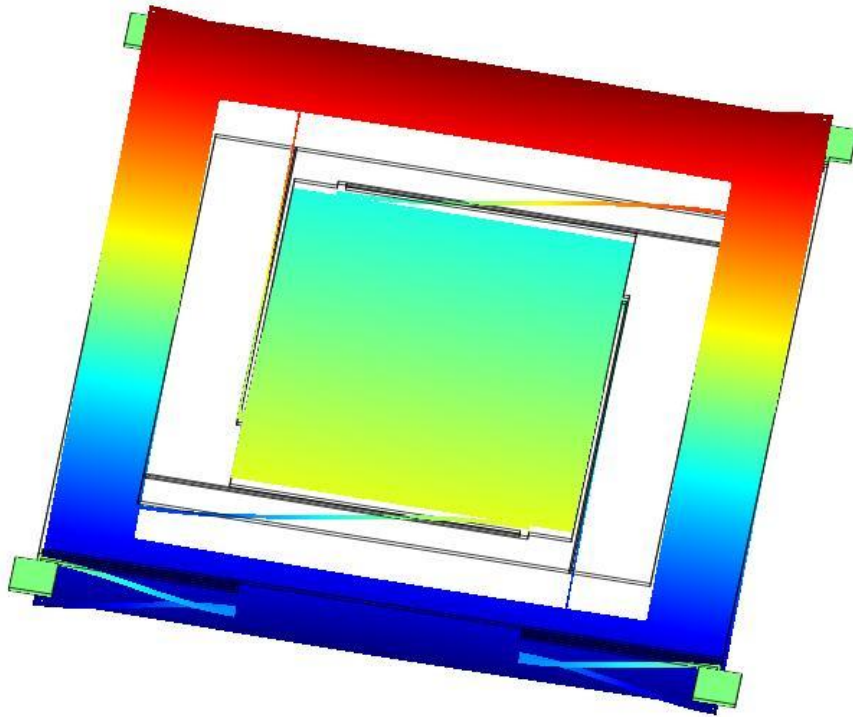
Figure 3-25 - Electrostatically-actuated SOI gyroscope simulated 7th mode at 7.476kHz.

The first and second modes are defined as the driving and sensing modes respectfully. At 2.159kHz the driving mode operates exclusively on the proof mass in the z-direction. The sensing mode shape acts in the y-direction on the outside frame and occurs at 3.298kHz. At 3.454kHz and 3.679kHz there is a torsional mode where the proof mass is rotating about a nodal axis located 45° and 135° in the x-y plane respectively. The fifth mode shape figure shows a torional mode where the outside frame vibrates about the y-axis at 5.494kHz and the proof mass bending in response to the applied forces from the connecting flexures. The outside frame vibrates up-and-down in the z-direction at the mode shape that occurs at 5.500kHz. The seventh mode shape figure shows the outside frame vibrating about the x-axis at 7.476kHz.

Chapter 4

Experimental Determination of Modal Frequencies

The purpose of experimentally determining the modal frequencies of the gyroscopes is to verify the simulated models and to predict their operational performance.

4.1 Thermally-Actuated Gyroscope Experimental Testing

4.1.1 Thermally-Actuated Gyroscope Testing Methodology

All testing was conducted in the MEMS Lab in Jackson Hall Rm. 212, Queen's University. Static measurements were performed using the National Instruments Vision Assistant AutoMax software. Individual images of the actuator were taken at different currents supplied by an Agilent DC source. The displacement of the actuator was measured in pixels by the image processing software by comparing each image to a reference image where no current applied. The resultant data was converted to microns and plotted.

Dynamic measurements were made with the Polytech Microsystem Analyzer MSA-400. The onboard signal generator was used to supply the actuation signal. The signal was amplified using an FK602 2-Watt power amplifier, which was powered by an Agilent DC source. The original and amplified signals were displayed using a Tektronix TDS 3052 Digital Oscilloscope and the electrical current was measured using a Mastercraft Digital Multimeter. Using laser interferometry, a scanning laser measured the out-of-plane motions of the gyroscope and relayed the information to the Polytec OFV-5000 vibrometer controller. The original actuation signal is compared to the vibrometer measurements. A diagram showing the relationships between the apparatuses is shown in the diagram in Figure 4.1. The experimental setup for the dynamic testing is demonstrated in Figrue 4.2.
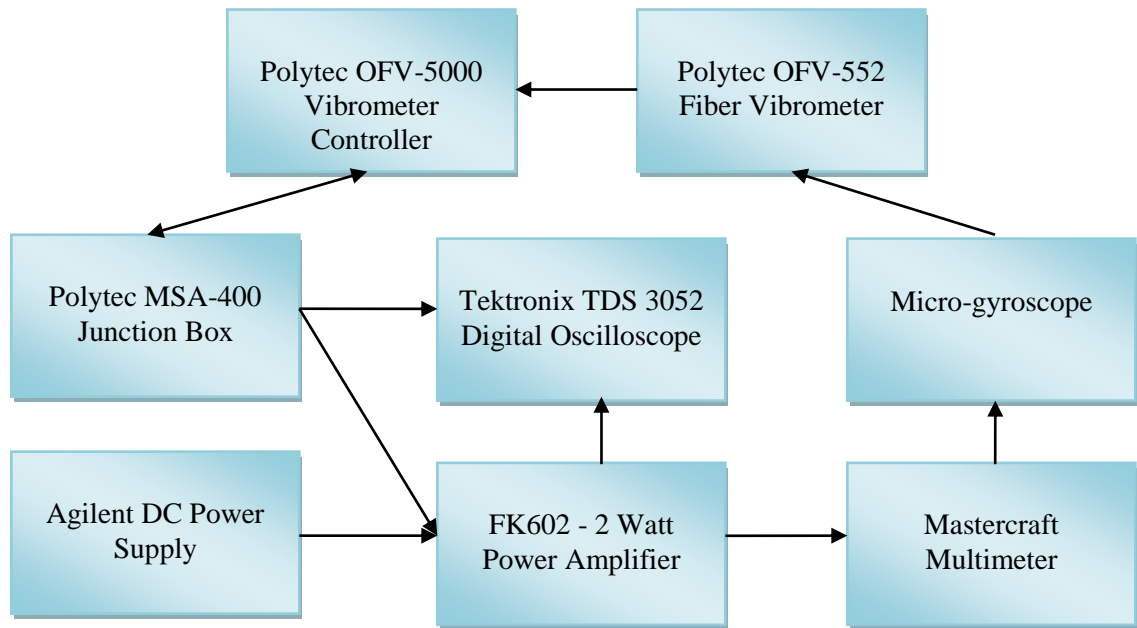
Figure 4-1 - Diagram of the electrical relationships between testing equipment apparatuses used for the thermally-actuated gyroscope.
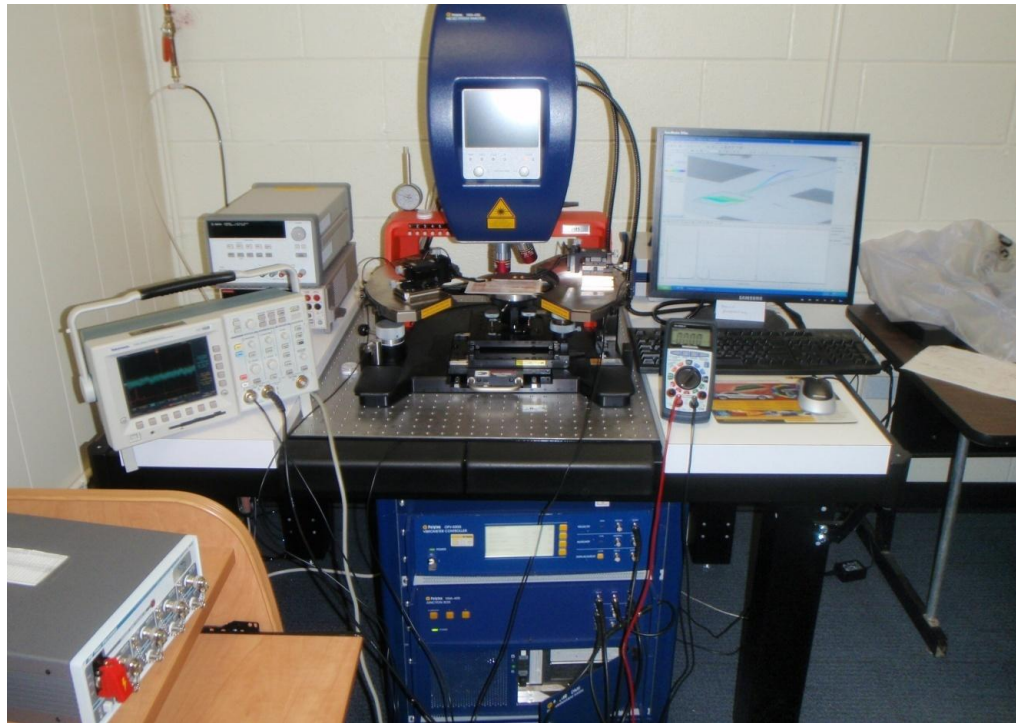
Figure 4-2 - Polytec MSA-400 and testing setup.

The Polytec MSA-400 can dynamically characterize in-plane modes using the Planar Motion Analyser (PMA-400) and out-of-plane modes using the Scanning Vibrometer (PSV-400). The

PMA uses stroboscopic images to measure the displacement of MEMS devices. An image is captured at different phase angles within an excitation signal waveform and spliced together to form a video. The displacement of the component being measured is determined by image processing. Each image is compared to the original reference image and the distance between the components of interest is measured in pixels between the two images. This is a similar process to the one used for static testing. An example of a reference image is shown in figure 4-3 below. The green box indicates the searching area and the red box is the area-of-interest.
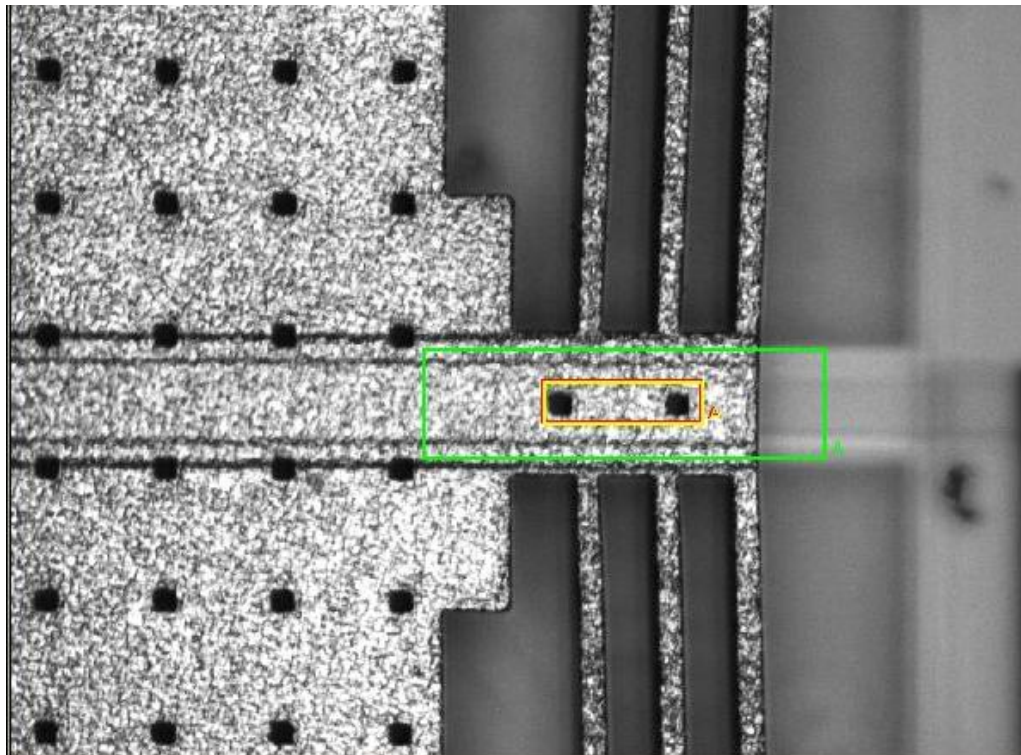
Figure 4-3 - Polytec PMA reference image example.

The PSV uses laser interferometry to determine the velocity of the out-of-plane component of MEMS devices. A measurement laser is scattered on the surface of a vibrating device that is then reflected back to the scanning head where the measurement laser interferes with a second

reference laser. The phase shift is measured using a photosensor and digitized so an FFT can be produced from the recorded data. A visual diagram of this process can be seen in Figure 4-4.
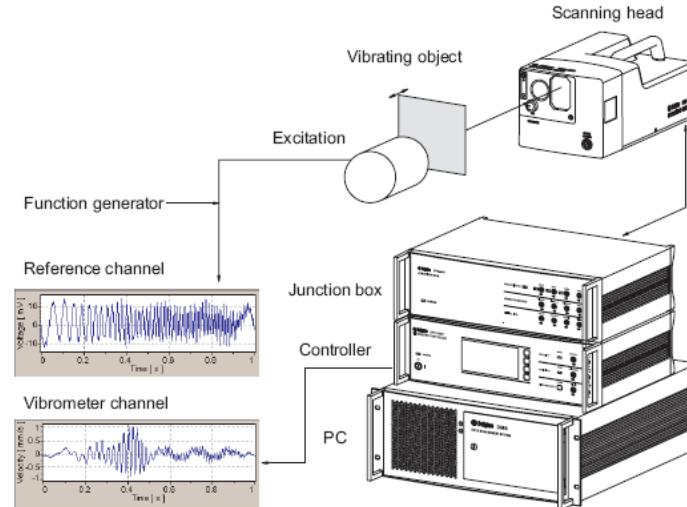
Figure 4-4 - Laser interferometry equipment diagram[20].

The testing equipment was isolated from environmental vibration noise using a pneumatically damped table. All measurements were taken at atmospheric pressure and room temperature.

4.1.2 Thermally-Actuated Gyroscope Prototype

The electro-thermally driven micro-gyroscope was fabricated using the MetalMUMPS process, which is outlined in section 2.2.1. Figure 4-5 below shows a scanning electron microscope (SEM) image of the gyroscope with the significant features identified. Figure 3-1 in the previous chapter shows the boundary conditions of the device.
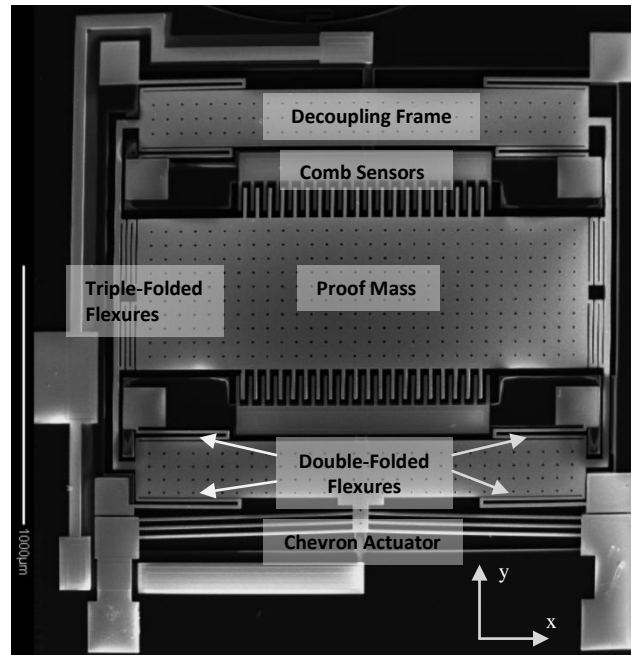
Figure 4-5 - SEM image of an electro-thermally actuated MEMS gyroscope prototype.

When the decoupling frame is driven using the chevron actuator and an angular velocity is applied about the out-of-plane, z-direction then a Coriolis acceleration is applied to the proof mass in the x-direction, which is then detected by the electrostatic comb sensors.

4.1.3 Thermally-Actuated Gyroscope Static Measurements

The response of the thermal actuator under a static excitation signal was first investigated to predict the actuation current required for dynamic testing and to provide additional insight on the behaviour of the actuator. The displacement was determined using the National Instruments Vision Assistant package. The current was steadily controlled and increased using an Agilent DC power source. The results of the test can be seen in the graph, figure 4-7, below.
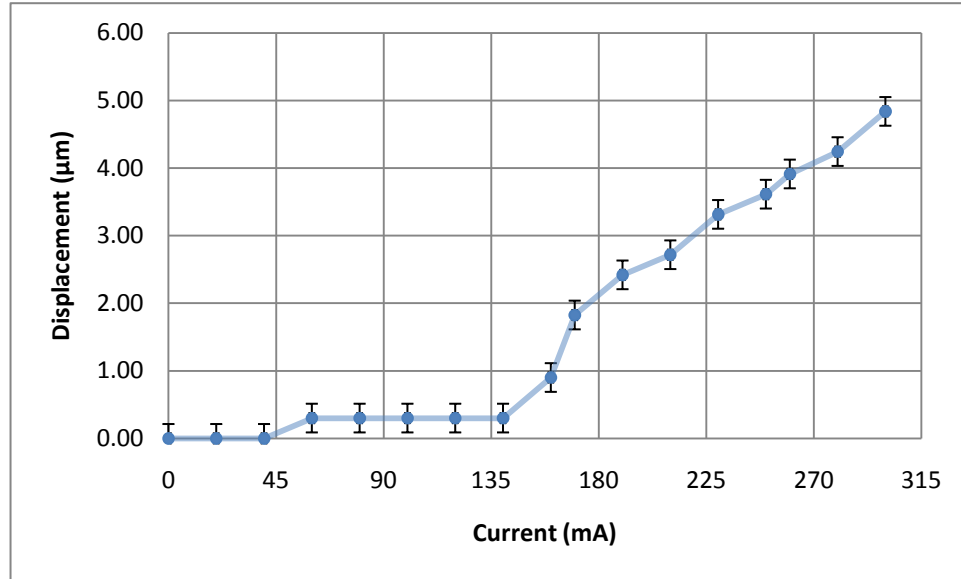
Figure 4-6 - Thermal actuator displacement and current relationship.

The error bars indicate the inaccuracy associated with the resolution of the images, which is limited by the magnification of the lens and number of pixels in each image. A 1 pixel change corresponds to a 0.3μm displacement, so planar displacements below 0.3μm cannot be determined accurately using this method.

The thermal actuator exhibits relatively little displacement under 150mA of current. This is attributed to surface stiction preventing the movement of the gyroscope frame under low thermal expansion forces. Above 150mA the surface stiction is overcome, which leads to a sharp increase in displacement followed by a linear relationship above 180mA. Above 300mA the chevron actuator begins to bow out-of-plane making it difficult to measure the in-plane displacement and becomes non-linear once again. Current between 180mA-300mA is the target operating range for the excitation signal of this device.

4.1.4 Thermally-Actuated Gyroscope Planar Driving Mode Resonant Frequency

Characterization

A sinusoidal AC 225mA$_{RMS}$ excitation signal was applied through the chevron actuator to elicit a resonant response from the structure. The driving mode natural frequency was identified by scanning multiple frequencies and analyzing the displacement and quality of the mechanical vibration. No DC offset was applied to the signal; consequently the frequency of the mechanical response is twice the frequency of the driving signal due to the squaring of the driving current waveform from joule heating. The maximum displacement occurred at a forcing frequency of approximately 3.0kHz with a mechanical response above the noise level between 2.5kHz and 3.5kHz. A comparison of the three frequency responses is shown in figure 4-8 below.
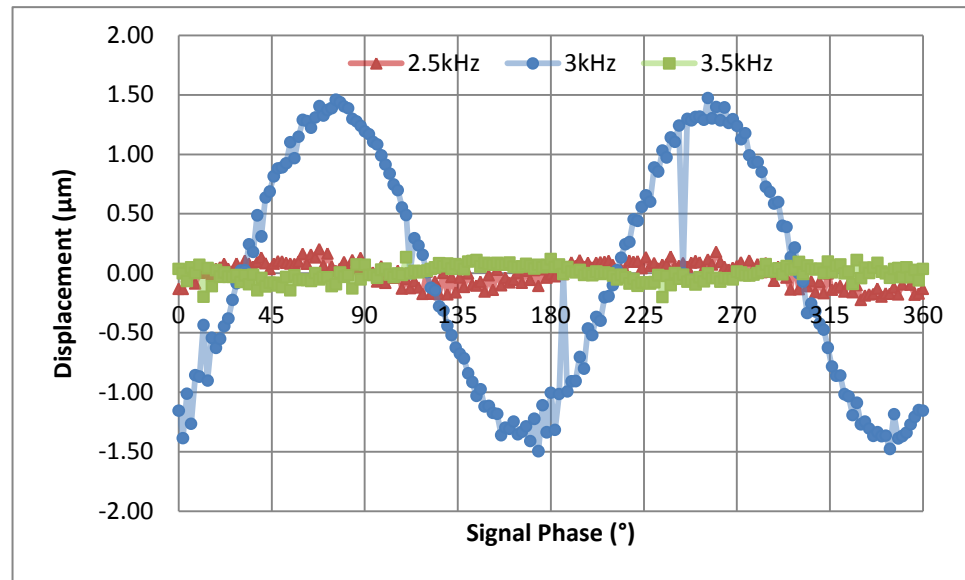
Figure 4-7 - Frequency response using a 225mA$_{RMS}$ sinusoidal excitation signal at three frequencies.

The driving resonant frequency, therefore, occurs at a frequency of 6.0kHz where a peak-to-peak displacement of approximately 3μm is elicited from the structure using a 225mA$_{RMS}$ AC signal. At 5kHz and 7kHz the displacement is significantly less at 0.3μm, however the vibration is still above the noise level and can still be used for exciting the sensing mass if necessary. The driving

mode resonant frequency is the most efficient operating frequency and would cause the greatest response in the sensing mass if the mode shape frequencies coincided.

Once the resonant frequency of the driving mode was identified to be 6.0kHz, the displacement amplitude for changes in current at a constant frequency was investigated. It is assumed that the operating voltage does not influence the resonant frequency of the device; however greater velocities will induce changes in the damping coefficients and higher temperatures will affect the spring coefficients due to changes in Young's modulus. The structure was vibrated at an operating frequency of 6.0kHz for all tests to induce the greatest response above the noise level. Seventeen separate tests were performed for currents between 0mA to 577mA, which is close to the predicted elastic limits of the actuator. The maximum peak-to-peak displacement was recorded with the RMS AC current and resultant power, which is graphed in the figure below. A table of the results can be found in table 2 in the appendix.
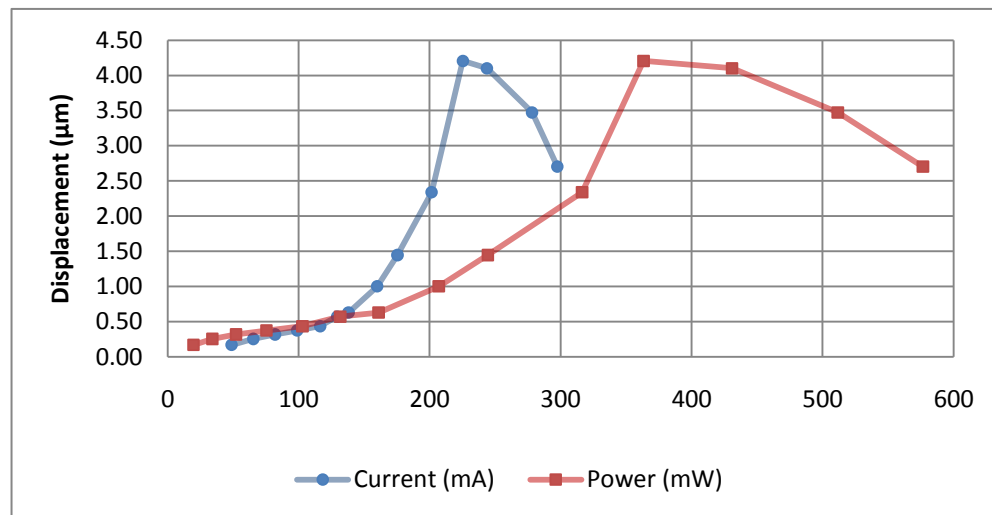
Figure 4-8 - Power consumption of the thermal actuator at several displacements elicited by changes in operational current.

Displacements amplitudes for RMS currents below 20mA were impossible to extract from the data due to noise. The response from the testing was, otherwise, relatively consistent and

predictable. The displacement can be represented with a second-order polynomial, as predicted by the governing equations shown in section 1.3.2, which has an R^2 value of 0.968. However, a third-order polynomial fits the data much better in comparison with an R^2 value of 0.997, suggesting that there are non-linearity's present. Another point-of-interest is the inflection point that occurs at 4.2µm of displacement. This is likely caused by energy being leeched by out-of-plane motions of the system such as bowing of the thermal actuator. The forcing frequency response curves, shown below, provide additional insight on the decrease in displacement from greater power consumption.
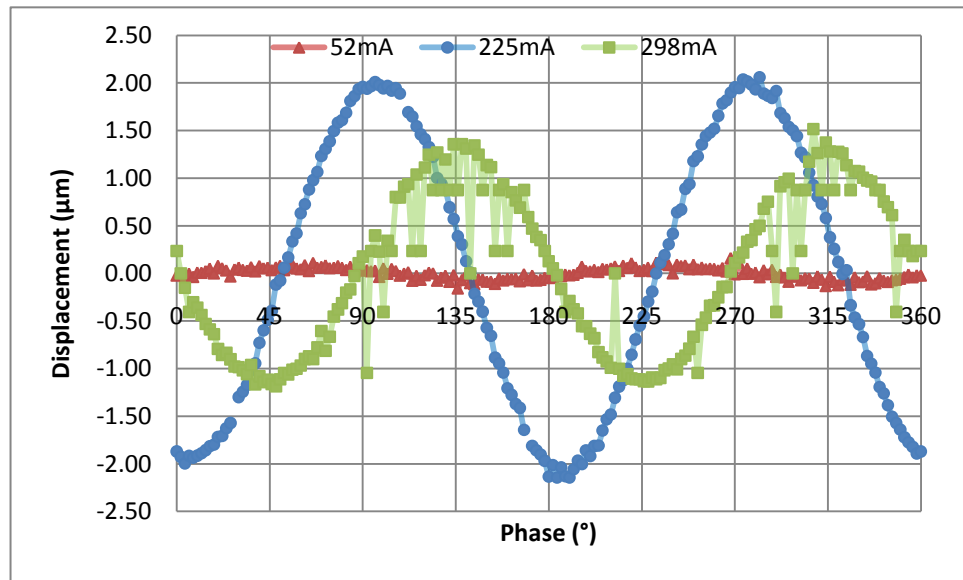
Figure 4-9 - Displacement of the thermal actuator at 3kHz excitation for different currents.

The 298mA signal is subject to more noise in comparison to the 225mA signal. This is caused by erroneous measurements made by the image processor when the thermal actuator moves out-of-plane and away from the focal point of the microscope, which can be observed visually as well. The 298mA signal is also offset by a displacement 0.25µm, which would be caused by a temperature offset due to insufficient cooling. The out-of-plane motions are undesirable due to changes in the apparent area of the capacitive fingers in the sensing circuit. The out-of-plane

displacement currents would not be selected regardless of these detrimental effects because the displacement for the 225mA signal dominates the greater current levels.

4.1.5 Thermally-Actuated Gyroscope Planar Sensing Mode Resonant Frequency Characterization

The sensing mode resonant frequency was identified with the PMA. The electrostatic parallel plate sensors were used as comb-drive actuators to excite the proof mass in the sensing direction. This was done by applying a 40V AC potential to the sensing fingers and gyroscope frame. To find the resonant frequency a 2kHz to 8kHz frequency sweep range was initially used. A finer sweep was used once the natural frequency was identified to define the resonant peak. A graph of the results can be found figure 4-11 below.
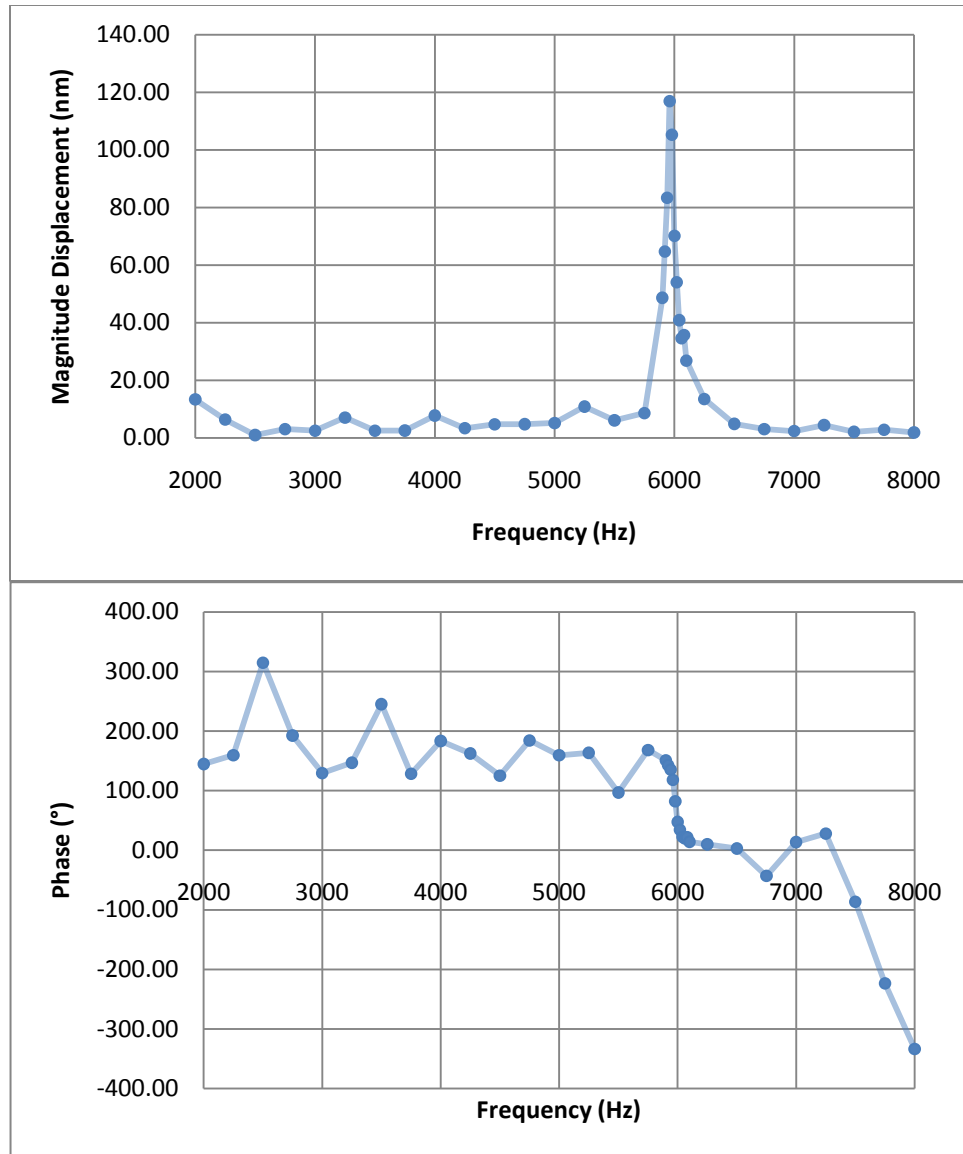
Figure 4-10 – Frequency response of the thermal gyroscope proof mass in the sensing direction.

The resonant frequency occurs at 5.98kHz for the in-plane sensing mode direction. At this frequency the amplitude of the displacement is 0.12μm using a 40V AC signal.

The relative proximity of the driving and sensing natural frequencies is beneficial to the output signal quality of the device; however, it may be detrimental to the device's accuracy due to susceptibility to temperature or pressure changes in the environment. These temperature and

pressure changes could shift the resonant frequencies of the modes, which would alter the force response due to the Coriolis acceleration acting on the sensing mass.

4.1.6 Thermally-Actuated Gyroscope Out-of-Plane Characterization

The out-of-plane response of the proof mass was found using the laser vibrometer. A 0.7V AC signal was applied to the chevron actuator to induce small vibrations in the structure. The system response was then recorded as an FFT to experimentally determine the eigenfrequencies. Figure 4-12 contains the FFT of the out-of-plane velocities caused by small vibrations.
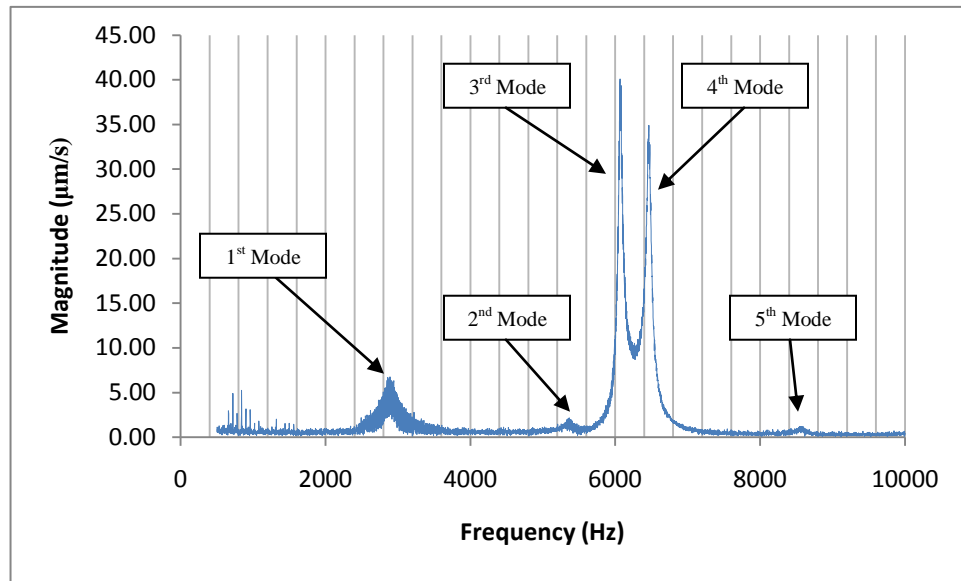
Figure 4-11 - Experimental out-of-plane FFT of the thermally-actuated gyroscope.

The FFT shown is the average spectrum of a matrix of points selected on the proof mass. The displacement vector of each point can be derived from the measurements and plotted such that the mode shapes can be reconstructed in a 2D plane. Images of the mode shapes can be seen in figure 4-13.
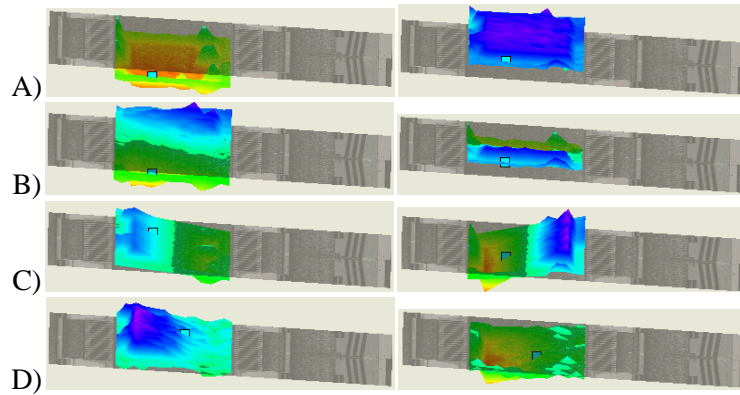
Figure 4-12 - Experimentally determined mode shapes for a thermally-actuated gyroscope at A) 1st observed mode at 2.9kHz, B) 2nd observed mode at 5.4kHz, C) 3rd and 4th observed mode at 6.1kHz and 6.5kHz, D) 5th observed mode at 8.6kHz

The first mode shape that occurs at 2.9kHz is a straight up-and-down mode. The second mode, at 5.4kHz, rotates about the driving axis and slightly wobbles about the sensing axis. The third and fourth peaks, which occur at 6.1kHz and 6.5kHz and have the largest amplitude, both have the same mode shape that rotates about the sensing axis. The final observed mode shape also rotates about the sensing direction; instead the actuation side of the proof mass is the nodal point.

4.2 Electrostatically-Actuated Gyroscopes Experimental Testing

4.2.1 Electrostatically-Actuated Gyroscopes Testing Methodology

Testing for the electrostatically-actuated MetalMUMPS gyroscope was performed similarly to the thermally actuated gyroscope testing as outlined in section 4.1.1; however voltage amplification was required in place of current amplification.
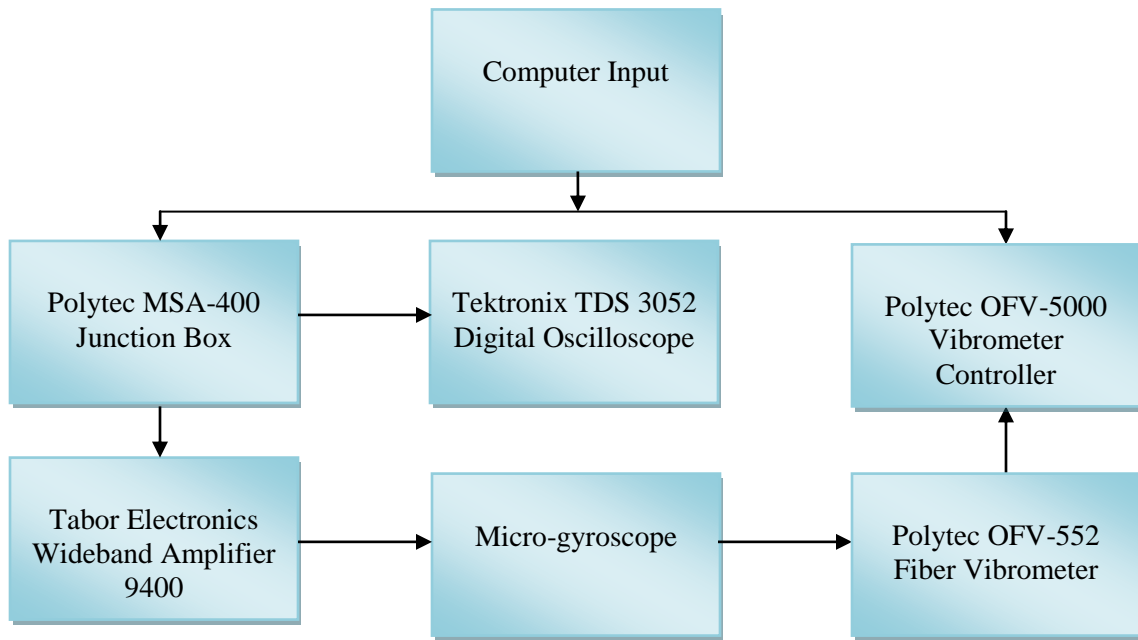
Figure 4-13 - Diagram of the electrical relationships between testing equipment apparatuses used for the electrostatically-actuated MetalMUMPS gyroscope.

The Tabor Electronics Voltage Amplifier had a gain of 50 for the operational frequency range it was used at.

4.2.2 Electrostatically-Actuated MetalMUMPS Micro-gyroscope Prototype

The electrostatically driven micro-gyroscope was fabricated using the MetalMUMPS process, which is outlined in section 2.2.1. Figure 4-15 below shows an SEM image of the gyroscope with the significant features identified.
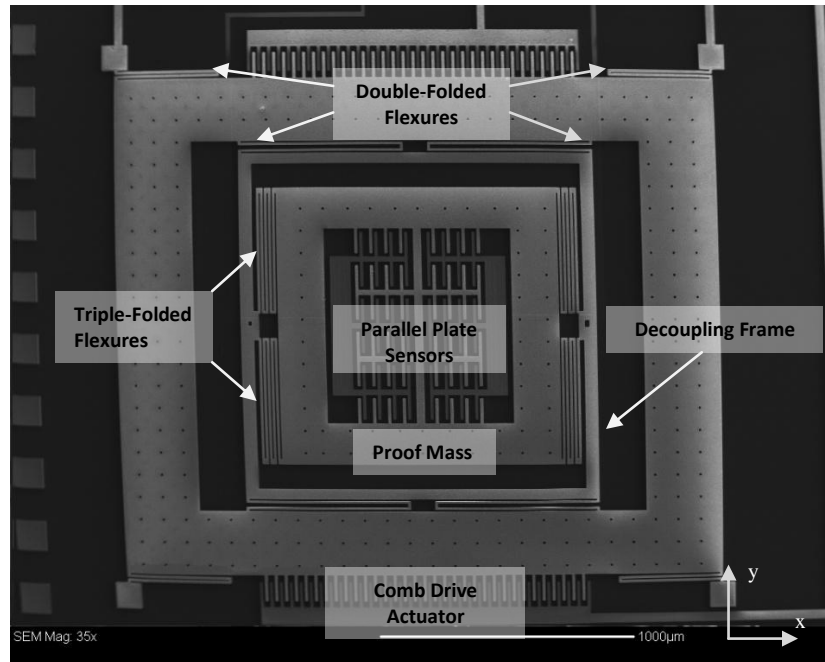
Figure 4-14 – SEM image of an electrostatically-actuated MetalMUMPS gyroscope prototype.

The device itself is approximately the same size as the thermally-actuated gyroscope with a footprint of 6mm^2 and a thickness of 20μm. The gyroscope is driven by comb drive actuators in the y-direction that are located at both ends of the device. The decoupling frame isolates the Coriolis induced force acting on the proof mass in the x-direction, also defined as the sensing direction in this case. The symmetrically placed parallel plate capacitive sensors detect movement in the sensing direction.

4.2.3 Electrostatically-Actuated MetalMUMPS Gyroscope Planar Driving Mode Resonant Frequency Characterization

The in-plane response of the MetalMUMPS electrostatically-actuated gyroscope was determined using the PMA. A 25V$_{AC}$ with 25V$_{DC}$ offset signal was applied to the comb drive actuator to excite the proof mass. A frequency sweep from 1kHz to 8kHz was used to identify the location of the resonant frequencies and a second finer sweep was performed to characterize the frequency

response curve of both the driving and sensing frequency; both frequency response curves are shown in Figure 4-16 and 4-17.
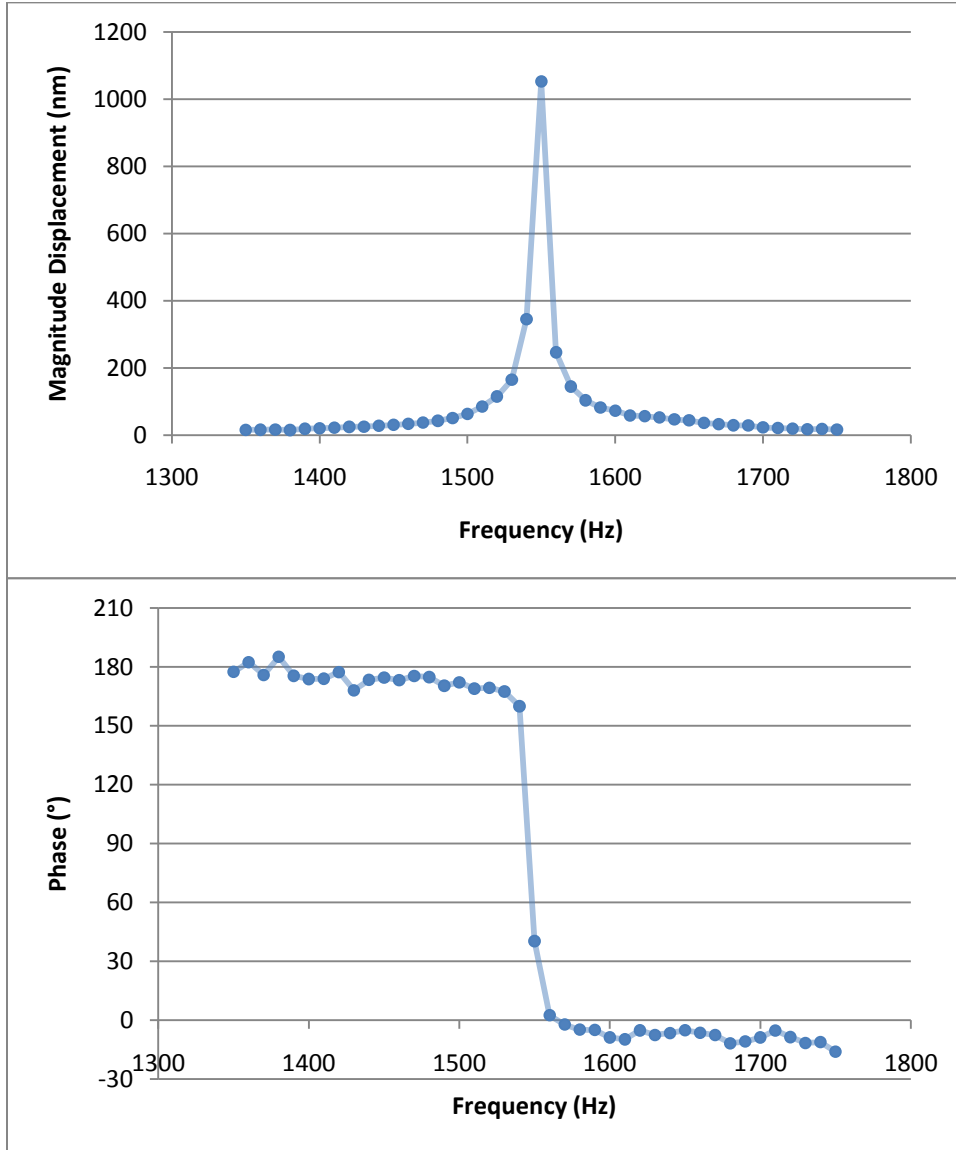
Figure 4-15 - Frequency response of the electrostatic gyroscope proof mass in the driving direction.
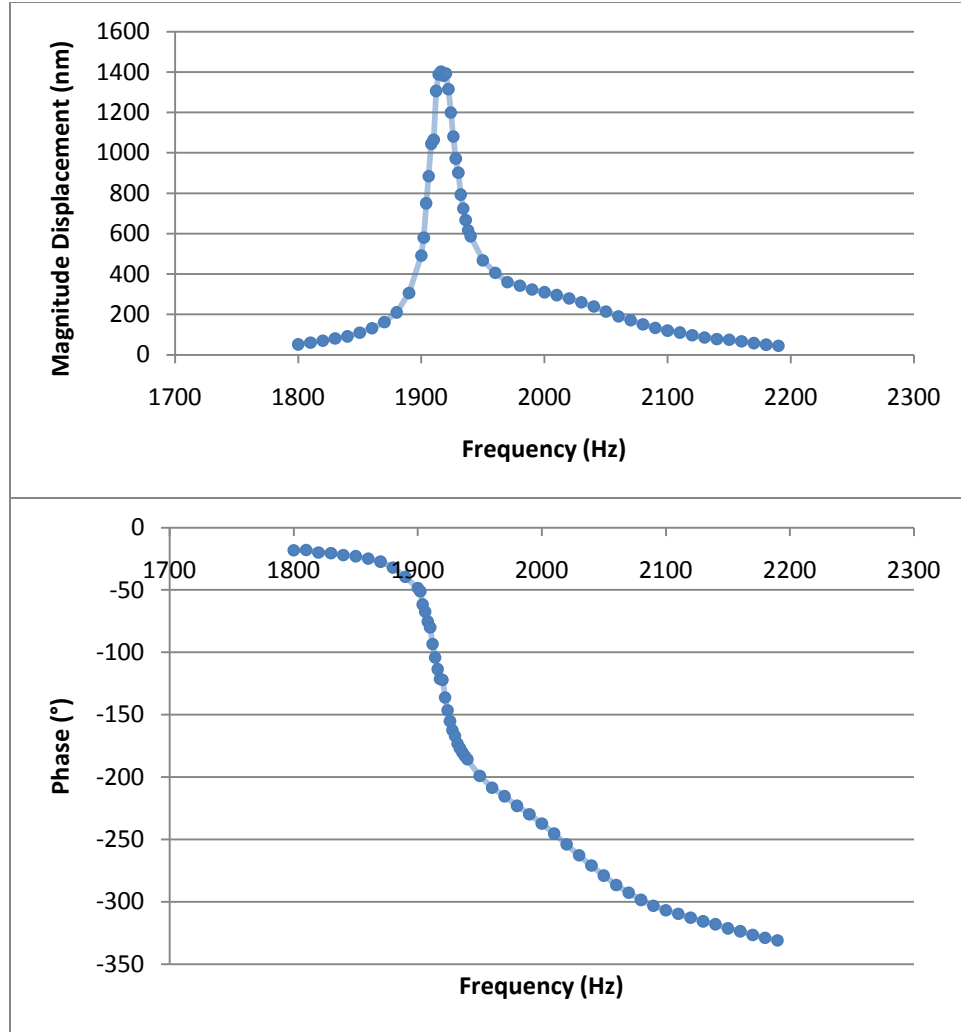
Figure 4-16 - Frequency response of the electrostatic gyroscope proof mass in the sensing direction.

The driving and sensing mode resonant frequencies were determined to be 1.56kHz and 1.91kHz respectively from the experimental data shown above.

A third in-plane mode was identified by the simulated results, labelled as the fourth mode in section 3.3, and was detected during the initial frequency sweep as well. However, the out-of-phase response of the driving frame and the proof mass made it difficult to identify the location of the resonant frequency due to interference of the two mass's vibration. The identification of the

resonant frequency of the fourth mode is not necessary to determine the ideal operational frequency of the device and can be ignored.

4.2.4 Electrostatically-Actuated MetalMUMPS Gyroscope Out-of-Plane Characterization

The gyroscope was driven using a $30V_{AC}$ 1kHz - 40kHz burst chirp excitation signal with $30V_{DC}$ offset. The out-of-plane mechanical response of the system was measured using the PSV system to determine the experimental eigenfrequencies. The resultant FFT is shown in figure 4-18.
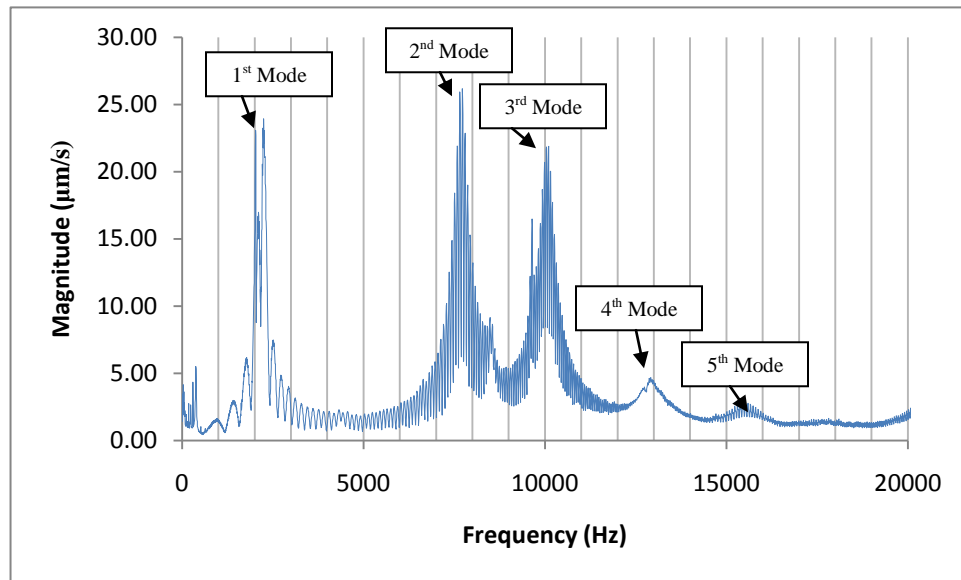
Figure 4-17 - Experimental out-of-plane FFT of the electrostatically-actuated gyroscope.

The entire non-fixed gyroscope structure was scanned to identify all the significant mode shapes on all three frames. Between 0kHz and 20kHz there are five significant peaks that were identified. The experimentally derived mode shapes can be seen in figure 4-19.
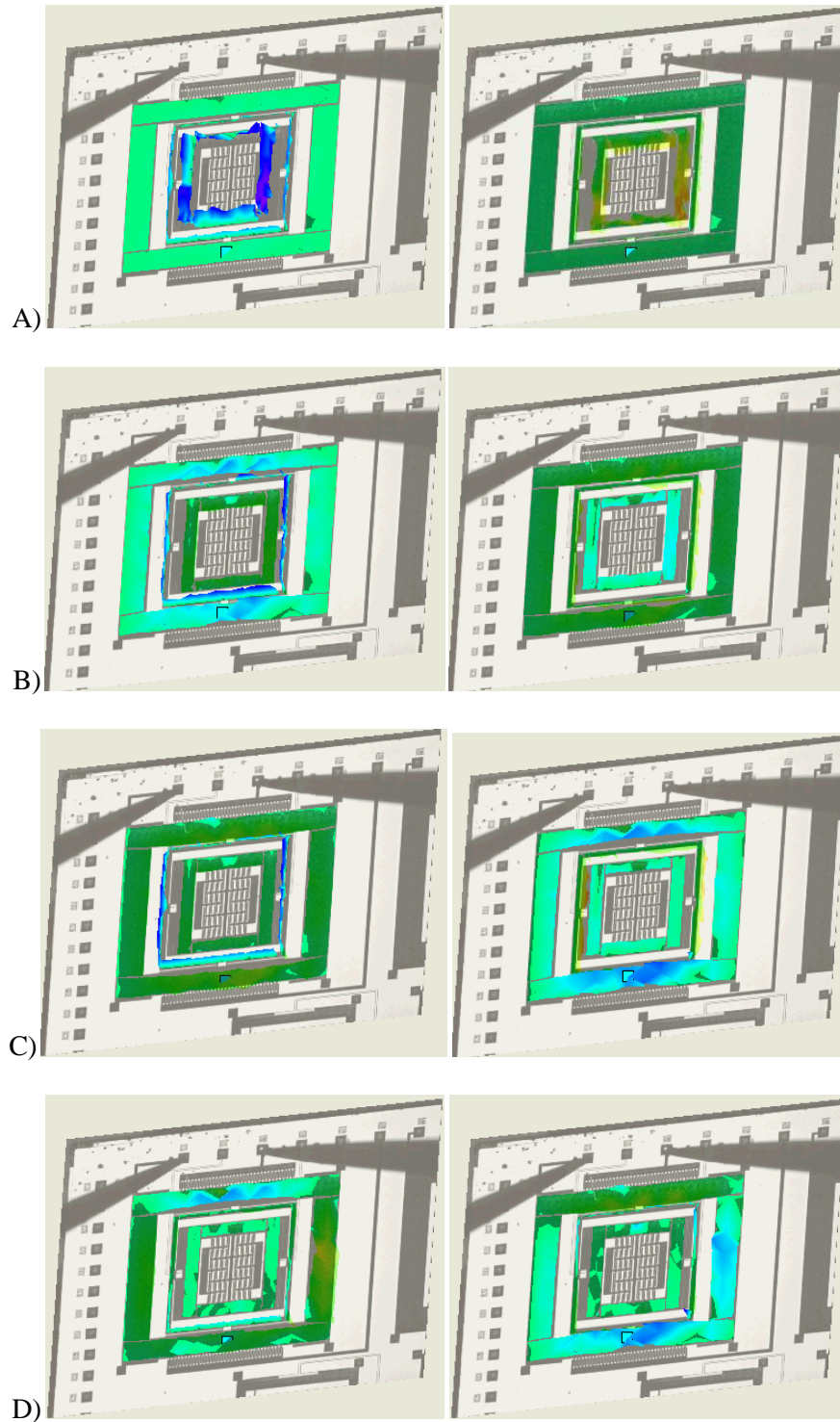
Figure 4-18 - Experimentally determined mode shapes for a thermally-actuated gyroscope at A) 3rd mode at 2.3kHz, B) 7th mode at 7.7kHz, C) 11th mode at 10.1kHz and D) an out-of-plane mode at 12.9kHz

The first mode shape, which occurs at 2.3kHz, is a straight up-and-down mode that acts on the proof mass and decoupling frame. The second mode shape is similar except that the proof mass vibrates 180° out-of-phase with the decoupling and outside frame at 7.7kHz. The peak that occurs at 10.1kHz is also an up-and-down mode shape, however the proof mass and outside frame are 180° out-of-phase with the decoupling frame. The mode shape that occurs at 12.9kHz is a wobbling vibration that only acts on the outer frame. The images of the peak that occurs at 15.5kHz are not shown due to noise interfering with the interpretation of the mode shape.

4.3 Electrostically-Actuated SOI Gyroscope Prototype

The electrostatically driven micro-gyroscope was fabricated using the SOI process, which is outlined in section 2.2.2. The figure below shows an SEM image of the SOI design made with the MetalMUMPS process. The in-plane dimensions of the SOI and MetalMUMPS devices are comparable; however the SCSi layer of the SOI device does not show up clearly in SEM imaging. The device has an approximate thickness of 10µm.
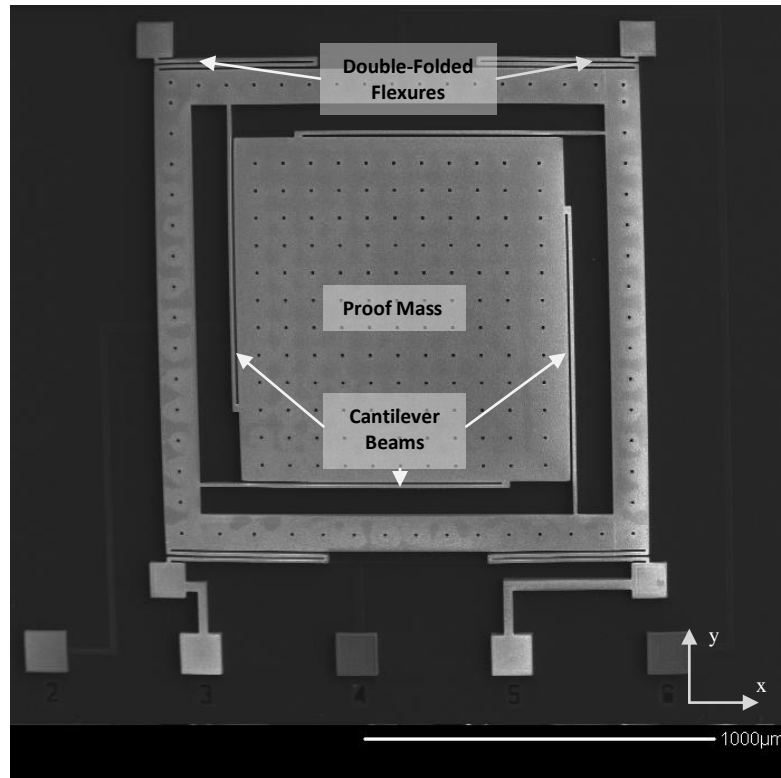
Figure 4-19 – SEM image of an electrostatically-actuated MetalMUMPS gyroscope prototype: SOI design

The operational principles of the out-of-plane device are different compared to the other two designs. The proof mass is actuated out-of-plane in the z-direction by a capacitive plate concealed underneath the mass. A rotation about the x-axis will induce an acceleration in the y-direction when the proof mass is actuated. Capacitive plate sensors underneath the outside frame detect the displacement in the y-direction. The 1μm thin cantilever beams ideally isolate the out-of-plane motion from the surrounding frame.

Testing was not possible due to the lack of functioning prototypes. The thin cantilever beams were broken, which was likely due to fabrication complications or the structure may have been too weak to survive transport.

Chapter 5

Simulated and Experimental Results Analysis

This section explores the significance of the results reported in chapters 3 and 4.

5.1 Detrimental Mode Shapes

The only two desirable mode shapes are the driving and sensing modes for each gyroscope. Other mode shapes can potentially interfere with the sensing performance of the gyroscopes, which is why each gyroscope uses symmetrical capacitive sensors to reduce error from sub-optimal mode shape displacements. The out-of-plane data for the thermally-driven gyroscope in section 4.6 shows several modes that are detrimental to the sensing performance of the device. The proof mass vibrates out-of-plane causing error due to the reduction in the apparent area of the parallel sensing plates from any displacement in the z-direction.

The same problem affects the electrostatically-actuated MetalMUMPS gyroscope; however the fourth simulated mode, found in figure 3-10 in section 3.3, interferes in-plane. The driving frame and decoupling frame resonate out-of-phase with each other, which reduces the driving velocity on the sensing frame that will decrease the strength of the output signal.

One method that can be used to mitigate the error associated with detrimental mode shapes. The detrimental mode shapes can be predicted using simulated modal analysis and experimental evaluation. Once identified, the amplitudes of the mode shapes can be reduced by avoiding the resonant frequencies of the detrimental modes when exciting the device. However this must be accounted for in the original design by separating the sensing mode resonant frequency from any unfavourable mode shape resonant frequencies.

The error associated with out-of-plane mode shapes can be determined while driving the gyroscope at its operational frequency. The PSV would then be used to produce an FFT of the proof mass and the magnitude of the displacement would be determined. Ideally, an angular velocity would be applied as well, but this would be impossible with the current testing setup.
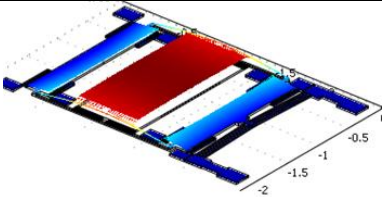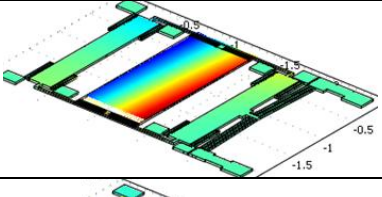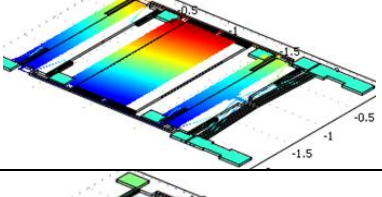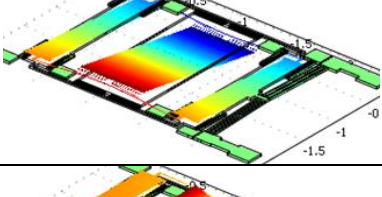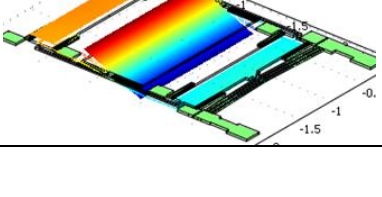
5.2 Comparison of Simulated and Experimental Results

The results from the simulations and experimental tests are compared to determine the accuracy of the simulated models and to give additional insight to the interpretation of the experimental data.

5.2.1 Thermally-Actuated Micro-gyroscope

The experimental data matched the order of the simulated modes but there is a large discrepancy in the resonant frequencies where they occur. This information is summarized in the table below.

Table 5-1 - Thermally-actuated gyroscope mode shape comparison.
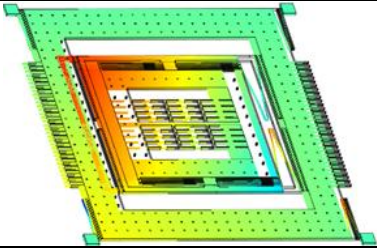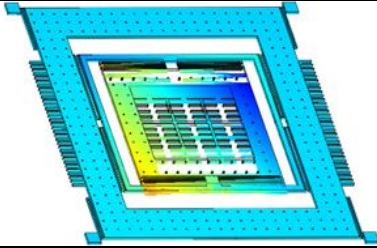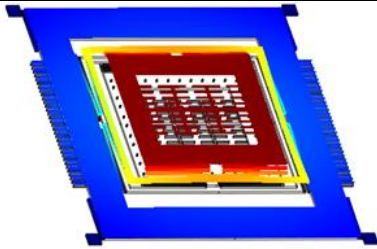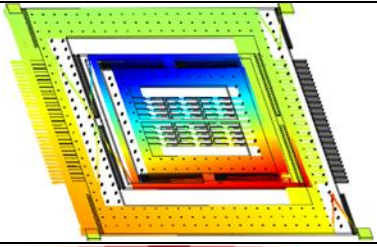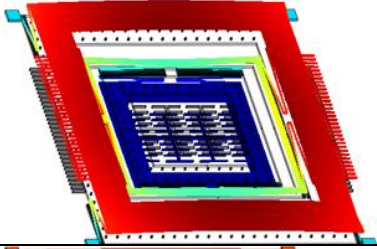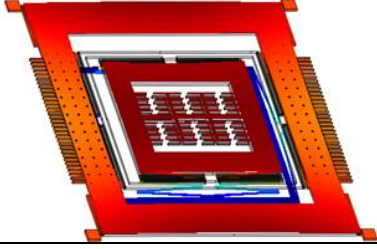
Mode Shape	Simulated (kHz)	Experimental (kHz)	Error (%)
	3.669	2.9	26.5%
	4.948	5.4	-8.4%
	5.459	6.0	-9.0%
	6.293	6.0	4.9%
	8.500	6.1, 6.5	39.3%, 30.8%

The experimental double-peak at 6.1kHz and 6.5kHz can be explained by the in-plane driving mode exciting the out-of-plane mode such that there are two observable peaks with the same mode shape.

5.2.2 Electrostatically-Actuated MetalMUMPS Micro-gyroscope

The out-of-plane mode shapes for the electrostatically-driven MetalMUMPS gyroscope also occur in order according to the simulated model. The data for the out-of-plane modes for both the simulated and experimental data and the in-plane modes for the simulated data are shown below.

Table 5-2 - Electrostatically-actuated MetalMUMPS gyroscope mode shape comparison.

Mode Shape	Simulated (kHz)	Experimental (kHz)	Error (%)
	1.170	1.6	-26.9%
	1.644	1.9	-13.5%
	1.941	2.3	-15.6%
	2.316	Not Available	Not Available
	4.246	7.7	-44.9%
	8.510	10.1	-15.7%

Due to the increased relative complexity of the electrostatically-actuated MetalMUMPS gyroscope, it has a high mode shape density making it difficult to differentiate between modes. Higher-energy modes typically overwhelm those with smaller amplitudes as well, which makes them difficult to identify.

5.2.3 Error Explanation

There are several factors that can explain the discrepancies found between the simulated and experimental results. One source of error is the exclusion of damping from the simulated model. This is expected to reduce the resonant frequencies in each mode compared to the simulated eigenfrequencies. The damping factor is also expected to vary with each mode shape depending on the contribution of viscous shearing forces and pressure differentials across the vibrating element. An in-plane mode will be less damped compared to an out-of-plane mode because there will be a greater shear force and a smaller pressure differential due to the surface area in each plane. It is expected that the experimental in-plane resonant frequencies will be closer to the simulated values for this reason. The information contained in table 5-1 is agreeable with this theory. However, upon calculating the quality factors from the experimental data using equation 1.8 and determining the damping coefficients using equation 1.7, the damping coefficient, ζ, for each mode shape was determined to be much less than 0.1; therefore damping can be accurately neglected from the simulated model. The quality factors and damping coefficients for each experimentally determined resonant peak are shown in figures 1 and 2 in the appendix.

The material properties from the COMSOL library and those of the gyroscopes can vary and cause a disparity between the simulated and experimental data. The material properties are also expected to be inconsistent within the gyroscope structure depending on imperfections and the size of the grain boundaries. The two significant properties that would affect the difference between the experimental and simulated models are density and Young's modulus. The values of

the properties are dependent on the type of fabrication method used and the thickness of the thin film. The range of values for the Young's modulus of nickel has been reported by various sources to be anywhere between 150GPa and 245GPa[21]. Any deviation of the actual material properties from the default COMSOL properties is expected to shift the resonant frequencies that the mode shapes occur at. The values that were used in the simulations are contained in table 1 in the appendix, which were taken directly from the COMSOL material library. According to the analytical model, a Young's modulus of 245GPa, a difference of 12% between the simulated and experimental value, would result in a discrepancy of 5.8%. Therefore any difference in the actual value of the Young's modulus would not account for all the error reported in tables 5-1 and 5-2.

The dimensions of the gyroscopes are also expected to vary between the simulated models and the prototypes. The CAD models, which were used for fabrication, were imported directly into COMSOL; the simulated and prototype dimensions are identical except for alterations made to the thermal gyroscope to simplify the structure and dimension variation due to fabrication tolerances. These variations are expected to change the spring and mass values for each element within the gyroscope's structure. The spring values are more susceptible to changes in the dimensions because of the relative thinness of the flexures. The thickness of MetalMUMPS structures can vary up to 20±10μm, which can result in large discrepancies between the actual device and the theoretical mass and spring matrices.[11] A thickness of 30μm would result in a discrepancy between the simulated and experimental results up to 50% according to the analytical model, which would account for all the error in the out-of-plane results. Two other common causes of dimensional error include slanted side-walls, an inherent limitation of the MetalMUMPS process, and mushrooming of the electroplated nickel.

Residual stresses may also be present within the structure after fabrication. They are not particularly significant in bottom-up fabrication processes such as electroplating but can still affect the resonant frequencies of a mechanical system.

5.3 Performance Analysis

5.3.1 Thermally-Actuated MetalMUMPS Gyroscope Mode Matching

The in-plane analysis in chapter 4 for the thermally-actuated gyroscope indicates that the driving and sensing modes are closely matched. The driving mode occurred at 6.0kHz and the sensing mode occurred at 5.98kHz. Having both modes directly coincide is ideal if the objective is to elicit the greatest response using the least amount of energy; however the system's performance is relatively unstable in this case. Fluctuations in temperature and pressure can affect the sensing mode's resonant frequency and change the magnitude of the response that will ultimately affect the output. It is expected that the thermally-actuated gyroscope will be highly dependent on environmental temperatures and pressures during operation, which will need to be compensated by additional circuitry. The sensitivity of environmental conditions can be tested by applying an angular velocity and changing the temperature and pressure then measuring the output. Sensitivity is one of the performance indicators of gyroscopic sensors.

5.3.2 Electrostatically-Actuated MetalMUMPS Gyroscope Predicted Mode Matching

Experimental in-plane mode testing has not been performed; consequently the simulated data is used to predict the modal response of the electrostatically-actuated gyroscopes. Three in-plane modes were identified in the simulated model. At 1.6kHz the proof mass and decoupling frame vibrate in the driving direction, and at 1.9kHz the proof mass resonates in the sensing direction. The gyroscope is expected to have poor temperature and pressure sensitivity because of the high quality factor of the sensing and driving mode frequency response curves. The gyroscope also will not take advantage of mode coupling because of the relatively large difference in proximity between the driving and sensing modes. Also, the out-of-phase driving mode, estimated to occur at 2.316kHz, will negatively affect the performance. The velocity of the proof mass is reduced by

the out-of-phase motion, which will affect the response in the sensing direction; therefore excitation signals close to this frequency should be avoided during operation.

5.3.3 Electrostatically-Actuated SOI Gyroscope Predicted Mode Matching

The simulated driving and sensing mode resonant frequencies was determined to be 2.159kHz and 3.298kHz respectively. The frequency span between both modes may be too great for the gyroscope to take advantage of mode matching; however it is difficult to speculate without knowing the quality factor of each peak. The driving response of the gyroscope will also be relatively small because of the large disparity between the driving and sensing modes.

5.3.4 Thermally-Actuated Gyroscope Power and Efficiency

Electrical power tests and the amplitude response from the gyroscope, summarized in figure 4-8, are important to the viability of thermally-actuated gyroscope designs. A significant disadvantage of electrostatically-actuated designs is the high voltage requirement, which requires on-chip circuitry and can sometimes restrict design possibilities. Thermal actuators require much lower voltages that make them easily implemented with digital CMOS circuitry. The disadvantage of thermal actuators is their large power requirements compared to electrostatic actuators, which is evident in the power tests that were performed. The largest amplitude observed was 4.2μm, which required 363.39mW to achieve. Increasing the power only induced out-of-plane responses. Microprocessors cannot output this much current; however several adjustments can be made to drive the gyroscope with a microprocessor.

Microprocessors are only capable of outputting square wave signals as opposed to the sinusoidal actuation signals were used during testing to drive the gyroscope. It was not possible to perform tests using a square wave actuation signal due to limitations of the testing equipment; however a square wave driving signal would be a better waveform to use because of its greater power

density, which would also elicit a faster response. Adjusting the voltage drop across the thermal actuator is one prerequisite for testing using a microprocessor. Currently, a $1.5V_{RMS}$ drop is observed; most microprocessors output 5V. It would be more efficient if a 5V drop was observed; however the gyroscope would have to be designed and fabricated around these specifications. Future thermally-actuated gyroscopes could incorporate this in their design specifications to optimize the efficiency.

The power requirements of the gyroscope would be further reduced by using on-chip circuitry. There is energy loss in the wires with the current testing setup that would be reduced if shorter interconnects were used. Also, the power used to elicit a peak-to-peak displacement of 4.2μm is not necessary. A smaller electrical current will also excite the proof mass in the sensing direction as well, albeit at a reduced response due to the decrease in driving velocity. Further testing is required to determine how low the driving current can be while still maintaining an acceptable output signal.

Chapter 6

Conclusion

The objective was to determine and characterize the modal behaviour of three MEMS gyroscopic sensors using simulated models in COMSOL and through experimental methods. Each gyroscope had its own distinguishing features; one was a novel thermally-actuated design, another used an electrostatic actuation method, which was manufactured using the MetalMUMPS fabrication process and another was an out-of-plane SOI design.

Simulated models were created for all three gyroscopes from CAD files to reduce the potential for dimensional error. Several mode shape resonant frequencies were solved for in each model, which were then used as predictions for the experimental PSV and PMA testing to help interpret the results.

Experimental testing was then performed for the thermally-actuated gyroscope and electrostatic MetalMUMPS gyroscope. Static testing was performed first to identify the driving signal power requirements. The thermal actuator required a driving current of at least 150mA to elicit a significant response. Similarly, the electrostatic actuator required a $25V_{AC}$ with $25V_{DC}$ offset to actuate. Seventeen dynamic tests were performed to characterize the response of the thermal gyroscope at different driving currents. The maximum peak-to-peak displacement observed was 4.2μm at $225.4mA_{RMS}$ current. Increasing the current provoked out-of-plane responses and reduced the in-plane displacement. The frequency response of the thermal actuator was determined similarly by measuring the amplitude of the displacement and varying the frequency. The frequency response of the in-plane sensing mode was also measured by using the parallel plate sensing fingers as actuators by applying a 40V AC driving signal. The natural frequency of the driving and sensing modes of the thermally-actuated gyroscope was experimentally

97

determined to be 6.0kHz and 5.98kHz respectively. Similarly, the driving and sensing mode resonant frequencies for the MetalMUMPS electrostatically-actuated gyroscope are 1.6kHz and 1.9kHz respectively.

The out-of-plane mode shape resonant frequencies were found using an FFT. The results were compared to the eigenfrequencies found in the simulated solutions and the discrepancies were attributed to fabrication and material tolerances, residual stresses and the exclusion of damping from the simulated model. An analytical model as well as quality factors derived from the experimental results was used to determine the most significant contributor to the error that was observed. The fabrication and material tolerances were determined to be the most significant contributors to the error between the experimental and theoretical results. An analysis on each significant mode shape helped identify modes that may interfere with the sensing performance of the gyroscopes. Similarly, the locations of the natural frequencies of the driving and sensing modes were used to predict the response of the gyroscope from mode matching.

6.1 Future Work Recommendations

The simulated models need additional work if they are to be useful for the fabrication of future gyroscope models. The inclusion of damping in a frequency response simulation would be useful for predicting the modal behaviour of the gyroscopes; however it will be difficult to derive an accurate viscous damping model that accounts for the variability in damping coefficients for each mode shape. Tweaking the material property settings, model dimensions and residual stresses in the current COMSOL models such that they closely match the experimental data will help with future simulations for other gyroscopes as well if the same settings are used. Completion of testing on the SOI electrostatically-actuated gyroscope would be useful for revising the simulations.

Circuitry for the capacitive sensing plates must be designed and connected as well in order to convert the capacitance to an output voltage for all gyroscopes. The significance of the modal behaviour of each gyroscope will be made explicit by measuring the performance indicators using rate table testing. Insight gained from these tests will be useful in designing future gyroscope devices. It is recommended that a new thermal-actuated gyroscope should be designed and fabricated to take advantage of the increased efficiency and ease-of-integration benefits of a thermal actuator that is intended to accept a 5V square wave driving signal.

6.2 Thesis Contribution

All the simulated and experimental results were original work performed by the author. The gyroscopic sensors were designed by Rana Iqtidar Shakoor, a previous graduate student at Queen's University.

References

[1] R. Feynman, "There's Plenty of Room at the Bottom", Journal of Micromechanical Systems Vol. 1, No. 1, March 1992, pp.60-66.

[2] M. Dahleh and W. Thomson, "Theory of Vibration with Applications", 5th Edition, Prentice-Hall Inc, 1998, ISBN 0-13-651068-X.

[3] B. Zhang and D. Fang, "Modeling and modification of the parallel plate variable MEMS capacitors considering deformation issue", Mechanism and Machine Theory, 44(4), 2009, pp. 647-655.

[4] R. Johnson, "MEMS finds niche in space exploration", EE Times, 2007

http://www.eetasia.com/ART_8800479803_480500_NT_ca7d6a67.HTM.

[5] W. Huang and G. Lu, "Analysis of lateral instability of in-plane comb drive MEMS actuators based on a two-dimensional model", Sensors and Actuators A: Physical 113(1), 2004, pp. 78-85.

[6] J.-C. Chiou, Y.-J. Lin and C.-F. Kuo, "Extending the traveling range with acascade electrostatic comb-drive actuator", J. Micromech. Microeng. 18 (2008) 015018 (7pp).

[7] "Lithography", http://www.memsnet.org/mems/processes/lithography.html.

[8] J. Ravnkilde, A. Yalcinkaya, L. Johansen and O. Hansen, "Fabrication of electroplated nickel micromechanical comb resonators", Technical University of Denmark DTU, Electrochemical Society Proceedings Vol. 99-34, pp. 197-202.

[9] J. Jahns and K. Brenner, "Microoptics: From technology to applications", New York : Springer, 2004.

[10] O. Geschke, H. Klank, P. Telleman, "Microsystem Engineering of Lab-on-a-Chip Devices", Ch. 6, Silicon and Cleanroom Processing (Lecture 2), Wiley-VCH, 2004.

[11] "MetalMUMPs Design Handbook", Revision 2.0, MEMSCAP Inc.

[12] "Micragem Data Sheet", Micralyne Inc.

[13] B. Bokenhorn and P. Greiff, "A vibratory micromechanical gyroscope", Navigation and Control Conference, Minneapolis, MN, Aug. 15-17, 1988, Technical Papers. Part 2 (A88-50160 21-08). Washington, DC, American Institute of Aeronautics and Astronautics, 1988, p. 1033-1040.

[14] Roylance, L. M., and J. B. Angell, "A Batch-Fabricated Silicon Accelerometer," IEEE Trans. Electron Devices, ED-26, 1979, pp. 1911–1917.

[15] K. Tanaka, Y. Mochida, S. Sugimoto, K. Moriya, T. Hasegawa, K. Atsuchi, and K. Ohwada, "A micromachined vibrating gyroscope". Proc., Eighth IEEE Int. Conf. on Micro Electro Mechanical Systems (MEMS '95), Amsterdam, Netherlands, Jan. 1995, pp. 278-281.

[16] T. Juneau, A. P. Pisano, and J. H. Smith, "Dual axis operation of a micromachined rate gyroscope" Proc., IEEE 1997 Int. Conf. on Solid State Sensors and Actuators (Tranducers '97), Chicago, June 1997, pp. 883-886.

[17] Y. Mochida, M. Tamura, and K. Ohwada, "A micromachined vibrating rate gyroscope with independent beams for the drive and detection modes." Proc. Twelfth IEEE Int. Conf. on Micro Electro Mechanical Systems (MEMS '99), Orlando, FL, Jan. 1999, pp. 618-623.

[18] C. Acar, A. M. Shkel "Inherently Robust Micromachined Gyroscopes with 2-DoF Sense Mode Oscillator" Journal of Microelectromechanical System, Vol 15, No.2, April 2006, pp 380-387.

[19] S. Bazaz, M. Burnie, M. Hasan, Y. Lai and R. Shakoor, "Electrothermally Actuated Resonant Rate Gyroscope Fabricated using the MetalMUMPs", unpublished.

[20] "Polytec Scanning Vibrometer: Theory Manual", Revision 8.4, Polytec Inc.

[21] D.-C. Baek, T.-S. Park and S.-B. Lee, "Measurement of Mechanical Properties of Electroplated Nickel Thin Film", Key Engineering Materials Vols. 261-263, 2004, pp 417-422.

Appendix

Table Appendix-5-Error! Main Document Only. **- Values for material properties used for simulation models.**

Material	Young`s Modulus (GPa)	Density (kg/m^3)
Nickel	219	8900
Single-Crystal Silicon	200	2330

Table Appenix-5-Error! Main Document Only. **- Thermally-actuated gyroscope dynamic testing results.**

| SG P-P Volt. (V)	Gyro P-P Volt. (V)	Gyro RMS Volt. (V)	RMS Current (mA)	Gyro Power (mW)	DC Current (mA)	Peak-to-Peak (μm)
0.13	0.13	0.09	0.45	0.04	4	
0.32	0.28	0.20	16.68	3.30	11	
0.52	0.42	0.30	32.95	9.79	19	
0.71	0.57	0.40	48.9	19.71	27	0.17
0.93	0.74	0.52	65.4	34.22	35	0.26
1.13	0.9	0.64	82.1	52.25	43	0.32
1.3	1.08	0.76	98.9	75.53	52	0.38
1.51	1.25	0.88	116.5	102.97	60	0.44
1.72	1.44	1.02	129.4	131.76	67	0.57
1.9	1.65	1.17	138.1	161.12	71	0.63
2.1	1.83	1.29	160	207.04	80	1.00
2.3	1.97	1.39	175.5	244.47	92	1.45
2.51	2.22	1.57	201.6	316.47	104	2.34
2.7	2.28	1.61	225.4	363.39	117	4.20
2.9	2.5	1.77	243.8	430.98	124	4.10
3.1	2.6	1.84	278.3	511.65	138	3.47
3.29	2.74	1.94	297.6	576.59	151	2.70
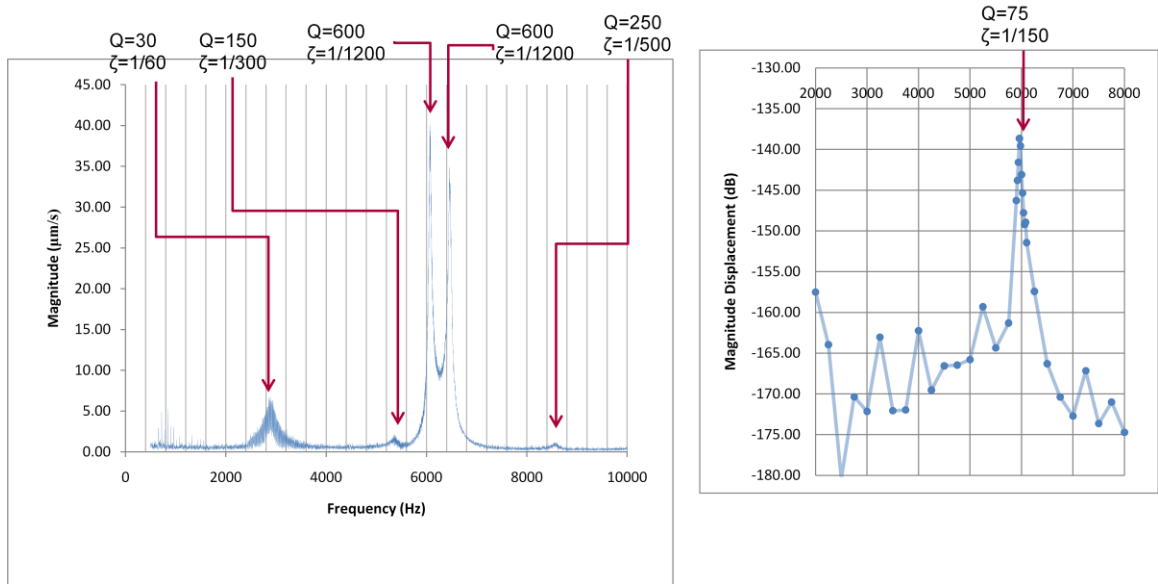
Figure Appendix- Error! Main Document Only. **– Experimentally calculated quality factors and damping coefficients of the thermally-actuated gyroscopic sensor.**
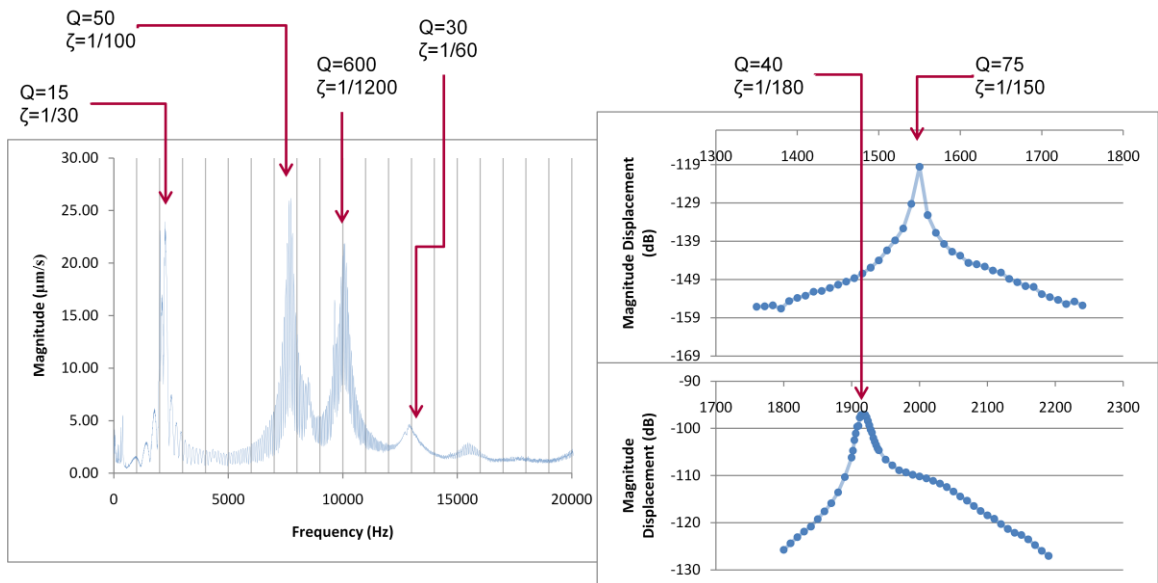

Figure Appendix- Error! Main Document Only. **- Experimentally calculated quality factors and damping coefficients of the electrostatically-actuated MetalMUMPS gyroscopic sensor.**